INTERPRETING SATELLITE REMOTE SENSING, AIRCRAFT AND GROUND-BASED OBSERVATIONS OF AEROSOL USING A CHEMICAL TRANSPORT MODEL

by

Jun-Wei Xu

Submitted in partial fulfilment of the requirements
for the degree of Doctor of Philosophy

at

Dalhousie University
Halifax, Nova Scotia
September 2018

Table of Contents

List of Tables

List of Figures

Abstract

Fine particulate matter ($PM_{2.5}$) is the leading environmental risk factor for the global burden of disease. Black carbon (BC) and metal components are primarily responsible for the adverse health effects associated with $PM_{2.5}$. $PM_{2.5}$ also has climate effects, especially BC that contributes significantly to Arctic warming. We interpret satellite, aircraft, and ground-based measurements using the GEOS-Chem global chemical transport model to better understand $PM_{2.5}$ and its chemical composition.

We determine and interpret $PM_{2.5}$ concentrations over eastern China for 2013 from aerosol optical depth (AOD) retrieved by the new Korean geostationary ocean color imager (GOCI) satellite instrument. Significant agreement is found between GOCI-derived $PM_{2.5}$ and ground-based measurements in both annual averages (R^2 =0.66, N = 494) and monthly averages (relative RMSE = 18.3 %). Secondary inorganics (SO_4^{2-}, NO_3^-, NH_4^+) and organic matter are the most important components of GOCI-derived $PM_{2.5}$. The population-weighted GOCI-derived $PM_{2.5}$ over eastern China for 2013 is 53.8 μg m^{-3}, with 400 million residents in regions that exceed the Interim Target-1 of the World Health Organization.

We interpret a series of recent airborne and ground-based measurements with the GEOS-Chem model and its adjoint to attribute the sources of Arctic BC. We find that anthropogenic emissions from eastern and southern Asia have the largest impact on the Arctic BC column burden (~37%) and that anthropogenic emissions from northern Asia are the primary source of the Arctic surface BC (~40%). Our adjoint simulations indicate noteworthy contributions from emissions in eastern China (15 %) and western Siberia (6.5 %) to the Arctic BC column concentrations. Gas flaring emissions from oilfields in western Siberia could have a striking impact (13 %) on Arctic BC loadings in January.

We present an initial simulation of 12 trace metals: Si, Ca, Al, Fe, Ti, Mn, K, Mg, As, Cd, Ni and Pb over continental North America for 2013 at a fine resolution of 0.25 ° x 0.3125 ° by using the GEOS-Chem transport model. The evaluation of modeled trace metal concentrations with observations from more than 200 monitors across North America indicates a promising spatial consistency.

List of Abbreviations and Symbols Used

Symbol	Units	Description
ACENET		Atlantic Computational Excellence Network
AE		Aethalometer
AERONET		Aerosol Robotic Network
AFD		Anthropogenic Fugitive Dust
AMS		Aerosol Mass Spectrometer
AOD		Aerosol Optical Depth
ARCPAC		Aerosol, Radiation, and Cloud Processes affecting Arctic Climate
ARCTAS		Arctic Research of the Composition of the Troposphere from Aircraft and Satellites
AWI		Alfred Wegener Institute
BAM		Beta Attenuation Monitor
BC		Black Carbon
BRAVO		Big Bend Regional Aerosol and Visibility Observational Inventory
CALIOP		Cloud-Aerosol Lidar with Orthogonal Polarization
CALIPSO		Cloud-Aerosol Lidar and Infrared Pathfinder Satellite Observations
CAPMON		Canadian Air and Precipitation Monitoring Network
CASTNET		Clean Air Status and Trends Network
CEMC		China Environmental Monitoring Center
CESM-CAM		The Community Earth System Model - Community Atmosphere Model
CNAAQS		Chinese National Ambient Air Quality Standard
COMS		Communication, Ocean, and Meteorology Satellite
CSN		Chemical Speciation Network
CTM		Chemical Transport Model
CV		Coefficient of Variation
DEAD		Dust Entrainment and Deposition
DEHM		den Danske Eulerske Hemisfæriske Model
DJF		December-January-February
EBC		Equivalent Black Carbon
EC		Elemental Carbon
ECLIPSE		Evaluating the climate and Air Quality Impacts of short-Lived Pollutants
EDGAR		Emission Database for Global Atmospheric Research
EDXRF		Energy Dispersive X-Ray Fluorescence
EMEP		European Monitoring and Evaluation Programme
EPA		Environmental Protection Agency
EPA-AQS		U.S. Environmental Protection Agency Air Quality System
FLEXPART		FLEXible PARTicle dispersion model
GEOS		Goddard Earth Observing System
GFED		Global Fire Emissions Database
GMAO		Global Modeling Assimilation Office

GOCI		Geostationary Ocean Color Imager
GW		Gridded Population of the World
HTAP		Hemispheric Transport of Air Pollution
IMPROVE		Interagency Monitoring of Protected Visual Environments
IPCC		Intergovernmental Panel on Climate Change
ISORROPIA		
IT		Interim
JJA		June-July-August
MAC		Mass Absorption Coefficient
MAM		March-April-May
MEGAN		Model of Emissions of Gases and Aerosol from Nature
MEIC		Multi-resolution Emission Inventory for China
MERRA		Modern-Era Retrospective Analysis for Research and Applications
MFB	%	Mean Fractional Bias
MFE	%	Mean Fractional Error
MICS		Model Inter-Comparison Study
MISR		Multiangle Imaging Spectroradiometer
MODIS		Moderate Resolution Imaging Spectroradiometer
NADP		National Atmospheric Deposition Program
NAPS		National Air Pollution Surveillance Network
NASA		National Aeronautics and Space Administration
NASA		The National Aeronautics and Space Administration
NATA		National Air Toxics Assessment
NDPS		National Deposition
NEI		National Emission Inventory
NETCARE		Network on Climate and Aerosols: Addressing Key Uncertainties in Remote Canadian Environments
NMB	%	Normalized Mean Bias
NME	%	Normalized Mean Error
NOx		NO + NO2
NSERC		National Science and Engineering Research Council
OA		Organic Aerosol
OC		Organic Carbon
OM		Organic Mass (a synonym of Organic Aerosol)
OMI		Ozone Monitoring Instrument
PAMARCMiP		Polar Airborne Measurements and Arctic Regional Climate Model Simulation Project
PM_{10}	$\mu g\ m^{-3}$	Fine particulate matter with aerodynamic diameter less than 10 μm
$PM_{2.5}$	$\mu g\ m^{-3}$	Fine particulate matter with aerodynamic diameter less than 2.5 μm
POA		Primary Organic Aerosol
PSAP		particle soot absorption photometer

rBC		refractory Black Carbon
RMSE	$\mu g\ m^{-3}$	Root Mean Square Error
rRMSE	%	relative Root Mean Square Error
SIA		Secondary Inorganic Aerosol
SOA		Secondary Organic Aerosol
SON		September-October-November
SP2		single particle soot photometer
SPARTAN		Surface PARTiculate mAtter Network
STP		Standard Temperature and Pressure
TEOM		Tapered Element Oscillating Monitor
TEPA		Taiwan Environmental Protection Administration
TNO		Netherlands Organisation for Applied Scientific Research
VOC		Volatile Organic Compounds
WDCA		World Data Centre for Aerosols
WHO		World Health Organization
XRF		X-Ray Fluorescence
I	$W\ m^{-2}$	Intensity of outgoing light
I0	$W\ m^{-2}$	Intensity of incoming light
P(Θ)		Aerosol phase function
P(Θ)		Aerosol phase function
R		Reflectance
R		Reflectance
Ra		Aerosol induced reflectance
Rm		Reflectance by molecular scattering
Rs		Surface reflectance

Acknowledgements

I am sincerely grateful for the contribution of many individuals to my PhD study.

Dr. Randall Martin is the best supervisor I have ever worked with. His exceptional scientific knowledge and creative thoughts are strong motivations for me to keep learning. He is always responsive to my questions and is patient when I have trouble understanding things. I appreciate him for taking the time to correct my every piece of writing word by word and for providing honest feedback on presentations. He also offers generous advice on career and professional life. His understanding makes it possible for me to balance life and work perfectly. I am very lucky to work with him over the course of my PhD program.

I would also like to thank my committee members, Dr. Glen Lesins for his insight and constructive suggestions on my work, and Dr. Rachel Chang for great conversations in a friendly way on many aspects like career development and parenting, etc.

Finally, I would like to thank my husband and my parents for their strong support and encouragement along the way.

It is my great honor to have these people in my life.

Chapter 1: Introduction

1.1 Aerosols

Aerosols are suspended particles or droplets in the atmosphere with a size typically between 0.01 μm and 10 μm in diameter (Pasceri and Friedlander, 1965). Despite their small size, aerosols strongly influence the climate, ecosystem and human health. Aerosols can alter the Earth's energy balance and thereby the climate by interacting with solar radiation through absorption and scattering (Ramanathan and Carmichael, 2008). Aerosols can also change the climate by enhancing cloud formation since they can serve as cloud condensation nuclei upon which cloud droplets form (Lohmann and Feichter, 2005). Aerosols contribute to acid deposition that damages aquatic wildlife and plants (Galloway et al., 1987). Aerosols are repository health hazard even below the level of the US national standard concentrations (12 $\mu g\ m^{-3}$; Crouse et al., 2012; Di et al., 2017). A thorough understanding of the processes and properties of aerosol particles in the atmosphere offers the opportunity to inform decisions affecting human health and the environment.

Aerosol size is a fundamental property that affects the formation, chemical composition, removal, and optical properties of aerosols. Atmospheric aerosols originate from two pathways: emissions of primary particulate matter and clustering of gas molecules (nucleation). Newly emitted or nucleated aerosols are primarily found in the ultrafine size range (aerodynamic diameter less than 0.1 μm), then rapidly grow to accumulation mode (diameter in 0.1 – 2.5 μm) particles through condensation, coagulation and non-precipitating cloud processing (Ramabhadran et al., 1976; Seinfeld and Ramabhadran, 1975). Further growth of accumulation particles to coarse particles (diameter larger than 2.5 μm) is slow as the condensation and coagulation rates decrease with particle mass and size (Ramabhadran et al., 1976; Seinfeld and Ramabhadran, 1975). Thus, accumulation mode is the most abundant contributor to mass in the atmosphere. In addition to the growth of accumulation particles, coarse particles (i.e. mineral dust or sea salt) also originate from the mechanical action of the

wind on the Earth's surface such as dust storm (Fairlie et al., 2007) or ocean wave breaking (Alexander et al., 2005).

The chemical composition of atmospheric aerosol varies with particle size. Fine aerosols (particle diameter < 2.5 μm) are typically composed of organic aerosols (OA), inorganic aerosols (i.e. sulfate, nitrate, ammonium), black carbon (BC) and trace metals (e.g. iron, lead, cadmium, nickel; Snider et al., 2016). Mineral dust, sea spray and biological particles (e.g. pollen, spores, plant fragments etc.) are major constituents of coarse particles (Lee et al., 2009; Pakkanen et al., 2001).

Depending on the formation processes, the chemical composition of aerosols is categorized into primary and secondary aerosols. Primary aerosols (i.e., BC, trace metals and coarse particles) are emitted directly into the atmosphere as particles. Secondary aerosols (i.e., sulfate, nitrate, ammonium, also termed together as secondary inorganic aerosols or SIA), are formed in the atmosphere through gas-to-particle conversion. For example, sulfate, nitrate, and ammonium aerosols are formed through the oxidation and condensation of their precursor gasses: sulfur dioxide (SO_2), NO_x (NO and NO_2) and ammonia (NH_3). Freshly emitted SO_2 and NO_x in the atmosphere is oxidized to H_2SO_4 and HNO_3 through a series of chemical reactions. Sulfate and nitrate aerosols are formed through the condensation of gas-phase H_2SO_4 and HNO_3 since they have a low vapor pressure. Ammonium aerosols are formed when atmospheric NH_3 gas neutralizes acids such as H_2SO_4 and HNO_3. In addition to SIA, secondary organic aerosols (SOA) are also formed through gas-to-particle conversions. The oxidation of gas-phase volatile organic carbons (VOCs, such as isoprene and benzene) in the atmosphere reduces their volatility by adding oxygen/nitrogen to organic molecules, facilitating their condensation onto particles or nucleation to form SOA. SOA can be formed alternatively by the polymerization of low-molecular-weight aldehydes on acidic aerosol surfaces (Jang et al., 2002; Kalberer et al., 2004). The amount of primary and secondary aerosol in the atmosphere varies considerably with time and location, depending on the local emission sources (Jimenez et al., 2009; Snider et al., 2016).

Aerosols and their precursors are emitted from natural and anthropogenic sources. Natural sources include soil (mineral dust and crustal elements), oceans (sea salt and dimethyl sulfide), forest fires (VOCs and BC), volcanoes (sulfate and SO_2) and biosphere (NH_3 and organics). Anthropogenic sources include fossil fuel combustion (SIA, BC, VOCs and trace metals), industrial processes (BC, SIA, organics, trace metals), biomass burning (BC and POA) and anthropogenic fugitive dust (crustal elements). Fossil fuel combustion and biomass burning dominate anthropogenic sources. It is projected that by 2040 anthropogenic sources of aerosol could be comparable to those from natural sources in mass (Wolf and Hidy, 1997).

Aerosols are removed from the atmosphere by wet and dry deposition. Wet deposition removes aerosol by incorporation into cloud droplets (in-cloud scavenging or washout) and subsequent precipitation (below-cloud scavenging or rainout). Dry deposition is the settling of aerosol in the absence of precipitation. Dry deposition is effective for nucleation particles by Brownian diffusion and for coarse particles by gravitational settling. Consequently, aerosols have a typical lifetime of 1-2 weeks in the lower troposphere (Gentry and Brock, 1968; Toossi and Novakov, 1985; Williams et al., 2002).

This thesis studies primarily on fine aerosol (diameter less than 2.5 μm) because it is typically used as an indicator in epidemiological analysis and disease burden assessment of adverse health effects associated with air pollution (Lippmann, 2014; Bell et al., 2015; Cohen et al., 2017; Di et al., 2017).

1.1.1 $PM_{2.5}$

$PM_{2.5}$ is fine particulate matter with aerodynamic diameter less than 2.5 μm. Given the small size, $PM_{2.5}$ can penetrate the thoracic region of the respiratory system, increasing the morbidity and mortality from respiratory and cardiovascular diseases, particularly in the elderly and children. (Bell et al., 2009; Di et al., 2017; Krall et al., 2016; Lippmann, 2014). It is estimated that more than 4 million premature deaths are attributable to outdoor $PM_{2.5}$ globally in 2015 (Cohen et al., 2017), making $PM_{2.5}$ one of the leading risk factors for global burden of disease. Due to these adverse effects, the World Health

Organization (WHO) recommends a maximum annual $PM_{2.5}$ exposure of 10 $\mu g/m^3$ (WHO, 2005). However, this recommendation is hardly met worldwide. The global population-weighted annual average $PM_{2.5}$ for 2010 is estimated as 32.6 $\mu g/m^3$, with the highest annual average of ~50 $\mu g/m^3$ in eastern and southern Asia (van Donkelaar et al., 2016). Therefore, further studies on $PM_{2.5}$, especially over Asia, is necessary for health benefits.

1.1.2 Black carbon

Black carbon (BC), also known as soot, is black-appearing carbonaceous aerosol with strong light absorption. The direct radiative forcing of BC is estimated as + 0.88 W m^2, with a total climate forcing of + 1.1 W/m^2, making BC the second most important pollutants in terms of climate forcing (only after carbon dioxide) in the atmosphere (Bond et al., 2013). The strong absorption of solar radiation by BC also contributes significantly to Arctic warming.

Arctic BC is primarily long-range transported from source regions such as Europe, Asia and North America (Koch, 2005; Shindell et al., 2008). BC is emitted from incomplete combustion of fossil fuels, biofuels and biomass (wood, forest, grass, solid waste, etc.). Within hours of emission, pure BC particles become mixed with other co-emitted aerosols from combustion (i.e., sulfate and organics) as they condense onto BC particles and coat the BC core. The mixing process coverts BC from hydrophobic to hydrophilic, since the chemical components of the coating (i.e. sulfate and SOA) are usually soluble (Abel et al., 2003). The e-folding time of the conversion is typically one day (Park, 2005). As BC become hydrophilic, its major removal from the atmosphere becomes wet deposition through in-cloud scavenging and precipitation. BC particles can be transported from their sources to the Arctic in several days to weeks (Heidam et al., 2004), long enough for BC to be well-mixed, aged and hydrophilic. There is also a moderate amount of Arctic BC transported from source regions on the fringes of the Arctic, such as boreal forest fires in Alaska (Warneke et al., 2009) and gas flaring emissions from oilfields in Siberia (Stohl et al., 2013).

In order to develop appropriate BC reduction strategies for Arctic warming, the geographical sources contributing to Arctic BC must be known quantitatively. Prior studies have presented very different or even contradictory results (Stohl, 2006; Stohl et al., 2007; Warneke et al., 2009). More studies are necessary to understand the differences and to better quantify geographical source contributions to Arctic BC.

1.1.3 Trace metals

Metals are important components of $PM_{2.5}$ with a minor contribution (< 1%) to $PM_{2.5}$ mass. Although low in concentrations, metals are responsible for a number of adverse health effects associated with $PM_{2.5}$. For example, cardiovascular and respiratory hospitalizations have been positively associated with aluminum (Al), calcium (Ca), silicon (Si), titanium (Ti) and potassium (K; Bell et al., 2013; Krall et al., 2016). Increased mortality risks are associated with transition metals such as iron (Fe), manganese (Mn) and Ti even under short-term exposure (Ostro et al., 2007; T. Burnett et al., 2000).

Trace metals contain a wealth of information about $PM_{2.5}$ sources. K concentrations are strongly associated with biomass burning (Pachon et al., 2013; Tanner et al., 2001). Crustal elements (i.e., Si, Al, Ca, Mg and Ti) are useful for identifying dust sources including road dust and mineral dust (Chang et al., 2017; Khodeir et al., 2012a). Heavy metals (i.e., Cd, Pb and As) can indicate industrial sources of $PM_{2.5}$ (Chang et al., 2017; Okuda et al., 2007; Pacyna and Pacyna, 2001).

Due to heterogeneous emission sources and short atmospheric lifetimes (days), trace metal concentrations can vary by several orders of magnitude from region to region, presenting a challenge for understanding their distributions. Nonetheless, recent developments in chemical transport models are promising in addressing the problem.

1.2 Monitoring of atmospheric aerosols

The health and climate concerns of aerosols have motivated the development of national and international monitoring networks and campaigns. In situ observations provide comprehensive measurements of aerosols mass, composition, and optical properties. There have been various extensive operational aerosol monitoring networks across North America and Europe since the 1970s (Chow, 2002; Holben et al., 1998; Tørseth et al., 2012). A large number of monitoring networks have been established in China during the past decade to monitor major air pollutants including $PM_{2.5}$. Even in the Arctic, there have been several ground monitoring stations in the North American and European Arctic to measure aerosol characteristics in a pristine environment. These worldwide in situ observations provide valuable information on aerosol properties.

The emergence of satellite remote sensing has allowed unprecedented spatial and temporal observational coverage of the Earth, which has considerably improved our understanding of aerosol loadings, optical properties and vertical profiles (Lee et al., 2009). Traditional low orbit (polar) satellite instruments provide aerosol measurements on a global coverage with fine spatial resolutions. Recent geostationary satellite instruments allow for regional aerosol retrievals at high temporal resolutions. Satellite remote sensing combined with in situ measurements offer comprehensive insight into aerosol properties from different perspectives.

1.2.1 In situ measurements of aerosol mass

Ambient aerosol samples are commonly collected by an air sampler in which aerosols travel through a size-selective inlet and are collected on a quartz fiber filter. The total mass of aerosol samples (typically PM_{10} or $PM_{2.5}$) can be determined either by the manual weighting of the filter before and after sampling or by automatic methods commonly including Tapered Element Oscillating Microbalances (TEOM) and beta attenuation monitors (BAM). TEOM measures aerosol mass on a filter by its effect on the resonant frequency of a vibrating support, while BAM measures the aerosol mass by its

absorption of electrons emitted by a weak beta-source. After the measurement of aerosol mass, samples are subsequently analyzed for their composition including BC, trace metals and water-soluble ions.

BC mass can be estimated by three techniques responding to different properties of BC. The optical method used by an aethalometer (Bond et al., 1999) or a particle soot absorption photometer (PSAP) converts the light absorption of BC to BC mass concentrations by assuming a mass absorption coefficient (MAC). Measurements based on this method are known as equivalent BC (EBC). The thermal method (Huang et al., 2006) measures non-volatile elemental carbon (EC) by heating the filter to evaporate volatile organic carbon out of the total carbon. The refractory method used by a single particle soot photometer (SP2) measures the incandescence of individual particles heated to 3600℃. Measurements based on the refractory method are known as refractory BC (rBC). Since different methods respond to different properties of BC and none of these methods are uniquely sensitive to BC, the measurement of BC mass is subject to large uncertainties (Bond et al., 2013; Sharma et al., 2017).

Trace metals are often measured by x-ray fluorescence (XRF) spectrometry. This method is based on the principle that individual atoms, when excited by an external energy source, emit X-ray photons of a characteristic energy. By counting the number of photons of each wavelength emitted from the sample, the elements present may be identified and quantified.

1.2.2 Satellite remote sensing of aerosol optical properties

Satellite remote sensing measures aerosol abundance through the total atmospheric column based on the fact that aerosol reflects and absorbs sunlight. The extinction of light passing through the atmosphere can be described by Beer's law as,

$$I=I_0 \exp(-\tau) \quad (1.1)$$

where I_0 and I are the intensity of incoming and outgoing light, respectively, at a particular wavelength. τ is the optical depth of traversing medium. Aerosol optical depth (AOD) describes light extinction through the atmospheric column due to the presence of aerosol, which is described as,

$$\tau = \int_{z}^{z_{TOA}} b_{ext} dz \tag{1.2}$$

where z is the length of light path, b_{ext} is light extinction coefficient that is determined by aerosol size distribution and extinction efficiency.

AOD can be retrieved by satellite remote sensing through the aerosol reflectance of sunlight. Aerosol reflectance (R_a) is retrieved by

$$R_a(\Theta) \approx R(\Theta) - R_m(\Theta) - R_s(\Theta) \tag{1.3}$$

where R is total atmospheric column reflectance retrieved by satellite. R_m and R_s are reflectance by gas molecules and the Earth surface, respectively. Θ is viewing angle. Aerosol reflectance is then converted to AOD by the following equation,

$$AOD \approx \frac{R_a(\Theta)}{P(\Theta)\varpi} \tag{1.4}$$

where P is aerosol phase function that describes the angular distribution of light scattered by aerosol. ϖ is aerosol single scattering albedo that quantifies the scatter fraction of incident radiation.

1.3 Chemical transport model and inverse modeling

In addition to direct measurements, aerosol properties such as concentrations and optical properties can also be calculated through modeling. Chemical transport models solve for the temporal evolution of atmospheric aerosols using meteorological datasets, emission

inventories, and equations that represent the physics and chemistry of the atmosphere. Aerosol properties calculated by chemical transport models have proven to be a valuable source of information with complete horizontal and vertical global coverage at high temporal resolution.

1.4 Goal of this work

In situ measurements, satellite remote sensing and chemical transport models each provide valuable insight into aerosol properties. This work brings together these sources, drawing on their individual strength to investigate global and regional aerosol concentrations, chemical composition and transport.

Given the adverse health effects associated with $PM_{2.5}$, it is importance to understand $PM_{2.5}$ distributions, especially in China where close to 1 million premature deaths are attributable to $PM_{2.5}$ in 2013 (HEI, 2016). The first part of this thesis estimates the distribution of $PM_{2.5}$ and its chemical composition over eastern China by using the first geostationary satellite instrument (GOCI) for air quality and the GEOS-Chem chemical transport model. This work was published in Atmospheric Chemistry and Physics in 2015.

The Arctic is warming at a rate two times faster than anywhere on the Earth (NOAA, 2017). BC has a considerable contributes to this warming due to its strong absorption of sunlight. However, geographical sources of BC remain uncertain given limited observations in the Arctic and missing emission sources in previous modelling studies. The second part of this thesis interprets the most recently aircraft and ground-based measurements in the Arctic with the GEOS-Chem model to better understand sources of Arctic BC. This work was published in Atmospheric Chemistry and Physics in 2017.

Airborne metals are responsible for a number of adverse health effects associated with $PM_{2.5}$ because of their toxicity and carcinogenicity. Studies on the health effects of airborne trace metals are limited by the strong spatial heterogeneity of trace metal distributions due to their complex emission sources and short lifetimes. The last part of this thesis presents the first

simulation of 12 trace metals: Si, Ca, Al, Fe, Ti, Mn, K, Mg, As, Cd, Ni and Pb over the continental North America for 2013 at a fine resolution of 0.25° x 0.3125° by using the GEOS-Chem chemical transport model. Results from this simulation provide valuable basis for further investigations into the health effects of trace metals and $PM_{2.5}$.

Chapter 2: Estimating Ground-level $PM_{2.5}$ in Eastern China Using Aerosol Optical Depth Determined from the GOCI Satellite Instrument

Authors: Junwei Xu[1], Randall V. Martin[1,2], Aaron van Donkelaar[1], Jhoon Kim[3], Myungjie Choi[3], Qiang Zhang[4,5], Guannan Geng[4,5], Yang Liu[6], Zongwei Ma[6,7], Lei Huang[7], Yuxuan. Wang[4,8,9], Hongbin Chen[10], Huizhen Che[11], Po-hsiung Lin[12], Neng-huei Lin[13]

[1]Department of Physics and Atmospheric Science, Dalhousie University, Canada
[2]Harvard-Smithsonian Center for Astrophysics, Cambridge, Massachusetts, USA
[3]Department of Physics and Atmospheric Sciences, Yonsei University, Seoul, South Korea
[4]Ministry of Education Key Laboratory for Earth System Modeling, Center for Earth System Science, Institute for Global Change Studies, Tsinghua University, Beijing, China
[5]State Key Joint Laboratory of Environment Simulation and Pollution Control, School of Environment, Tsinghua University, Beijing, China
[6]Department of Environmental Health, Rollins School of Public Health, Emory University, Atlanta, GA, United States
[7]State Key Laboratory of Pollution Control and Resource Reuse, School of the Environment, Nanjing University, China
[8]Department of Marine Sciences, Texas A&M University at Galveston, Galveston, Texas, USA
[9]Department of Atmospheric Sciences, Texas A&M University, College Station, Texas, USA
[10]Institute of Atmospheric Physics, Chinese Academy of Sciences, China
[11]Institute of Atmospheric Composition, Chinese Academy of Meteorological Sciences, China
[12]Department of Atmospheric Sciences, National Taiwan University, Taiwan
[13]Department of Atmospheric Sciences, National Central University, Taiwan

Article published in Atmospheric Physics and Chemistry, 15, 13133-13144, 2015. All text, figures and results were contributed by the first author.

2.1 Abstract

We determine and interpret fine particulate matter ($PM_{2.5}$) concentrations in eastern China for January to December 2013 at a horizontal resolution of 6 km from aerosol optical depth (AOD) retrieved from the Korean Geostationary Ocean Color Imager (GOCI) satellite instrument. We implement a set of filters to minimize cloud contamination in GOCI AOD. Evaluation of filtered GOCI AOD with AOD from the Aerosol Robotic Network (AERONET) indicates significant agreement with mean fractional bias (MFB) in Beijing of 6.7% and northern Taiwan of -1.2%. We use a global chemical transport model (GEOS-Chem) to relate the total column AOD to the near-surface $PM_{2.5}$. The simulated $PM_{2.5}$/AOD ratio exhibits high consistency with ground-based measurements in Taiwan (MFB= -0.52%) and Beijing (MFB= -8.0%). We evaluate the satellite-derived $PM_{2.5}$ versus the ground-level $PM_{2.5}$ in 2013 measured by the China Environmental Monitoring Center. Significant agreement is found between GOCI-derived $PM_{2.5}$ and *in-situ* observations in both annual averages (r^2=0.66, N=494) and monthly averages (relative RMSE=18.3%), indicating GOCI provides valuable data for air quality studies in Northeast Asia. The GEOS-Chem simulated chemical composition of GOCI-derived $PM_{2.5}$ reveals that secondary inorganics (SO_4^{2-}, NO_3^-, NH_4^+) and organic matter are the most significant components. Biofuel emissions in northern China for heating increase the concentration of organic matter in winter. The population-weighted GOCI-derived $PM_{2.5}$ over eastern China for 2013 is 53.8 μg m^{-3}, with 400 million residents in regions that exceed the Interim Target-1 of the World Health Organization.

2.2 Introduction

Fine particulate matter with aerodynamic diameter less than 2.5 μm ($PM_{2.5}$) is a robust indicator of mortality and other negative health effects associated with ambient air pollution (Goldberg et al., 2008; Laden et al., 2006). It is estimated that more than three million people lost their lives prematurely due to $PM_{2.5}$ in 2010 (Lim et al., 2012), of which one million occurred in East Asia (Silva et al., 2013). In China, there have already been several episodes with $PM_{2.5}$ described as "beyond index" levels. Thus, it is of paramount importance to monitor $PM_{2.5}$ concentrations across China. Satellite remote sensing has a high potential to monitor $PM_{2.5}$.

Satellite retrievals of aerosol optical depth (AOD), which provide a measure of the amount of light extinction through the atmospheric column due to the presence of aerosols, have long been

recognized to relate to ground level $PM_{2.5}$ (Wang and Christopher, 2003). Many studies have developed advanced statistical relationships to estimate with high accuracy surface $PM_{2.5}$ from satellite AOD (Liu et al., 2009; Kloog et al., 2012; Hu et al., 2013). For example, Ma et al. (2014) estimated $PM_{2.5}$ concentrations in China from satellite AOD by developing a national-scale geographically weighted regression model, and found strong agreement (r^2=0.64) with ground measurements.

In addition to empirical statistical methods, satellite AOD can also be geophysically related to surface $PM_{2.5}$ by the use of a chemical transport model to simulate the $PM_{2.5}$ to AOD relationship (Liu et al., 2004; van Donkelaar et al., 2010). This approach was first demonstrated using data from the Multiangle Imaging Spectroradiometer (MISR) aboard NASA's Terra satellite over the United States for 2001 (Liu et al., 2004). Van Donkelaar et al. (2006, 2010) extended this approach to estimate $PM_{2.5}$ from AOD retrieved from both the MODIS (Moderate Resolution Imaging Spectroradiometer) and the MISR satellite instruments, and developed a long-term global estimate of $PM_{2.5}$ at a spatial resolution of approximately 10 km x 10 km. Boys et al. (2014) used AOD retrieved from MISR and the SeaWiFS (Sea-viewing Wide Field-of-view Sensor) to produce a 15-year (1998−2012) global trend of ground-level $PM_{2.5}$. These previous studies have proven to be globally effective, but more detailed regional investigation is needed in densely polluted and populated regions like China.

The Geostationary Ocean Color Imager (GOCI) is the first geostationary satellite instrument that offers multi-spectral aerosol optical properties in Northeast Asia (Park et al., 2014). GOCI has a high observation density of 8 retrievals/day (hourly retrievals from 09:00 to 16:00 Korean Standard Time) over a location, which exceeds the retrieval density of traditional low-Earth polar-orbiting satellite instruments. Thus, GOCI is promising for more detailed investigations on aerosol properties in highly polluted and populated regions including eastern China.

In this study, we estimate ground-level $PM_{2.5}$ in eastern China for 2013 at a horizontal resolution of 6 km by 6 km, by using AOD retrieved from GOCI, coupled with the relationship of $PM_{2.5}$ to AOD simulated by a chemical transport model (GEOS-Chem). Section 2 describes the approach and data. Section 3 evaluates the GOCI AOD, the simulated $PM_{2.5}$ to AOD relationship, and the GOCI-derived $PM_{2.5}$ using recently available ground-level measurements from the China

Environmental Monitoring Center (http://113.108.142:20035/emcpublish/). We also interpret the GOCI-derived $PM_{2.5}$ by using the GEOS-Chem model to estimate its chemical composition. Section 4 summarizes the major findings and potential future improvements of the current analysis.

2.3 Methods

2.3.1 Aerosol optical depth from the GOCI satellite instrument

GOCI operates onboard the Communication, Ocean, and Meteorology Satellite (COMS) that was launched in 2010 in Korea (Lee et al., 2010). The spatial coverage of GOCI is 2500 km x 2500 km in Northeast Asia, including eastern China, the Korean peninsula and Japan (Kang et al., 2006). GOCI has eight spectral channels for aerosol retrievals, including six visible bands at 412, 443, 490, 555, 660, 680 nm and two near infrared bands at 745 and 865 nm (Park et al., 2014). The Level 2 AOD products are retrieved at a spatial resolution of 6 km by 6 km, using a clear-sky composite method for surface reflectance and a lookup table approach based on AERONET observations (Lee et al., 2010; Lee et al., 2012).

A challenge using GOCI to detect aerosols in the atmosphere is the absence of mid-infrared (IR) channels to detect clouds, which means that significant errors could be induced in the estimates of AOD. The operational GOCI products screen clouds based on spatial variability and threshold tests at each 6 km x 6 km pixel in combination with a meteorological imager that has 4 IR channels (at 3.7 μm, 6.7 μm, 10.8 μm, 12 μm wavelengths) at 4 km by 4 km resolution onboard the same satellite (Cho et al., 2006). However, as will be shown here cloud contamination still occurs. Therefore, we apply a set of spatial filters following Hyer et al. (2011) and temporal filters to further eliminate cloud contamination in GOCI AOD. The filters include 1) a buddy check that sets a minimum number of 15 retrievals per 30 km x 30 km grid cell, 2) a local variance check to eliminate grid cells where the coefficient of variation of AOD is larger than 0.5 within the surrounding 5 x 5 grid cells and 3) a diurnal variation check that excludes grid cells with diurnal variation (maximum – minimum) of AOD larger than 0.74 which is the 90^{th} percentile of diurnal variation of AERONET AOD in Beijing and northern Taiwan for 2013. In this study, we use GOCI AOD for Jan-Dec 2013 to derive ground-level $PM_{2.5}$ in eastern China.

2.3.2. Aerosol optical depth from AERONET ground-based measurements

The Aerosol Robotic Network (AERONET) is a globally distributed network of CIMEL Sun photometers (Holben et al., 1998) that provide multi-wavelength AOD measurements with a low uncertainty of < 0.02 (Holben et al., 2001). Here we use AERONET Level 1.5 cloud screened data (Smirnov et al., 2000) for Jan-Dec 2013 from 4 stations within the GOCI domain: Beijing, Beijing-CAMS, Taipei_CWB and EPA-NCU. AERONET Level 2 data for 2013 are not available for some stations discussed in this paper. Thus, we use Level 1.5 for consistency. We compared Level 2 and Level 1.5 data for 2013 for stations that do have Level 2 available, and found Level 1.5 AOD is highly consistent with Level 2 AOD with RMSE of 0.01-0.02 (relative RMSE of 2%-7%). Criteria for selecting an AERONET station are 1) a $PM_{2.5}$ ground monitor has to be located within 10 km and 2) a complete time series of AOD data records for the period of study has to be available. Beijing and Beijing-CAMS stations are located in downtown Beijing, with the closest available $PM_{2.5}$ monitors 9.5 km and 7.5 km away, respectively. However, due to interrupted time series of $PM_{2.5}$ records at both these stations, we combine the AERONET AOD from the Beijing and Beijing-CAMS stations and $PM_{2.5}$ from the corresponding two *in-situ* ground-based sites as a "combined Beijing" site. Taipei_CWB and EPA-NCU stations are located in populated northern Taiwan, with nearly collocated $PM_{2.5}$ monitors (< 3 km). We similarly combine the Taipei_CWB and EPA-NCU as "northern Taiwan" site. We use these sites to evaluate GOCI AOD and the relationship between AOD and $PM_{2.5}$ simulated by a global chemical transport model.

2.4 Simulation of the relationship between AOD and $PM_{2.5}$ by GEOS-Chem

We use the GEOS-Chem chemical transport model (version 9-01-03; http://geos-chem.org) to calculate the spatiotemporally resolved relationship between ground-level $PM_{2.5}$ and satellite-retrieved column AOD.

Our nested GEOS-Chem simulation at 1/2° x 2/3° spatial resolution with 47 vertical levels (14 levels in the lowest 2 km) is driven by assimilated meteorology from the Goddard Earth Observing System (GEOS-5). A global simulation at 2° x 2.5° spatial resolution is used to provide boundary conditions for the nested domain (Wang et al., 2004). We spin up the model for one month before each simulation to remove the effects of initial conditions on the aerosol simulation.

GEOS-Chem includes a fully coupled treatment of tropospheric oxidant-aerosol chemistry (Bey et al., 2001; Park et al., 2004). The GEOS-Chem aerosol simulation includes the sulfate-nitrate-ammonium system (Park et al., 2004; Pye et al., 2009), primary (Park et al., 2003) and secondary (Henze et al., 2006; Henze et al., 2008; Liao et al., 2007; Fu et al., 2008) organics, mineral dust (Fairlie et al., 2007), and sea salt (Jaegle et al., 2011). We estimate the concentration of organic matter (OM, which includes elements such as hydrogen, oxygen and nitrogen) from the simulated primary organic carbon (OC) using spatially and seasonally resolved values from OMI (Ozone Monitoring Instrument) NO_2 and AMS (Aerosol Mass Spectrometer) measurements following Philip et al. (2014). Gas-aerosol phase partitioning is simulated using the ISORROPIA II thermodynamic scheme (Fountoukis and Nenes, 2007). GEOS-Chem calculates AOD using relative humidity dependent aerosol optical properties following Martin et al. (2003). Dust optics are from Ridley et al. (2012).

Anthropogenic emissions are based on the Multi-resolution Emission Inventory for China (MEIC; http://www.meicmodel.org) for 2010, and the Zhang et al. (2009) inventory for surrounding East Asia regions for 2006. Both inventories are scaled to the simulation year (2012-2013), following Ohara et al. (2007). Non-anthropogenic emissions include biomass burning emissions (GFED-3) (Mu et al., 2011), biogenic emissions (MEGAN) (Guenther et al., 2006), soil NO_x (Yienger and Levy, 1995; Wang et al., 1998), lightning NO_x (Murray et al., 2012), aircraft NO_x (Wang et al., 1998; Stettler et al., 2011), ship SO_2 from EDGAR (Olivier et al., 2001) and volcanic SO_2 emissions (Fischer et al., 2011). HNO_3 concentrations are artificially decreased to 75% of their values at each timestep following Heald et al. (2012) to account for regional bias (Wang et al., 2013). Emissions are distributed into the lower mixed layer, with a correction to the GEOS-5 predicted nighttime mixing depths following Heald et al. (2012) and Walker et al. (2012).

We apply GEOS-Chem to simulate daily relationships between ground level $PM_{2.5}$ and column AOD, specifically $PM_{2.5}$/AOD. $PM_{2.5}$ concentrations are calculated at 35% relative humidity for consistency with *in-situ* measurements. For consistency with GOCI AOD and $PM_{2.5}$ ground-based measurements, we sample the simulated AOD only from hours that GOCI has retrievals (00:00 - 07:00 UTC), and calculate the simulated daily $PM_{2.5}$ from 24-hour averages as reported for the ground-based $PM_{2.5}$ measurements. The simulation period is May 2012 - April 2013 as the GEOS-

5 meteorological fields are not available afterward. The mismatch with observations for May-Dec 2013 has the potential to degrade performance, but as will be shown here no clear loss of quality is apparent.

2.5 *In-situ* $PM_{2.5}$ measurements

We collect $PM_{2.5}$ measurements from 494 monitors to evaluate the GOCI-derived values. *In-situ* $PM_{2.5}$ daily measurements in Mainland China for 2013 are primarily from the official website of the China Environmental Monitoring Center (CEMC; http://113.108.142:20035/emcpublish/). Data are also collected from some provinces (e.g. Shandong, Zhejiang) and municipalities (e.g. Beijing and Tianjin) with additional sites that are not included in the CEMC website. Daily *in-situ* $PM_{2.5}$ data in northern Taiwan for 2013 are from the Taiwan Environmental Protection Administration (TEPA; http://taqm.epa.gov.tw). The *in-situ* $PM_{2.5}$ data in both Mainland China and northern Taiwan are measured by a collection of the Tapered Element Oscillating Microbalance Methods (TEOMs) and beta-attenuation methods (BAMs) with some TEOMs being heated to 30 °C and others to 50 °C (CNAAQS GB3095-2012, 2012; http://taqm.epa.gov.tw). The specific instrument (BAMs or TEOMs) used by each monitoring site is unknown. The effective relative humidity of the resultant $PM_{2.5}$ measurement likely varies diurnally and seasonally as a function of the ambient temperature. Semivolatile losses are expected from the TEOMs. The network design appears to include compliance objectives that may affect monitor placement. Despite these issues, we use the monitoring data to evaluate our satellite-derived $PM_{2.5}$ since the monitoring data offer valuable information about ground-level $PM_{2.5}$ concentrations. We also collect $PM_{2.5}$ measurements from a monitor in Beijing as part of the Surface PARTiculate mAtter Network (SPARTAN; www.spartan-network.org) using a three-wavelength nephelometer and an impaction filter sampler (Snider et al., 2015). The SPARTAN, CEMC and TEPA $PM_{2.5}$ monitoring data combined with AERONET AOD are used to estimate the empirical relationship between $PM_{2.5}$ and AOD, and to further evaluate the relationship simulated by the model.

2.6 Statistical Terms

Root mean square error (RMSE), relative root mean square error (rRMSE), mean fractional bias (MFB) and mean fractional error (MFE) are defined as

$$\text{RMSE} = \sqrt{\frac{1}{\text{N}}\sum_{\text{i=1}}^{\text{N}}(\text{S}_i - \text{O}_i)^2} \quad (1)$$

$$\text{rRMSE} = \frac{\text{RMSE}}{\frac{1}{N}\sum_{\text{i=1}}^{\text{N}}\text{O}_i} \quad (2)$$

$$\text{MFB} = \frac{1}{N}\sum_{i=1}^{N}\frac{(S_i - \text{O}_i)}{(\frac{S_i + \text{O}_i}{2})} \text{ x } 100\% \quad (3)$$

$$\text{MFE} = \frac{1}{N}\sum_{i=1}^{N}\frac{|S_i - \text{O}_i|}{(\frac{S_i + \text{O}_i}{2})} \text{ x}100\% \quad (4)$$

where S_i is the satellite-derived value of the parameter in question, O_i is the corresponding observed value, and N is the number of observations.

Coefficient of variation (CV)is defined as

$$\text{CV} = \frac{\text{Standard deviation}}{\text{Mean}} \quad (5)$$

2.7 Results and Discussion

2.7.1 Evaluation of satellite AOD and the simulated relationship between $PM_{2.5}$ and AOD

Figure 2-1 shows the effects of our cloud-screening filters on GOCI AOD. The left panel shows GOCI true color images from 5 July 2013 at 10:30 (top) and 11:30 (bottom) Korean Standard Time. The boxes identify challenging regions with thick white cloud, dark cloud-free oceans and grey shading that appears to be thin cloud. The operational GOCI AOD retrievals, shown in the middle panel, correctly exclude thick clouds, but report high AOD for the potentially thin clouds. Although these grey regions could contain aerosol, we err on the side of caution. Application of our additional temporal and spatial cloud filters removes the suspicious pixels from the original GOCI data, as shown in the right panel. Our filters reject 10.3% of all the operational GOCI AOD data investigated in this study. We evaluate the cloud filters further below.

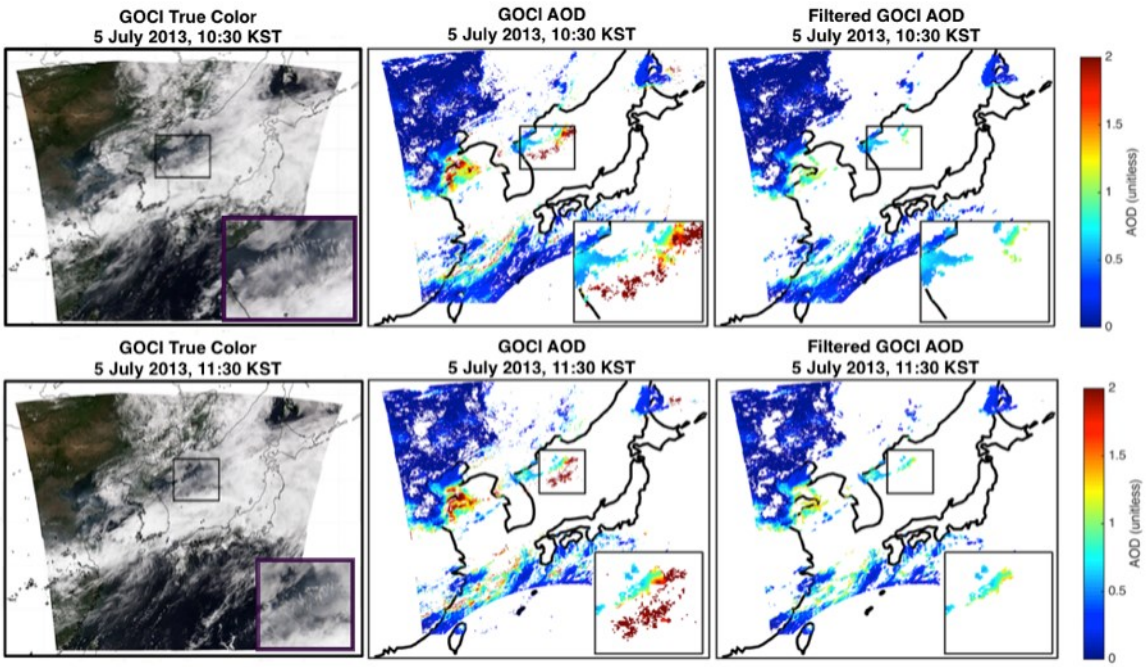

Figure 2-1: The GOCI granules from 5 July 2013, 10:30 (top) and 11:30 (bottom) Korean Standard Time. From left to right on each panel are the GOCI true color images, the operational AOD retrievals and the AOD retrievals after applying temporal and textual filters to reduce cloud contamination. The boxes highlight examples of challenging cloud fields, and are enlarged within the lower right subplot of each panel.

Figure 2-2 (top) shows monthly averages of coincident filtered hourly GOCI and AERONET AOD for Jan-Dec 2013 at combined Beijing and northern Taiwan stations. GOCI AOD is highly consistent with AERONET observations with MFB of 6.7% in Beijing and -1.2% in Taiwan. GOCI AOD and AERONET AOD are positively skewed at both stations, and the skewness is reduced in GOCI AOD at both stations due to more records for extremely small AOD (< 0.04) in GOCI products. The relatively larger rRMSE between GOCI and AERONET AOD in northern Taiwan may reflect the fewer observations there.

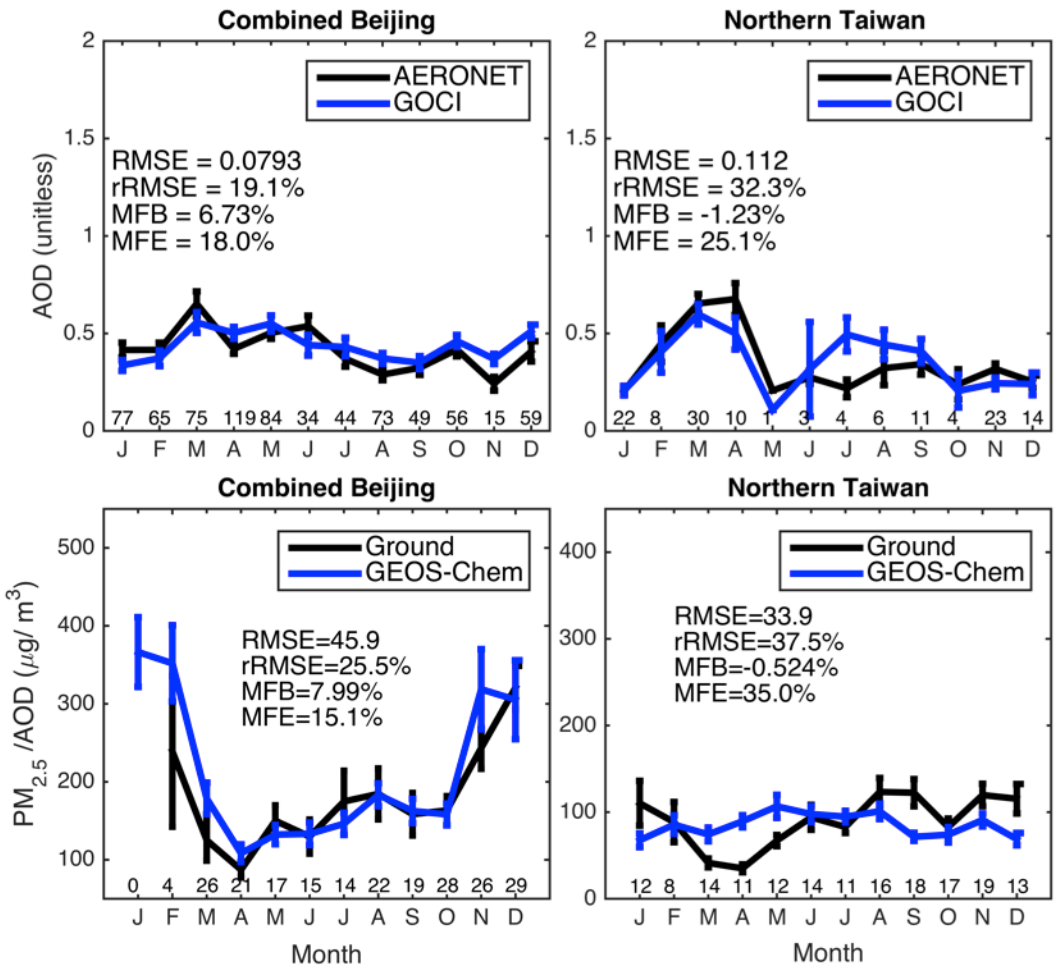

Figure 2-2: Top: monthly time series of AOD from AERONET and GOCI for January–December 2013. Numbers above the x axis denote the number of coincident hourly observations in each month. Bottom: monthly averages of $PM_{2.5}$ =AOD from ground measurements and the GEOS-Chem simulation at AERONET sites. The ground-based ratio is sampled from daily ground $PM_{2.5}$ coincident with AERONET AOD for January–December 2013. The GEOSChem simulation is for May 2012–April 2013, non-coincident with the ground-based ratio for May–December 2013. Numbers above the x axis denote the number of daily ground-based observations in each month. Error bars represent standard errors. Statistics are root mean square error (RMSE), relative root mean square error (rRMSE), mean fractional bias (MFB) and mean fractional error (MFE).

We investigate the filtered diurnal variation of GOCI AOD at the above AERONET stations and find the level of AOD is uniform within a day (e.g. the coefficient of variation in Beijing is 0.1), similar to AERONET observations.

The effect of excluding our cloud-screening filters is negligible for coincident comparisons with AERONET since AERONET is already cloud-screened. The exclusion of our cloud filters for a non-coincident comparison that includes all GOCI data would introduce significant error versus AERONET observations, increasing rRMSE by a factor of 1.7 - 3.3 in Beijing and northern Taiwan.

Changing the buddy check threshold in our cloud filters from 15 to 10 would significantly underestimate AOD especially in northern Taiwan where the MFB would increase from -1.2% to -15.0%. Decreasing the threshold of local variance check to 0.4 has little influence (< 0.1%) for rRMSE, MFB and MFE, but would have larger influence on GOCI-derived $PM_{2.5}$ as will be shown later. Limiting the diurnal variation of GOCI AOD to the 80th percentile of diurnal variations in observations would introduce bias (rRMSE would increase by 4% in Beijing) to GOCI AOD. As will be shown here, GOCI-derived $PM_{2.5}$ offers an additional test of cloud screening filters. Figure 2-2 (bottom) shows the relationship between the ground level $PM_{2.5}$ and the columnar AOD as simulated by GEOS-Chem and from ground-based measurements. The measured ratio in Beijing has pronounced seasonal variation with values high in winter and low in spring. The measured ratio in northern Taiwan exhibits little seasonal variation. The annual mean GEOS-Chem $PM_{2.5}$/AOD ratio well reproduces the ground-based measurements despite the temporal inconsistency of the two metrics for May - Dec. The simulation captures the pronounced seasonal variation in Beijing and the comparably aseasonal behavior in northern Taiwan. The simulated seasonal variation of $PM_{2.5}$/AOD in Beijing arises from the seasonal variation of mixed layer depth (factor of 2 higher in summer than winter) combined with the near-constant columnar AOD throughout the year as shown in Fig. 2-2 (top).

Snider et al. (2015) interpreted coincident measurements of AOD, $PM_{2.5}$, and nephelometer measurements of aerosol scattering and found that the temporal variation of the $PM_{2.5}$/AOD ratio in Beijing was primarily driven by the vertical profile in aerosol scattering. We examine the seasonal variation in the simulated $PM_{2.5}$/AOD and similarly find that the ratio of ground-level aerosol scatter to columnar AOD contributes most (89%) of the monthly variability in the $PM_{2.5}$/AOD ratio in Beijing.

2.7.2 Evaluation of ground-level $PM_{2.5}$ derived from GOCI AOD

Figure 2-3 shows the seasonal and annual distribution of $PM_{2.5}$ over East Asia at a spatial resolution of 6 km by 6 km for 2013. In both GOCI-derived and measured $PM_{2.5}$, winter concentrations in eastern China exceed 100 $\mu g\ m^{-3}$ over vast regions, with lower values in summer. Both GOCI-derived and in-situ measurements reveal that $PM_{2.5}$ in northern China is higher than in southern China, especially for the Beijing, Hebei and Shandong provinces where

the annual $PM_{2.5}$ is almost 100 μg m^{-3} or more. Prior work has attributed this regional enhancement to high emission rates (Zhao et al., 2013; Zhang et al., 2013) that in part arises from emissions when producing goods for exports (Jiang et al., 2015).

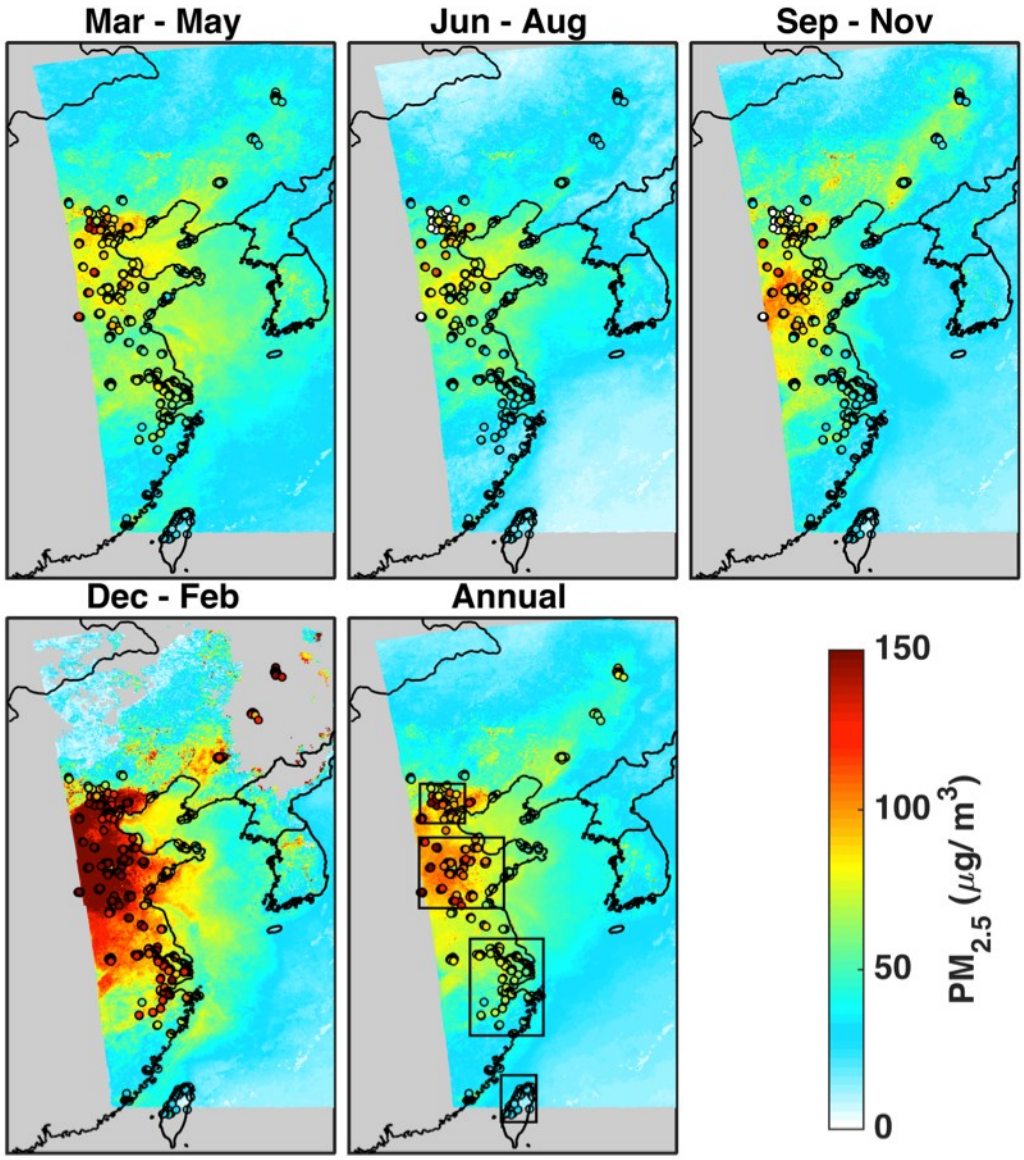

Figure 2-3: Seasonal and annual distribution of $PM_{2.5}$ concentrations at 6 km by 6 km resolution over East Asia for 2013. The background color indicates averages of GOCI-derived daily surface $PM_{2.5}$ concentrations. Filled circles represent averages of daily ground-based measurements of $PM_{2.5}$. Gray denotes missing values. Boxes in the annual map denote regions used for monthly comparisons in Fig. 2-5 from top to bottom: Beijing and surrounding areas, Shandong and surrounding regions, Shanghai and surrounding areas and northern Taiwan.

Figure 2-4 compares annual and seasonal averages of daily ground-measured $PM_{2.5}$ from 494 sites with coincident daily GOCI-derived $PM_{2.5}$ from pixels that contain the ground-based sites. A significant correlation (r^2=0.66, N=494) with a slope near unity (1.01) is found in the annual scatter plot. The slope remains near unity (0.95-1.01) in seasonal scatter plots. The weaker correlation for all four seasons implies random representativeness differences between point *in situ* measurements and area-averaged satellite values when data density diminishes. Semivolatile losses from some *in situ* instruments (TEOMs) might contribute to scatter in winter when nitrate constitutes a larger fraction of $PM_{2.5}$. We focus on more meaningful aggregated measurements. Using the same technique, we also estimated $PM_{2.5}$ from MODIS Collection 6 AOD for 2013, and found GOCI-derived $PM_{2.5}$ achieves greater consistency than MODIS-derived $PM_{2.5}$ when compared with ground-based measurements (slope=1.1, r^2=0.61). GOCI-derived $PM_{2.5}$ also corrects the significant underestimation of $PM_{2.5}$ from GEOS-Chem (slope=0.68, r^2=0.85) when compared with ground measurements.

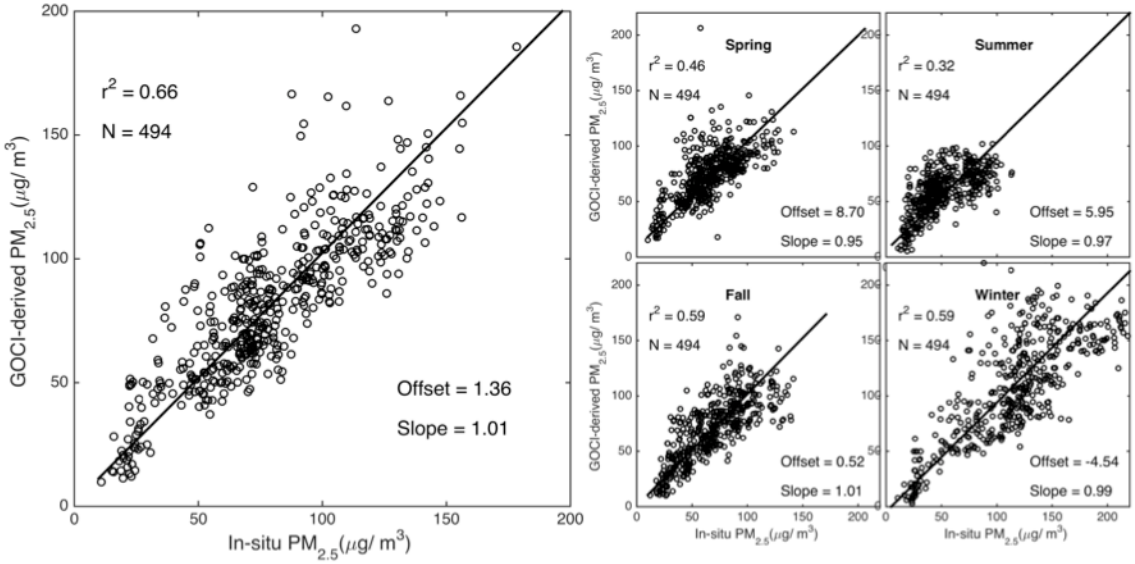

Figure 2-4: Scatterplots of the annual mean (left) and seasonal mean (right) GOCI-derived PM2.5 for 2013 against PM2.5 from 494 ground monitors over the GOCI domain in eastern China.

Figure 2-5 shows monthly averages of GOCI-derived $PM_{2.5}$ and *in-situ* measurements at four regions outlined in Fig. 2-3. Regions are selected based on the level of $PM_{2.5}$ concentration and the population of residents. A high degree of consistency is found in all regions. Both datasets show more seasonal variation in northern regions like Beijing and Shandong than southern regions

like Shanghai and northern Taiwan. Both indicate that $PM_{2.5}$ concentrations in northern regions are generally higher than in southern regions. The exclusion of our cloud screening filters from the GOCI AOD would introduce significant bias in GOCI-derived $PM_{2.5}$ versus ground-based measurements especially in summer, increasing rRMSE by a factor of 1.7 – 5.3 in all four regions. Changing the threshold of local variance check in our cloud filters to 0.4 would introduce bias by restricting the variation of $PM_{2.5}$ concentrations. For example, GOCI-derived $PM_{2.5}$ would be generally underestimated in Beijing areas (rRMSE=16.6% and MFB=-6.8%) and Shandong areas (rRMSE=16.6% and MFB=-3.42%).

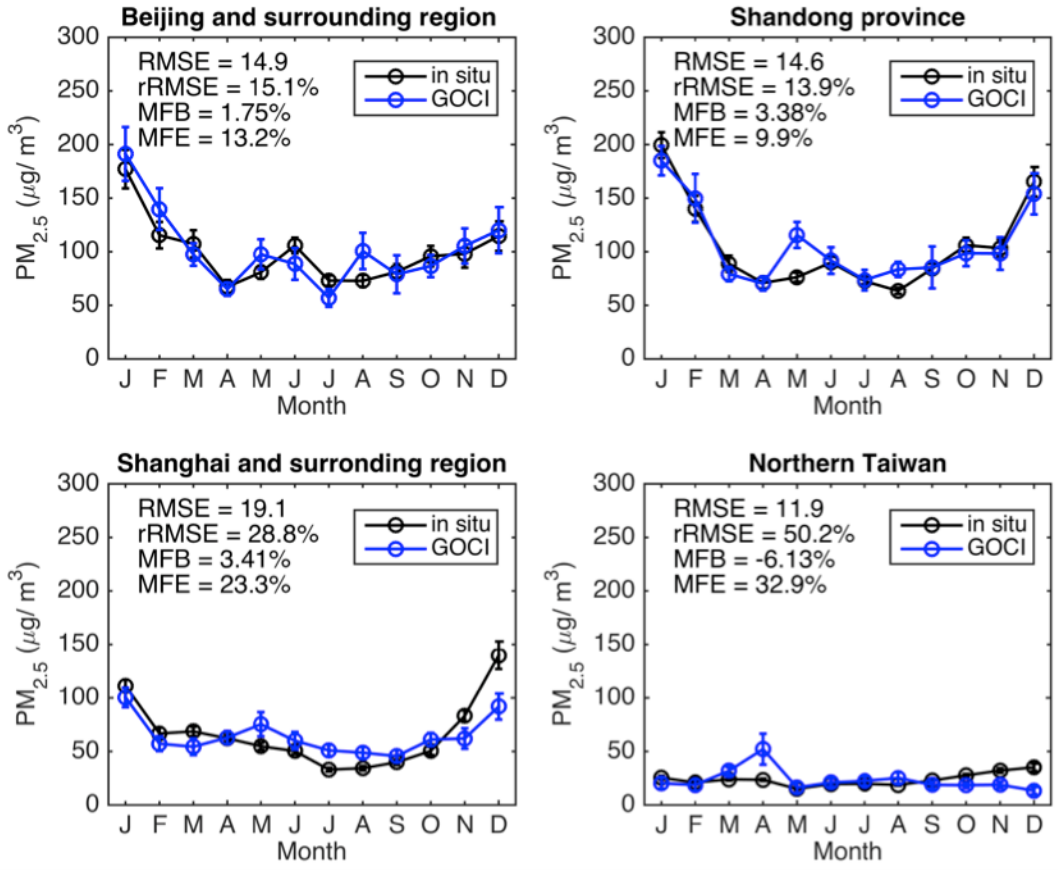

Figure 2-5: Monthly averages of daily PM2.5 from in situ measurements and daily PM2.5 estimated from GOCI AOD for 2013. Regions are defined in Fig. 2-3. Error bars represent standard errors. Statistics are root mean square error (RMSE), relative root mean square error (rRMSE), mean fractional bias (MFB) and mean fractional error (MFE).

2.8 Seasonal variation of $PM_{2.5}$

Figure 2-6 shows the monthly averages of coincident daily GOCI-derived and *in-situ* $PM_{2.5}$ concentrations for the domain of eastern China. Both the GOCI-derived $PM_{2.5}$ and ground-based observations exhibit similar seasonal variation with values high in winter and low in summer. Exclusion of our temporal and spatial cloud-screening filters from GOCI-derived $PM_{2.5}$ would increase rRMSE by a factor of 3.4. Fig. 2-6 also shows the chemical composition of GOCI-derived $PM_{2.5}$, as calculated by applying the GEOS-Chem simulated mass fraction of $PM_{2.5}$ chemical components to GOCI-derived $PM_{2.5}$ mass concentration. Aerosol water is attached to each component according to its hygroscopicity. Secondary inorganic aerosols (SIA; SO_4^{2-}, NO_3^-, NH_4^+) are the most abundant components throughout the year, accounting for 65% of $PM_{2.5}$ concentrations, followed by OM (18%). The NO_3^- and OM concentrations increase by a factor of 2 in winter, together comprising most of $PM_{2.5}$ (31% for NO_3^- and 26% for OM). Summer is predominately controlled by SIA (74%). Dust plays an important role in spring (15%) and fall (15%). Our seasonal variation of chemical composition is generally consistent with ground-based measurements in previous works across eastern China. A number of studies in Beijing, the Yangtze River delta and Pearl River delta regions all reported that OM and SIA are the most important components of $PM_{2.5}$ through the year (He et al., 2001; Ye et al., 2003; Tao et al., 2012; Zhang et al., 2013). Zhang et al. (2008) showed consistent seasonal patterns in OM at 18 stations in China, with a winter maximum, and a summer minimum, similar to the seasonality of OM in this work. Zhang et al. (2013) studied the chemical composition of $PM_{2.5}$ in Beijing and found the percentage of SIA in $PM_{2.5}$ is largest in summer, consistent with our result.

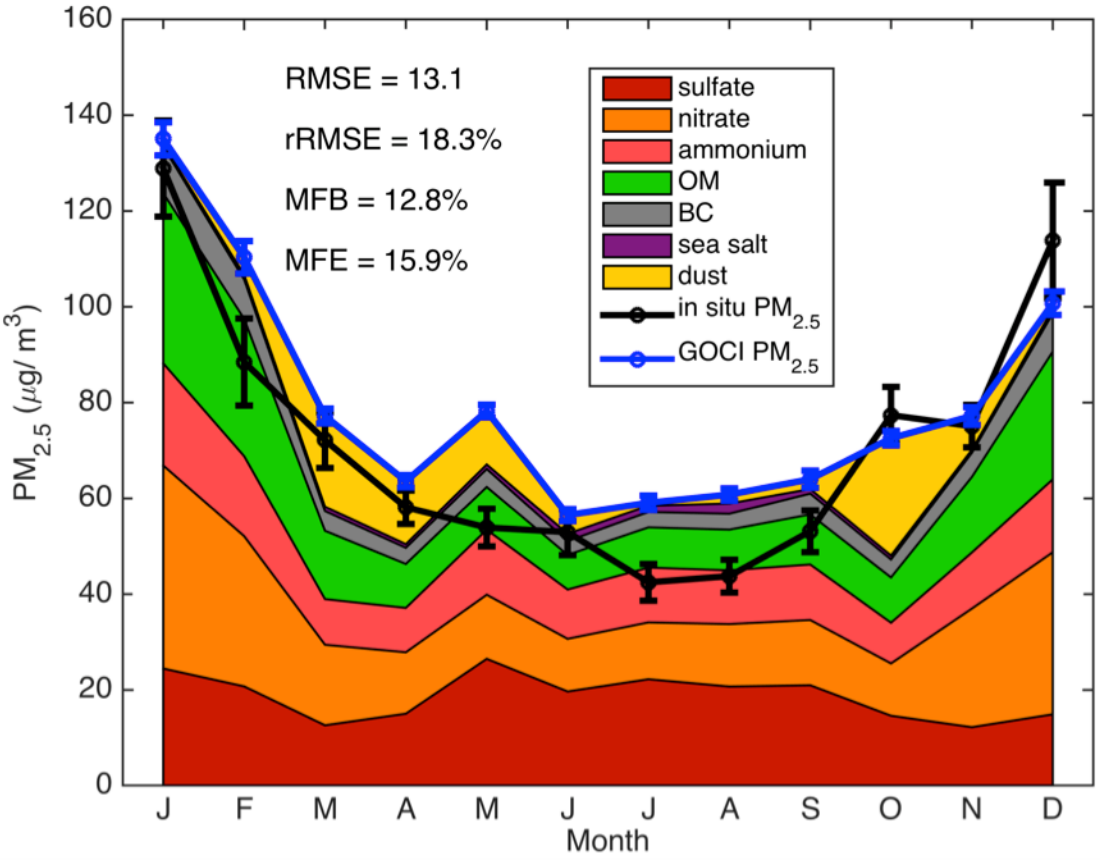

Figure 2-6: Monthly variation of GOCI-derived PM2.5 and in situ PM2.5 for 2013 over eastern China, with chemical composition for GOCI-derived PM2.5. The in situ PM2.5 is determined from the averages of all ground stations in eastern China for 2013 and GOCI-derived PM2.5 is calculated from the average of all grid boxes that contain PM2.5 ground monitors. The chemical composition is calculated by applying the GEOS-Chem simulated mass fraction of PM2.5 chemical components to GOCI-derived PM2.5 mass concentration. Aerosol water is associated with each PM2.5 component according to its hygroscopicity. Error bars represent standard errors.

The seasonal variation of $PM_{2.5}$ in Fig.2- 6 is driven by a combination of meteorological conditions, emissions, and nitrate formation. All three processes have greater seasonal variation in the north than south. The mixing height over northeastern China has strong seasonal variation with summer having an average mixing height from GEOS-5 that is 1.9 times higher than in winter. The GEOS-Chem simulation reveals that the increase of OM in winter is primarily driven by biofuel emissions from burning wood, animal waste and agricultural waste (Bond et al., 2004) for heating in eastern China. The spatial distribution of biofuel emission is primarily north of the Yangze River, especially from the North China Plain. The significant contribution from biofuel emissions to the OM concentration in our work is consistent with Bond et al. (2004) who found residential biofuel emissions were responsible for ~70% of OC emissions in China. The increase of NO_3^- in winter in

Fig. 2-6 is consistent with prior attribution of the increase of NO_3^- in winter to the favorable formation of NH_4NO_3 at low temperatures (Wang et al., 2013).

Table 2-1 shows the annual chemical composition of GOCI-derived $PM_{2.5}$ in regions outlined in Fig. 2-3 and in overall eastern China. SIA and OM are the most abundant species. Among the SIA components, SO_4^{2-} and NO_3^- concentrations are similar in the Beijing, Shandong and Shanghai regions, whereas in eastern China and northern Taiwan SO_4^{2-} is the dominant component. OM concentrations in the Beijing and Shandong regions are considerably higher than in the other regions, similar to or even exceeding the concentrations of SO_4^{2-} and NO_3^-. Our estimation of $PM_{2.5}$ composition is generally consistent with *in-situ* measurements in prior studies. In Beijing, the concentrations of SIA in this work are similar to Zhang et al. (2013) who measured concentrations for 2009-2010 of 13.6 ± 12.4 μg m^{-3} for SO_4^{2-}, 11.3 ± 10.8 μg m^{-3} for NO_3^- and 6.9 ± 7.1 μg m^{-3} for NH_4^+. Our SIA concentrations in Beijing are also comparable with Yang et al. (2011) who measured concentrations for 2005-2006 of 15.8 ± 10.3 μg m^{-3} for SO_4^{2-}, 10.1 ± 6.09 μg m^{-3} for NO_3^- and 7.3 ± 4.2 μg m^{-3} for NH_4^+. The OC concentration in Beijing in this work is smaller than Zhang et al. (2013) of 16.9 ± 10.0 μg m^{-3} and Yang et al. (2011) of 24.5 ± 12.0 μg m^{-3}. In Shandong and surrounding regions, our concentrations are smaller than in Cheng et al. (2011) by a factor of about 2, perhaps related to unresolved sources. Our results in Shanghai cluster are comparable with Yang et al. (2011) for 1999-2000, except the OC concentration in this work is considerably lower than Yang et al. (2011) of 16.8 μg m^{-3}. In northern Taiwan, our NO_3^- is similar to Fang et al. (2002) for 2001-2003, yet our estimations of SO_4^{2-} and NH_4^+ are higher than Fang et al. (2002) by a factor of two, which could be driven by changes in emissions over the last decade. In summary, the chemical composition broadly represents *in-situ* measurements with some location-dependent discrepancies.

Table 2-1: Annual $PM_{2.5}$ concentrations, area-weighted concentrations of chemical composition and affected population of $PM_{2.5}$ in regions outlined in Fig. 2-3 and in overall eastern China (excluding northern Taiwan) for 2013. Aerosol water is not associated with each $PM_{2.5}$ component for consistency with measurement protocols. $PM_{2.5}$ concentration is at 35% relative humidity. IT1 refers to the WHO air quality interim target-1 of 35 μg m^{-3}.

Region	Beijing	Shandong	Shanghai	Taiwan	Eastern China
Population-weighted GOCI-derived $PM_{2.5}$ ($\mu g\ m^{-3}$)	90.8	89.1	56.9	18.9	53.8
Area-weighted GOCI-derived $PM_{2.5}$ ($\mu g\ m^{-3}$)	86.5	89.1	51.0	23.6	44.3
SO_4^{2-} ($\mu g\ m^{-3}$)	12.8	14.0	9.2	5.1	13.1
NO_3^- ($\mu g\ m^{-3}$)	14.5	16.1	8.5	2.1	4.2
NH_4^+ ($\mu g\ m^{-3}$)	8.9	9.8	5.7	2.2	3.3
OC ($\mu g\ m^{-3}$)	10.3	9.6	4.3	1.6	2.9
BC ($\mu g\ m^{-3}$)	6.3	5.2	2.6	0.8	1.6
Dust ($\mu g\ m^{-3}$)	9.1	8.3	4.9	2.9	4.4
Sea Salt ($\mu g\ m^{-3}$)	0.2	0.4	0.9	2.2	1.9
OM ($\mu g\ m^{-3}$)	17.1	15.7	7.4	3.0	5.4
Population (million people) exposed to $PM_{2.5}$ exceeding IT-1 level	37.8	91.8	109.0	15.8	603.3

2.9 Population exposure to ambient $PM_{2.5}$ in eastern China

We estimate the population exposure to ambient $PM_{2.5}$ in eastern China for 2013 at a spatial resolution of 6 km by 6 km using our GOCI-derived $PM_{2.5}$ and the Gridded Population of the World (GPW; Tobler et al., 1997) data for 2010 from the Socioeconomic Data and Applications Center (GPW version 3; http://sedac.ciesin.columbia.edu/). Table 2-1 also provides the population-weighted GOCI-derived $PM_{2.5}$ for regions outlined in Fig. 2-3 and for overall eastern China. The population-weighted $PM_{2.5}$ exceeds the area-weighted for all regions except northern Taiwan and Shandong and surrounding regions. The overall population-weighted $PM_{2.5}$ concentration for eastern China for 2013 is 53.8 $\mu g\ m^{-3}$. The level of $PM_{2.5}$ for Beijing and Shandong regions in this study is similar to Ma et al. (2014) who suggested that the $PM_{2.5}$ concentration over the North China Plain for 2013 is 85 - 95 $\mu g\ m^{-3}$. The $PM_{2.5}$ concentration in eastern China in this study is also comparable with previous works. Van Donkelaar et al. (2015) estimated the $PM_{2.5}$ concentration over eastern Asia for 2001-2010 is $50.3 \pm 24.3\ \mu g\ m^{-3}$. Geng et al. (2015) estimated the $PM_{2.5}$ concentration in China for 2006-2012 is 71 $\mu g\ m^{-3}$, higher than our work. According to the World Health Organization (WHO) Air Quality Interim Target-1, an

annual mean $PM_{2.5}$ concentration of 35 μg m^{-3} or higher is associated with about 15% increased risk of premature mortality. As shown in Table 2-1, population-weighted $PM_{2.5}$ for eastern China considerably exceeds the Interim Target-1 level of $PM_{2.5}$ concentration, especially in Beijing and Shandong regions where the $PM_{2.5}$ concentration is almost triple the Interim Target-1 level. These elevated concentrations threaten the health of 433 million inhabitants (Table 2-1) in eastern China who live in regions that exceed this target.

2.10 Conclusions

We estimated the ground-level concentration of $PM_{2.5}$ in eastern China for 2013 using AOD retrieved from the GOCI satellite instrument, coupled with the relationship of AOD to $PM_{2.5}$ simulated by a global chemical transport model (GEOS-Chem). GOCI-derived $PM_{2.5}$ was compared with *in-situ* measurements throughout eastern China.

We applied a set of filters to GOCI AOD to remove cloud contamination. The filtered GOCI AOD showed significant agreement with AERONET AOD at Beijing and northern Taiwan (MFB of 6.7% to -1.2%). We also evaluated the simulated relationship of $PM_{2.5}$ and AOD from GEOS-Chem by using an empirical relationship calculated from nearly collocated ground-based $PM_{2.5}$ monitors and AERONET AOD stations. A high degree of consistency was observed between the GEOS-Chem simulation and ground-based measurements with MFB of -0.52% to 8.0%.

The GOCI-derived $PM_{2.5}$ were highly consistent with *in-situ* measurements, capturing the similar seasonal and spatial distribution throughout eastern China. The highest $PM_{2.5}$ concentrations were found in winter over northern regions. The annual averages of GOCI-derived $PM_{2.5}$ were strongly correlated (r^2=0.66) with surface measurements with a slope near unity (1.01). Monthly comparison of GOCI-derived $PM_{2.5}$ with ground-based measurements across the entire region of eastern China was also in good agreement with rRMSE =18.9%. The exclusion of our cloud-screening filters in GOCI retrievals would introduce significant bias in GOCI-derived $PM_{2.5}$, especially in summer and would increase the rRMSE by a factor of 1.7 - 5.3.

The chemical composition of GOCI-derived $PM_{2.5}$ revealed that secondary inorganic aerosols (SIA; SO_4^{2-}, NO_3^-, NH_4^+) and organic matter (OM) dominated throughout the year. NO_3^- had a winter maximum due to aerosol thermodynamics. OM increased by a factor of 2 in winter, which was

primarily driven by biofuel emission for heating in northern China. Dust played an important role in spring and fall.

The population-weighted GOCI-derived $PM_{2.5}$ for 2013 at 6 km by 6 km resolution in eastern China was 53.8 μg m^{-3}, suggesting ~400 million people in China live in regions with $PM_{2.5}$ concentrations exceeding the suggested 35 μg m^{-3} by the World Health Organization (WHO) Air Quality Interim Target-1, of which ~130 million people in Beijing and Shandong regions are seriously threatened by even higher $PM_{2.5}$ concentrations. Population-weighted $PM_{2.5}$ of pixels containing ground-based monitors is much higher at 82.4 μg m^{-3}, suggesting the value of the newly established $PM_{2.5}$ network to monitor these seriously polluted regions.

The satellite measurements of AOD from the GOCI instrument coupled with the relationship between AOD and $PM_{2.5}$ simulated by a chemical transport model have the potential to provide a unique synopsis of ground-level $PM_{2.5}$ concentrations at fine spatial resolution in the most polluted and populated part of China. Further development of this capability will depend on both the quality of GOCI aerosol products and the aerosol simulation. Assimilating satellite observations of trace gases from the forthcoming GEMS (Geostationary Environment Spectrometer) geostationary platform would provide additional constraints on $PM_{2.5}$ composition.

2.11 Acknowledgements

We are grateful to the GOCI, AERONET, CEMC, TEPA and SPARTAN for providing available data used in this study. Funding for this work was provided by NSERC (Natural Sciences and Engineering Research Council of Canada) and by an Izaak Walton Killiam Memorial Scholarship for J.-W. Xu. Computational facilities are partially provided by ACEnet, the regional high performance computing consortium for universities in Atlantic Canada.

Chapter 3: Source Attribution of Arctic Black Carbon Constrained by Aircraft and Surface Measurements

Authors: Jun-Wei Xu[1], Randall V. Martin[1,2], Andrew Morrow[1], Sangeeta Sharma[3], Lin Huang [3], W. Richard Leaitch[3], Julia Burkart[4], Hannes Schulz[5], Marco Zanatta[5], Megan D. Willis[4], Daven K. Henze[6], Colin J. Lee[1], Andreas B. Herber[5], Jonathan P.D. Abbatt[4]

[1]Department of Physics and Atmospheric Science, Dalhousie University, Halifax, NS, Canada

[2]Harvard-Smithsonian Center for Astrophysics, Cambridge, MA, USA

[3]Atmospheric Science and Technology Directorate/Science and Technology Branch, Environment and Climate Change Canada, Toronto, Ontario, Canada

[4]Department of Chemistry, University of Toronto, Toronto, Canada

[5]Alfred Wegener Institute, Helmholtz Centre for Polar and Marine Research, Bremerhaven, Germany

[6]Department of Mechanical Engineering, University of Colorado, Boulder, CO, USA

Article published in Atmospheric Physics and Chemistry, 17, 11971-11989, 2017. All text, figures and results were contributed by the first author.

3.1 Abstract

Black carbon (BC) contributes to Arctic warming, yet sources of Arctic BC and their geographic contributions remain uncertain. We interpret a series of recent airborne (NETCARE 2015, PAMARCMiP 2009 and 2011 campaigns) and ground-based measurements (at Alert, Barrow and Ny-Ålesund) from multiple methods (thermal, laser incandescence and light absorption) with the GEOS-Chem global chemical transport model and its adjoint to attribute the sources of Arctic BC. This is the first comparison with a chemical transport model of refractory BC (rBC) measurements at Alert. The springtime airborne measurements performed by the NETCARE campaign in 2015 and the PAMARCMiP campaigns in 2009 and 2011 offer BC vertical profiles extending to above 6 km across the Arctic and include profiles above Arctic ground monitoring stations. Our simulations with the addition of seasonally varying domestic heating and of gas flaring emissions are consistent with ground-based measurements of BC concentrations at Alert and Barrow in winter and spring (rRMSE < 13 %), and with airborne measurements of the BC

vertical profile across the Arctic (rRMSE=17 %) except for an underestimation in the middle troposphere (500-700 hPa).

Sensitivity simulations suggest that anthropogenic emissions in eastern and southern Asia have the largest effect on the Arctic BC column burden both in spring (56 %) and annually (37 %), with the largest contribution in the middle troposphere (400-700 hPa). Anthropogenic emissions from northern Asia contribute considerable BC (27 % in spring and 43 % annually) to the lower troposphere (below 900 hPa). Biomass burning contributes 20 % to the Arctic BC column annually.

At the Arctic surface, anthropogenic emissions from northern Asia (40 % - 45 %) and eastern and southern Asia (20 % - 40 %) are the largest BC contributors in winter and spring, followed by Europe (16 % - 36 %). Biomass burning from North America is the most important contributor to all stations in summer, especially at Barrow.

Our adjoint simulations indicate pronounced spatial heterogeneity in the contribution of emissions to the Arctic BC column concentrations, with noteworthy contributions from emissions in eastern China (15 %) and western Siberia (6.5 %). Although uncertain, gas flaring emissions from oilfields in western Siberia could have a striking impact (13 %) on Arctic BC loadings in January, comparable to the total influence of continental Europe and North America (6.5 % each in January). Emissions from as far as the Indo-Gangetic Plain could have a substantial influence (6.3 % annually) on Arctic BC as well.

3.2 Introduction

The Arctic has warmed rapidly over the last few decades at a rate about twice the global mean (AMAP, 2011; AMAP, 2015). By directly absorbing solar radiation, black carbon (BC) contributes substantially to the warming, impacting the Arctic in multiple ways (Flanner et al., 2007; Ramanathan and Carmichael, 2008; Shindell and Faluvegi, 2009; Bond et al., 2013; Sand et al., 2016). Near-surface (< 1 km) BC particles over a highly reflective surface (i.e. snow and ice in the Arctic) warm the atmosphere, and subsequently the surface (Shaw and Stamnes, 1980;

Quinn et al., 2008). BC particles well above the surface warm the layer in which they reside and increase the stability of the Arctic atmosphere (e.g. Brock et al., 2011). Deposition of BC onto snow and ice can reduce surface albedo and enhance light absorption by snow and ice (Wiscombe and Warren, 1980; Chýlek et al., 1983), and trigger chain reactions involving the acceleration of snow aging (Clarke and Noone, 1985; Hansen and Nazarenko, 2004), leading to accelerated melting (Quinn et al., 2008; Namazi et al., 2015). The modified local radiative balance exerted by deposited BC has the potential to further affect climate at a larger scale (Flanner et al., 2007; Doherty et al., 2010).

Analyses of observations have revealed that Arctic BC is primarily transported from regions outside the Arctic (Klonecki et al., 2003; Stohl, 2006). In winter, northern Eurasia is the primary source where air masses are cold enough to penetrate the polar dome into the Arctic lower troposphere (Stohl, 2006). Air masses from the relatively warm mid-latitudes (i.e. North America and Asia) are forced to ascend above the polar dome to the Arctic middle and upper troposphere (Law and Stohl, 2007). In spring, the warming of the surface leads to higher potential temperature over the Arctic and the northward retreat of the polar dome, facilitating the transport of air masses from mid-latitude regions to the Arctic (Stohl, 2006). However, large uncertainties remain in sources and geographical contributions to Arctic BC that require additional interpretation of observations to address.

Elevated BC concentrations in the Arctic especially in winter and spring have been observed over the past few decades (Delene & Ogren, 2002; Sharma, et al., 2006; Eleftheriadis et al., 2009; Yttri et al., 2014). Some studies attributed the surface BC primarily to emissions in high-latitude regions including Europe and northern Eurasia (e.g. Stohl, 2006; Shindel et al., 2008; Hirdman et al., 2010; Wang et al., 2014a) while others found eastern and southern Asia had the largest contribution (Koch and Hansen, 2005; Ikeda et al., 2017). Some studies suggested that Europe was the dominant source of BC aloft (Stohl, 2006; Huang et al, 2010b) while others found eastern and southern Asia was the most important source (Sharma et al., 2013; Breider et al., 2014; Wang et al., 2014a; Ikeda et al., 2017) in the middle troposphere. Recent work by Stohl et al. (2013) and Sand et al. (2016) raised questions about prior studies by identifying the importance of seasonally varying residential heating and by suggesting a significant overlooked

source from gas flaring in high-latitude regions. In addition to anthropogenic emissions, biomass burning is another important source of Arctic BC (Stohl et al., 2007; Warneke et al., 2009; Yttri et al., 2014; Evangeliou et al., 2016), yet its contribution remai20ns uncertain. Furthermore, evidence is emerging that the BC observations to which many prior modeling studies compared may have been biased by 30 % (Sinha et al., accepted) or a factor of 2 (Sharma et al., 2017) due to other absorbing components in the atmospheric aerosol. Additional attention is needed to these issues.

BC emissions in mid- and low-latitude regions increase the Arctic climate forcing efficiency by altering the BC vertical distribution (Breider et al., 2017). Thus it is also crucial to quantify the source contributions to the vertical distribution of Arctic BC. However, vertical profiles in the Arctic have been scarce (Jacob et al., 2010; Brock et al., 2011) and anomalously influenced by biomass burning (Warneke et al., 2009). The NETCARE (Network on Climate and Aerosols: Addressing Key Uncertainties in Remote Canadian Environments, http://www.netcare-project.ca) aircraft campaign in 2015 and the PAMARCMiP (Polar Airborne Measurements and Arctic Regional Climate Model Simulation Project) aircraft campaigns in 2009 and 2011 offer a new dataset of BC measurements across the Arctic.

Source attributions of pollution in the Arctic are commonly estimated by back-trajectory analysis (Huang et al., 2010a; Harrigan et al., 2011; Barrett et al., 2015; Liu et al., 2015), and by sensitivity simulations using chemical transport models (Fisher et al., 2010; Sharma et al., 2013; Mungall et al., 2015; Evangeliou et al., 2016). These traditional approaches have been insightful, but suffer from coarse regional estimates of the source location. The adjoint of a global chemical transport model (Henze et al., 2007) efficiently determines the spatially resolved source contribution to receptor locations by calculating the gradient of a cost function (e.g. Arctic column BC concentrations) with respect to the perturbations of the initial conditions (e.g. emissions). This approach has been successfully applied to quantify source contributions to Arctic surface BC in April 2008 (Qi et al., 2017b). We extend the application of this method to investigate the seasonal and annual responses of Arctic column BC to changes in regional emissions.

In this study, we first evaluate the BC concentrations simulated with the GEOS-Chem global chemical transport model with surface and aircraft measurements in the Arctic to assess the quality of different emission representations. Then sensitivity simulations are conducted to assess the regional contributions to the observed BC in the Arctic. We subsequently use the adjoint of the GEOS-Chem model to investigate the spatially resolved sensitivity of Arctic BC column concentrations to global emissions. Our work builds on knowledge gained from previous GEOS-Chem studies of Arctic BC (Wang et al., 2011; Breider et al., 2014; Breider et al., 2017; Qi et al., 2017a; Qi et al., 2017b) with major improvements including 1) new airborne measurements during 2009, 2011 and 2015 when more typical fires than in previous studies foster better understanding of anthropogenic source contributions to the Arctic; 2) new refractory BC measurements in the Arctic more accurately constrain emissions in simulations; 3) more recent and improved emissions better represent the global redistribution of BC emissions, include flaring and seasonal emissions of residential heating; and 4) seasonal source attribution using the adjoint of GEOS-Chem reveals the importance of specific sources.

3.3 Method

3.3.1 Surface measurements of BC in the Arctic

Surface BC mass concentrations are measured at three Arctic stations: Alert (Nunavut, Canada; 62.3° W, 82.5° N), Barrow (Alaska, USA; 156.6° W, 71.3° N) and Ny-Ålesund (Svalbard, Norway; 11.9° E, 78.9° N). Station locations are shown in Fig. 3-1. Following the recommendations of Petzold et al. (2013), measurements of BC based on light absorption are here referred to as equivalent BC (EBC); measurements based on a laser induced incandescence technique (e.g. single particle soot photometer; SP2) are referred to as refractory BC (rBC); and measurements based on a thermal volatilization in an oxygen-enriched environment are referred to as elemental carbon (EC).

EBC mass concentrations derived from an AE-31 Aethalometer (Magee Scientific Inc.) at Alert for 2011-2013 are obtained from Environment and Climate Change Canada and those at Barrow for 2010-2014 and Ny-Ålesund for 2009-2010 are obtained from the EMEP (European Monitoring and Evaluation Programme) and WDCA (World Data Centre for Aerosols) database

(http://ebas.nilu.no/). The Aethalometer measures the absorption of light at 880 nm transmitted through particles that accumulate on a quartz fiber filter and relates the change of light absorption to light absorption coefficients (σ_{ap}) using Beer's Law. EBC mass concentrations are derived from σ_{ap} by adopting a mass absorption cross-section (MAC) of 16.6 $m^2 g^{-1}$ at all stations. This MAC value is recommended by the manufacturer for Model AE31 at 880 nm to account for absorption by BC and additional light scattering by both particles and filter fibers.

EBC mass concentrations are also derived from a particle soot absorption photometer (PSAP, Radiance Inc.) that operates on a similar principle to the Aethalometer at the three stations. PSAP measures the absorption of light at 530 nm. σ_{ap} data at Alert for 2011-2013 are obtained from Environment and Climate Change Canada, and σ_{ap} data at Barrow for 2009-2015 and Ny-Ålesund for 2009-2014 are obtained from the EMEP and WDCA database (http://ebas.nilu.no/). σ_{ap} has been corrected for scattering following Bond et al. (1999) and is further reduced by 30 % at all stations following Sinha et al. (accepted). σ_{ap} values less than the detection limit (0.2 Mm^{-1}) are excluded. Recent evidence is emerging that the MAC is lower than the traditional value of 10 $m^2 g^{-1}$, with recent effective MAC values ranging from 8 $m^2 g^{-1}$ (Sharma et al., 2017) to 8.7 $m^2 g^{-1}$ (Sinha et al., accepted). We adopt the average of these two values (8.4 $m^2 g^{-1}$) for application to PSAP measurements at all three sites.

Two additional measurements of BC mass concentrations are available at Alert for 2011-2013: rBC and EC. rBC is measured via laser induced incandescence by an SP2 instrument (Droplet Measurement Technologies Inc., Boulder, CO). The SP2 uses a high intensity laser (Ni:YAG) operating at 1064 nm wavelength to selectively heat individual particles up to 4000K. At such high temperature, the non-refractory components evaporate and rBC mass is proportional to the intensity of the emitted incandescent light. The incandescence signal is calibrated using Aquadag particles of known size selected with a differential mobility analyzer (Sharma et al., 2017). The detection range of the SP2 at Alert spans approximately between 75 nm and 530 nm volume-equivalent diameter (Sharma et al., 2017), assuming an rBC density of 1.8 g cm^{-3} (Bond and Bergstrom, 2006). A lognormal function fit over the range of 80-225 nm is applied to calculate rBC concentrations over the 40-1000 nm size range that increases the rBC concentrations by about 50 % (Sharma et al., 2017).

EC measurements at Alert are inferred from weekly-integrated samples of particles collected on quartz filters with a 1μm upper size cut and analyzed using an in-house thermal technique referred to as EnCan-total-900 (Huang et al., 2006). The EnCan-total-900 method has three temperature steps with different redox conditions: 550°C and 870°C under pure helium and 900°C under helium + 10 % oxygen. The retention times are 600 seconds at 550°C for organic carbon (OC), 600 seconds at 870°C for pyrolysis of OC and carbonate carbon, and 420 seconds at 900°C for EC. The 870°C pure helium step releases pyrolysis OC and carbonate carbon to minimize the effect of OC charring on EC.

3.3.2 Aircraft measurements of BC in the Arctic

Prior Arctic aircraft campaigns (i.e. ARCTAS) were strongly influenced by the unusually extensive Russian fires in 2008 (e.g. Warneke et al., 2009; Wang et al., 2011; Breider et al., 2014). This study uses new aircraft observations when fires were less pronounced over multiple years (2009, 2011 and 2015) to better understand anthropogenic source contributions. The PAMARCMiP campaigns conducted springtime surveys of sea ice thickness, aerosol and meteorological parameters along the coast of the western Arctic onboard the Alfred Wegener Institute (AWI) Polar 5 aircraft. Data from two campaigns in April 2009 (Stone et al., 2010) and March 25th – May 6th 2011 (Herber et al., 2012) are used here. The NETCARE campaign in April 2015 continued and extended the PAMARCMiP campaigns observations using the Polar 6 aircraft. Flight tracks of each campaign are shown in Fig. 3-1. All three campaigns traveled along similar routes across the western Arctic and near long-term ground monitoring stations in the Arctic (Alert, Barrow and Ny-Ålesund). Measurements of rBC mass concentrations during all three campaigns were performed with the state-of-the-art SP2 (Droplet Measurement Technologies Inc., Boulder, CO) instrument. The SP2 used during the PAMARCMiP campaigns was previously described in Stone et al. (2010). The NETCARE 2015 campaign used the AWI's 8-channel SP2 with a detection range of 75 – 700 nm of volume-equivalent diameter (assuming a particle density of 1.8 g cm^{-3}) without corrections for particles outside the size range. The incandescence signal was calibrated with particles of Fullerene soot size selected with a

differential mobility analyzer. The spatial and multi-year coverage of airborne measurements during these campaigns offer comprehensive representation of Arctic BC.

3.3.3 Simulations of Arctic BC

We use the GEOS-Chem global chemical transport model (version 10-01; http://geos-chem.org/) and its adjoint (version 35) to simulate Arctic BC concentrations and their sensitivities to local emissions.

Figure 3-1 shows the annual mean BC emissions in our GEOS-Chem simulation averaged over 2009, 2011 and 2015. We develop the simulation here to use global anthropogenic emissions of BC from version 2 of the HTAP (Hemispheric Transport of Air Pollution; http://www.htap.org/) emission inventory for 2010 (Gilardoni et al., 2011; Janssens-Maenhout et al., 2015) with regional overwrites over the United States (NEI 2011) for the most recent year (2011). Global and regional BC emissions remain largely constant after 2010 (Crippa et al., 2016). The HTAP inventory is a compilation of different official emission inventories from MICS-Asia, EPA-US/Canada and TNO-Europe data, gap-filled with global emission data of EDGARv4.1. The HTAP contains BC emissions from all major sectors, including energy and industrial production, transport and residential combustion.

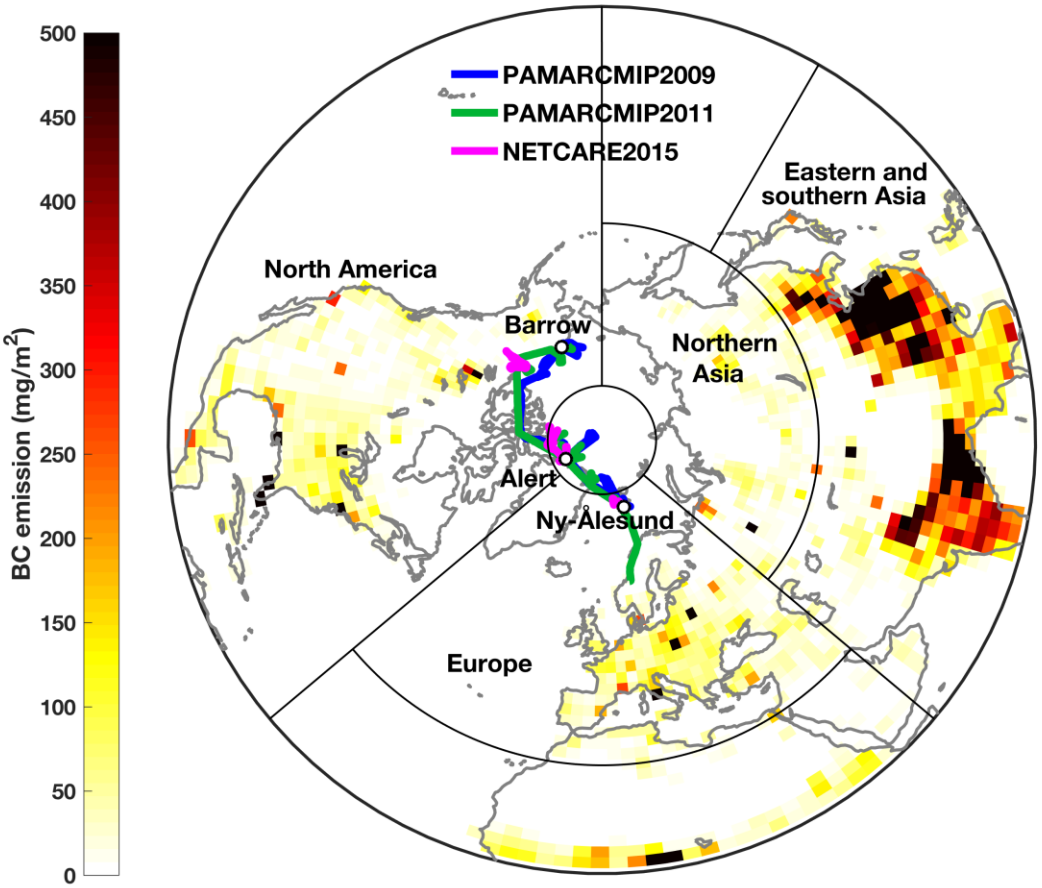

Figure 3-1: The colormap indicates annual total BC emissions averaged over 2009, 2011 and 2015 as used in the GEOS-Chem simulation. Black open circles indicate the locations of ground monitoring stations (Alert, Barrow and Ny-Ålesund). Colored lines indicate the flight tracks of the NETCARE 2015 (April 5th-21st), the PAMARCMiP 2009 (April 1st -25th) and the PAMARCMiP 2011 (Mar 30th – May 5th) campaigns. Black lines outline the source regions used in this study. Regional BC emissions are in Table 3-1.

Table 3-1 contains the annual regional BC emissions used in the simulation. Total BC emissions from eastern and southern Asia exceed by more than a factor of 4 the BC emissions from either North America or Europe.

Table 3-1. Regional annual BC emissions averaged over 2009, 2011 and 2015 as used in the GEOS-Chem simulations[a].

Emission Source ($Tg\ C\ yr^{-1}$)	North America	Europe	Northern Asia	Eastern and southern Asia
Anthropogenic[b]	0.62	0.48	0.11	3.36
Biomass burning	0.17	0.02	0.13	0.20

[a] Regions are outlined in Fig. 3-1.

[b] Including gas flaring, fossil fuel combustion and biofuel combustion.

Figure 3-2 shows annual HTAP BC emissions and its seasonal variation over the Arctic and the Northern Hemisphere. The Bond et al. (2007) emission inventory for 2000 is included for comparison, since it has been widely used in modeling studies of Arctic BC (Shindell et al., 2008; Koch et al., 2009; Liu et al., 2011; Wang et al., 2011; Breider et al., 2014; Qi et al., 2017a; Qi et al., 2017b). The Bond et al. (2007) inventory is based on energy consumption in 1996 and contains similar emission sectors as in the HTAP. The HTAP annual emissions over the Northern Hemisphere exceed those in Bond et al. (2007) by 30 %, with a substantial difference in China and India where HTAP emissions are double those of Bond et al. (2007). A considerable increase of global energy consumption since 2001 especially in China and India contributes to the difference (Zhang et al., 2009; Li et al., 2017). Both inventories have low BC emissions within the Arctic. Figure 3-2 also shows the seasonal variation of HTAP emissions that are high in winter and spring and low in summer over the Northern Hemisphere, owing to the seasonal variation of emissions from residential heating in the HTAP. Bond et al. (2007) emissions are non-seasonal.

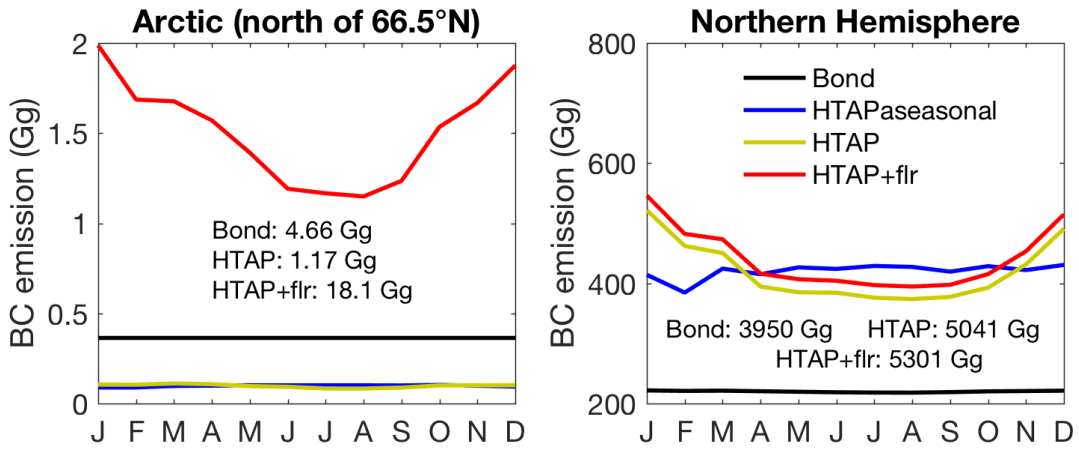

Figure 3-2: Anthropogenic BC emissions. Lines indicate monthly anthropogenic BC emissions from the Bond et al. (2007) non-seasonal inventory for 2000, the HTAP inventory for 2010, the HTAP inventory with non-seasonal emissions from residential heating, and the HTAP with additional flaring emissions for 2010. Annual values are given in the text.

We also include additional BC emissions from gas flaring in the oil and gas industry taken from version 5 of the ECLIPSE (Evaluating the climate and Air Quality Impacts of short-Lived Pollutants) emission inventory (Klimont et al., 2016; http://eclipse.nilu.no). Gas flaring emissions of BC are calculated based on gas flaring volumes developed within the Global Gas Flaring Reduction initiative (Elvidge et al., 2007, 2011) with emission factors derived on the basis of particulate matter and soot estimates from CAPP (2007), Johnson et al. (2011) and US EPA (1995). Despite the small percentage (~5 %) of flaring in total anthropogenic BC emissions over the Northern Hemisphere, flaring from Russia alone accounts for 93 % of total anthropogenic BC emissions within the Arctic in the ECLIPSE inventory.

Emissions from biomass burning are calculated from the GFED4 (Global Fire emissions Database version 4) inventory (Giglio et al., 2013). The GFED4 combines satellite information on fire activity and vegetation productivity to estimate globally gridded monthly burned area (including small fires) and fire emissions. We use emissions for 2009, 2011 and 2014 (the most recent year available) for the simulations of 2009, 2011 and 2015. The mismatch of emission year is unlikely to strongly influence the simulation as no abnormal fire activities were reported for 2014 and 2015. Biomass burning emissions are injected into the boundary layer in our simulations.

As discussed in Sect. 2.1, measurements of BC depend on the analysis method. However, it is ambiguous what analysis method is used to derive BC emission factors or BC speciation factors in particulate matter in various emission inventories (Bond et al., 2013). Therefore, we directly compare simulated BC concentrations with the best estimate of measured atmospheric BC.

The simulation of BC in GEOS-Chem is initially described in Park et al. (2003). BC emitted from all primary sources is in hydrophobic and hydrophilic states with a constant conversion time of one day. Dry deposition of BC aerosols adopts a standard resistance-in-series scheme as described in Zhang et al. (2001) with improvements on BC dry deposition velocity over snow and ice following Fisher et al. (2010) and Wang et al. (2011). Wet deposition of BC aerosols is initially described in Liu et al. (2001) and developed by Wang et al. (2011) to distinguish between liquid cloud ($T > 268$ K) in which 100 % hydrophilic BC is removed and ice cloud ($T < 268$ K) in which only hydrophobic BC is removed. The scavenging developments of Wang et al. (2014b) are not implemented since they have little effect on Arctic BC.

Our GEOS-Chem simulations are driven by Modern-Era Retrospective Analysis for Research and Applications (MERRA) meteorological fields from the Global Modeling and Assimilation Office (GMAO) at 2° × 2.5° spatial resolution with 47 vertical levels from the surface to 0.01 hPa. We conduct the simulations with a 10-minute operator duration for transport and a 20-minute operator duration for chemistry as recommended by Philip et al. (2016). The model is initialized with a 6-month spin-up before each simulation to remove the effects of initial conditions on aerosol simulations. The time period simulated is 2009, 2011 and 2015, which is coincident with aircraft measurements when fires were more typical than for previous evaluations of GEOS-Chem versus Arctic observations (i.e., Wang et al., 2011; Breider et al., 2014) to better understand anthropogenic source contributions here.

We conduct sensitivity simulations using the GEOS-Chem model to quantify the contributions of regional emissions to Arctic (hereafter refer to the region north of 66.5° N) BC concentrations by excluding the regional anthropogenic source. Regions are North America (180° W-50° W, 0° N – 80° N), Europe (50° W- 50° E, 30° N – 80° N), eastern and southern Asia (50° E – 150° E, 0° N – 50° N) and northern Asia (50° E – 180° E, 50° N – 80° N), as outlined in Fig.3-1. We also

conduct sensitivity simulations to quantify the contribution of biomass burning from North America and from the rest of the world to Arctic BC concentrations. These simulations are initialized with a 6-month spin-up as well.

We also apply the GEOS-Chem adjoint model to quantify the spatially resolved sensitivity of Arctic BC column concentrations to local emissions. A detailed description of the adjoint model is given in Henze et al. (2007). Here we briefly describe the concept in the context of our study. The adjoint model offers a computationally efficient approach to calculate the sensitivity of a model output scalar, the cost function, to a set of model input parameters such as emissions. In this study, we define the cost function as the column concentrations of BC north of 66.5° N. The adjoint model calculates the partial derivatives of this cost function with respect to the modeled atmospheric state in each model grid box at each time step. This calculation is performed iteratively backward in time through transport toward emissions to yield the sensitivity of the cost function with respect to emissions.

Our adjoint simulation is driven by GEOS-5 meteorology at 2° × 2.5° spatial resolution with 47 vertical levels from the surface to 0.01 hPa for 2011. Differences between MERRA meteorological fields that are used in the forward model and GEOS-5 meteorological fields that are used in the adjoint are negligible (r^2 = 0.99 for Arctic column BC concentrations for 2011) in the simulation of BC. Although the adjoint simulation is based on an earlier version (v8) of the GEOS-Chem model than the forward model version (v10-01) used in this study, the differences in BC concentrations at Arctic stations that are simulated with the adjoint and with the forward model are within 15 % (Qi et al., 2017b).

3.3.4 Statistics

To assist with the evaluation of simulations, we define root mean square error (RMSE) and relative root mean square error (rRMSE) as

$$\text{RMSE}=\sqrt{\frac{1}{N}\sum_{i=1}^{N}(C_m(i)-C_o(i))^2} \quad (1)$$

$$\text{rRMSE}=100\ \%\times\frac{\text{RMSE}}{\frac{1}{\text{N}}\sum_{\text{i=1}}^{\text{N}}C_m(i)} \quad (2)$$

where $C_m(i)$ is the model simulated concentration and $C_o(i)$ is the measurement concentration. N is the number of measurements.

3.4 Results

3.4.1 Evaluation of GEOS-Chem simulated BC concentrations in the Arctic

Figure 3-3 shows the seasonal variation of BC concentrations from measurements and simulations at the Alert, Barrow and Ny-Ålesund stations. Different black line types indicate different instruments. Slight differences exist in sampling periods from different instruments. Restricting measurements to common years changes monthly means by less than 13 %, except for a 40 % change at Ny-Ålesund in April that arises from limited data coverage in common years since PSAP measurements for April are not available at Ny-Ålesund in 2009. At Alert, a diversity of instruments offers valuable insight into the suite of BC measurements throughout the Arctic, and perspective on previous model comparison with only one instrument type. EBC concentrations measured by the Aethalometer are biased high by a factor of 2 relative to rBC measurements, due to the presence of absorbing substances other than BC (e.g. brown carbon and mineral dust), extinction issues associated with the filter matrix and uncertainties in MAC values (Sharma et al., 2017). EC concentrations are lower than EBC concentrations from the Aethalometer, yet still high relative to rBC partly due to the presence of pyrolysis OC and carbonate carbon (Sharma et al., 2017). PSAP EBC concentrations are close to the average of EC and rBC concentrations throughout the year. At Barrow, EBC concentrations from the Aethalometer are higher than those from the PSAP, especially in summer when the Aethalometer shows a pronounced increase in concentrations to around 55 ng m^{-3}, whereas PSAP measurements reach a minimum for the year of 10 ng m^{-3}. The summer peak is also observed in Aethalometer EBC measurements at 370 nm that is sensitive to brown carbon, indicating the influence of biomass burning. Unintentional exclusion of biomass burning plumes in the local pollution data screening performed for PSAP measurements at Barrow could contribute to the bias between the PSAP and the Aethalometer there (Stohl et al., 2006).

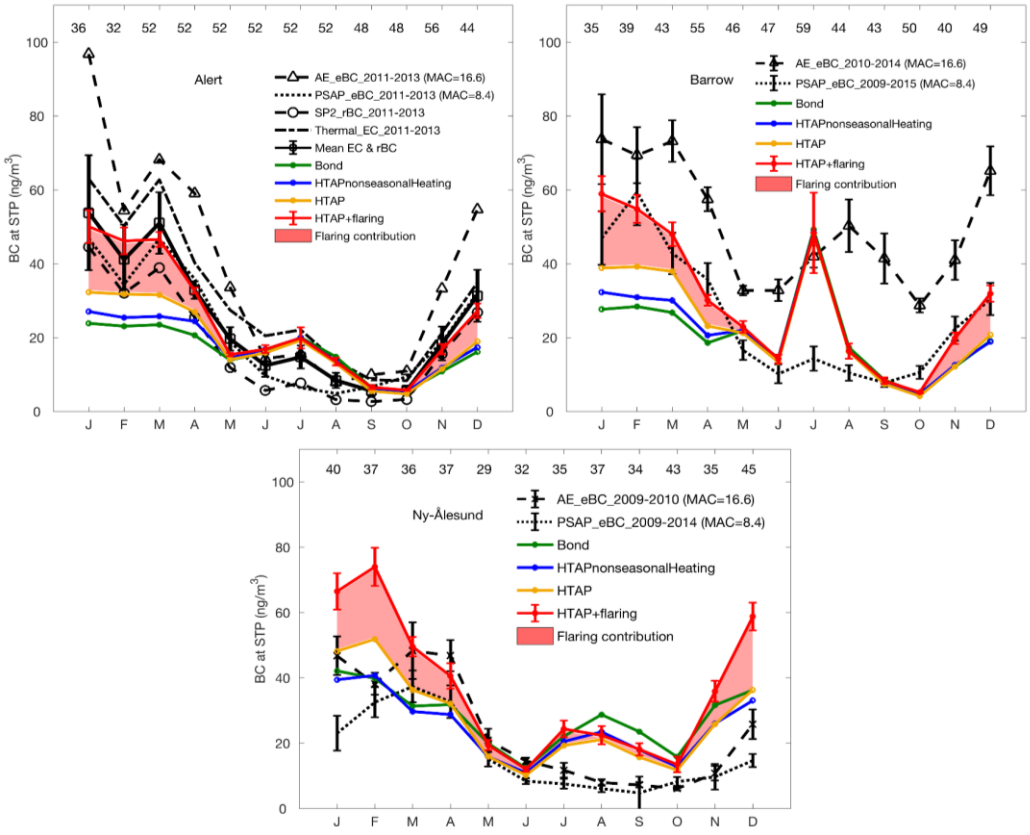

Figure 3-3: Seasonal variation of surface BC concentrations from measurements and simulations at selected Arctic stations. Black lines represent measurements from different instruments according to the legend. Error bars represent standard errors. The thick black line with squares at Alert is the average of rBC and EC concentrations. Error bars on the thick black line denote standard errors of monthly mean BC concentrations across instruments that are included in the calculation. Red shadings are the contributions from flaring to BC concentrations. Numbers below the top x-axis denote the total number of weekly observations from all available instruments in each month. Simulated monthly BC concentrations are the monthly averages of simulated concentrations for 2009, 2011 and 2015. Simulations use different emission inventories that are represented in color according to the legend. Error bars on the simulation represent standard errors. Concentrations from measurements and simulations are all calculated at standard temperature and pressure (STP).

Following Sharma et al. (2017), we treat the best estimate of measured BC surface concentrations at Alert as the average of rBC and EC measurements, as shown by the thick black line with squares in Fig. 3-3. Since the PSAP EBC concentrations are close to the average of rBC and EC measurements throughout the year at Alert, we adopt the PSAP EBC measurements as the best estimate of surface BC at Barrow and Ny-Ålesund. The seasonal variations of surface BC at the three sites show similar features, characterized by higher concentrations in winter and early spring than in summer. At Ny-Ålesund, peak months are March and April, slightly later

than at the other sites (January and February). BC concentrations at Ny-Ålesund are generally lower than those at the other sites.

The surface BC concentrations from measurements are used to constrain emissions in the simulations. Table 3-2 summarizes the RMSE and rRMSE between measurements and different simulations. The green line in Fig. 3-3 shows simulated surface BC concentrations using anthropogenic emissions of BC from the Bond et al. (2007) non-seasonal emission inventory. Stohl et al. (2013) found that accounting for BC emissions from gas flaring and from seasonal variation of residential heating improved their simulation with a particle dispersion model (FLEXPART) during winter and early spring. Our simulation at Alert and Barrow in winter and spring is also improved by using the HTAP emissions that include seasonal variation of residential heating and by adding flaring emissions to the HTAP inventory, decreasing the bias by about a factor of 2 and reducing the rRMSE to 5.6 % at Alert and 13 % at Barrow. At Barrow all simulations show a distinct peak in July, which is partly due to the timing of biomass burning. Eckhardt et al. (2015) similarly observed enhanced concentrations in July at Barrow in three models (DEHM, CESM1-CAM5 and ECHAM6-HAM2) driven with the GFED3 inventory for biomass burning emissions. At Ny-Ålesund, all simulations overestimate measured concentrations for most of the year, potentially indicating insufficient wet deposition from riming in mixed phase clouds that occurs more frequently at this site (Qi et al., 2017a).

Table 3-2: Summary of root mean square error (RMSE) and relative root mean square error (rRMSE) between simulations with different emissions and measurements for BC surface concentrations at Arctic stations (in reference to Fig. 3-3) and for vertical concentrations from airborne measurements (in reference to Fig. 3-5).

RMSE (ng m^{-3}; rRMSE)	Alert	Barrow	Ny-Ålesund	Vertical
Bond[a]	13 (55%)	17 (66%)	15 (88%)	17 (40%)
HTAPnonseasonalheating[b]	11 (48%)	16 (61%)	12 (71%)	11 (27%)
HTAPheating[c]	8.7 (37%)	13 (52%)	14 (82%)	9.4 (23%)
HTAPheatingflaring[d]	3.7 (16%)	11 (44%)	25 (150%)	7.2 (17%)

[a] Bond et al. (2007) emission inventory for 2000.

[b] HTAP v2 inventory for 2010 with non-seasonal residential heating

[c] HTAP v2 inventory for 2010 with seasonal residential heating

[d] HTAP v2 inventory for 2010 with seasonal residential heating and the addition of flaring emissions from the ECLIPSE v5 inventory

Figure 3-4 shows vertical profiles of BC concentrations at Alert and Ny-Ålesund averaged from the NETCARE 2015, the PAMARCMiP 2009 and the PAMARCMiP 2011 campaigns, along with the best estimate of ground-based measurements of April BC concentrations averaged over 2009 and 2011. Barrow is not included here due to limited number of airborne measurements (a total of 12 measurements at all pressures). The measured profile at Alert exhibits layered structure with enhanced concentrations in the middle troposphere that are attributable to a plume on April 8th 2015 around 660-760 hPa with a peak concentration of 128 ng m^{-3}. The mean ground-based measurements of BC concentrations at Alert are higher than airborne measurements at the same pressure by ~10 ng m^{-3}. Including only rBC measurements in ground-based mean concentrations reduces the difference with airborne rBC measurements to less than 5 ng m^{-3}. At Ny-Ålesund, the measured vertical profile exhibits a zigzag shape that arises from averaging multiple years each with individual features. The mean April ground-based concentration (20 ng m^{-3}) is about half that of the airborne measurements (37 ng m^{-3}) at the same pressure.

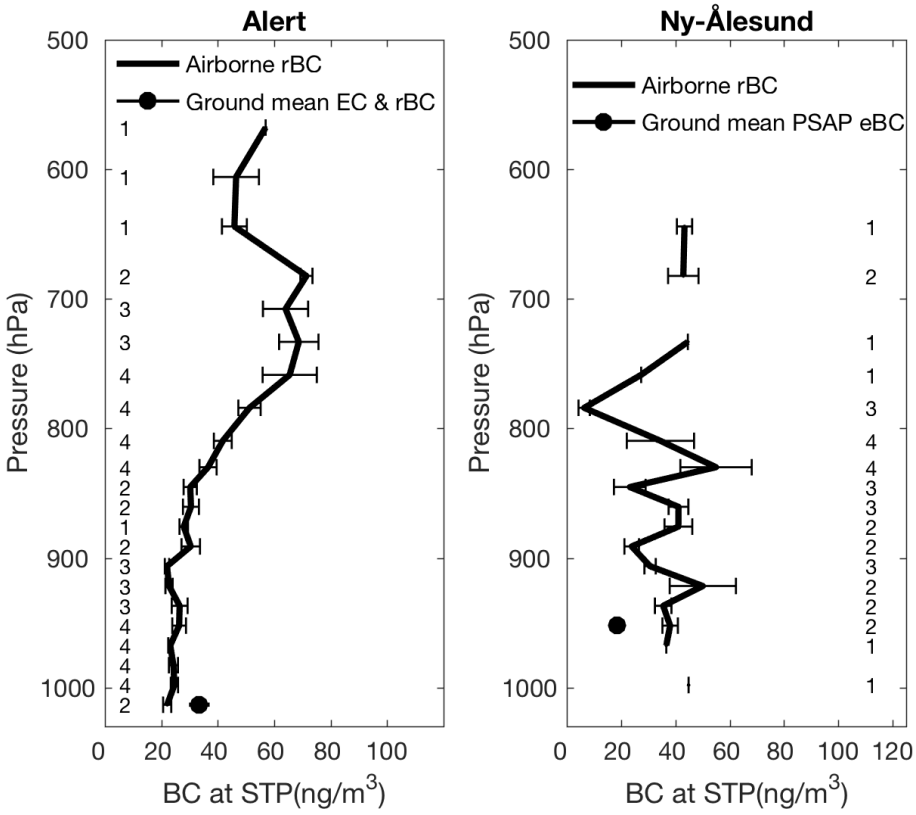

Figure 3-4: Vertical profile of BC concentrations averaged from all points along the flight tracks of the three aircraft campaigns (NETCARE 2015, the PAMARCMiP 2009 and the PAMARCMiP 2011) in Alert and Ny-Ålesund areas, along with the best estimate of April BC concentrations from ground-based measurements averaged for 2009 and 2011. The Alert area is defined as 59°W-65°W, 81.3°N-83.4°N and the Ny-Ålesund area is within 12°E-18°E, 77.8°N-79.1°N. Numbers along the y-axis are the number of airborne measurements in each pressure bin. All concentrations are presented at STP. Error bars on ground measurements are standard errors.

Figure 3-5 shows spring vertical distributions of BC averaged over all points along the flight tracks of the three campaigns in Fig. 3-1 for measurements and simulations. Simulated vertical profiles of BC are coincidently sampled with airborne measurements for spring 2009, 2011 and 2015, and are averaged to the GEOS-Chem vertical resolution. The measured rBC concentrations remain roughly constant (~38 ng m^{-3}) from the surface to 700 hPa, followed by an enhancement to around 50 ng m^{-3} between 700 hPa – 500 hPa, and then a rapid decrease with altitude. This vertical distribution is similar to the measurements of the ARCTAS aircraft campaign in the Arctic in spring 2008 (Wang et al., 2011), though the magnitude of concentrations in this work is lower by a factor of about 2, likely because the Arctic was substantially influenced by strong biomass burning in northern Eurasia during the ARCTAS in spring 2008 (Warneke et al., 2009).

All simulations generally represent the near constant vertical distribution of BC measurements from the surface to 700 hPa, and the decrease above 500 hPa, yet none represent the enhancement between 700-500 hPa. Despite the comparable distributions, the magnitudes of concentrations simulated with different emissions vary substantially. Their consistency with airborne measurements is summarized in Table 3-2.

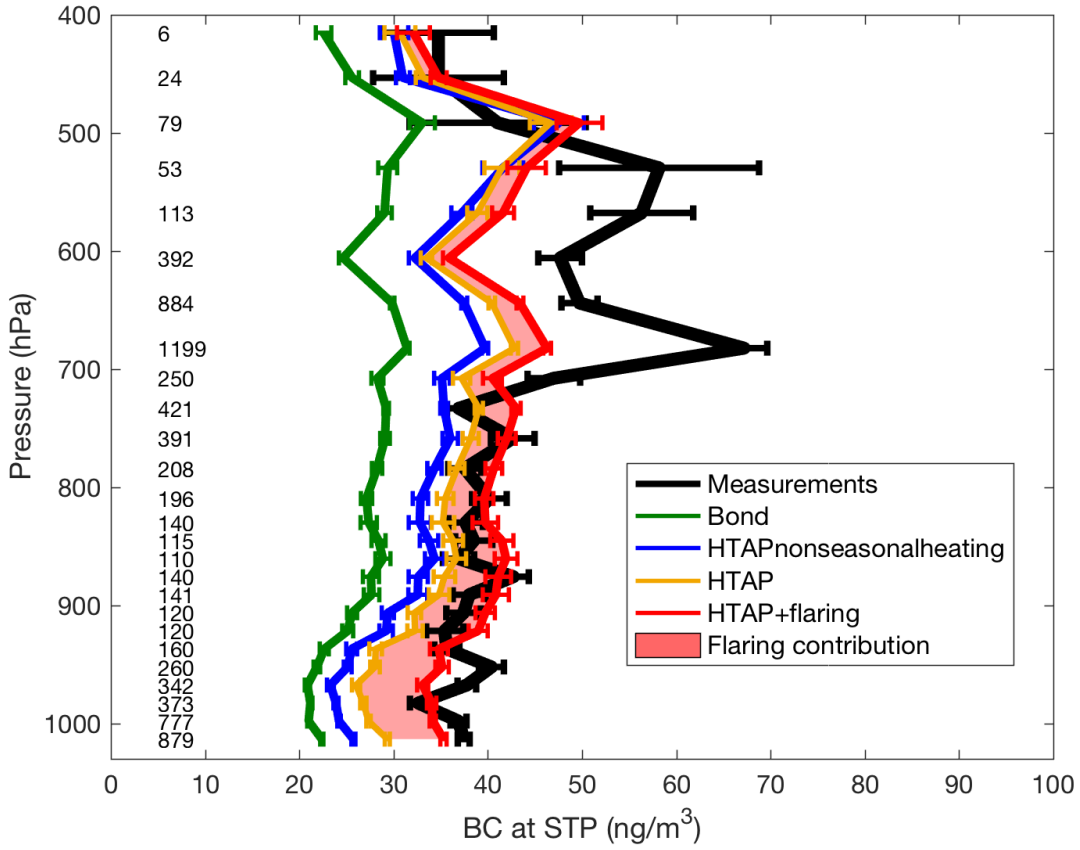

Figure 3-5: Mean spring vertical profiles of BC concentrations from measurements and simulations averaged over 50 hPa pressure bins from all points along the flight tracks of the NETCARE 2015, the PAMARCMiP 2009 and the PAMARCMiP 2011 campaigns. The red shading denotes the contribution of flaring to BC concentrations. Simulated vertical profiles of BC are coincidently sampled with airborne measurements for spring 2009, 2011 and 2015, and are averaged to the GEOS-Chem vertical resolution. Simulations include different emission inventories that are represented in different lines according to the legend. Error bars are standard errors. Numbers along the y-axis represent the number of measurements in each pressure bin. All concentrations are presented at STP.

Figure 3-5 shows that the apparent bias of 40 % rRMSE (17 ng m^{-3} RMSE) in simulated concentrations with the Bond et al. (2007) non-seasonal inventory is reduced to 27 % rRMSE (11 ng m^{-3} RMSE) by the HTAP inventory with non-seasonal residential heating. The improvement

is larger aloft than near-surface, indicating that the increased BC emissions in Asia in the HTAP inventory (discussed in Sect. 2) substantially contributes to the improvement. The bias versus measurements is further reduced to 23 % rRMSE (9.4 ng m^{-3} RMSE) by the HTAP emissions with seasonal residential heating, with larger improvement below 600 hPa. Adding flaring emissions further improves the consistency (17 % rRMSE; 7.2 ng m^{-3} RMSE) with measurements at all levels with larger effects in the lower troposphere, especially near the surface where the RMSE is only 3.2 ng m^{-3}. The substantial portion (93 %) of flaring in BC emissions within the Arctic (Fig. 3-2) explains the larger effect near the ground. The remaining underestimation of 14 ng m^{-3} RMSE in 500-700 hPa in the HTAP+flaring simulation is possibly due to insufficient emissions or preferential sampling of plumes by the aircraft as discussed further below. If the measurements are representative in this region, the Arctic BC burden below 500 hPa in springtime could be 6.5 % larger than simulated here.

Figure 3-6 (A1 and A2) shows the spatial distribution of BC concentrations from aircraft measurements gridded onto the GEOS-Chem grid along with that from the HTAP+flaring simulation. The simulation represents well the spatial distribution of BC measurements, with concentrations of 30-70 ng m^{-3} near Barrow and Ny-Ålesund and lower concentrations of 20-40 ng m^{-3} near Alert, yet the simulation underestimates concentrations at three hotspots (labeled as a, b, c). Hotspot a is near Barrow along the coast of the Beaufort Sea that is affected by a plume around 800 hPa on April 6th 2011 and a plume around 500 hPa on April 20th 2015. Hotspot b is west of the Baffin Bay in Nunavut that is affected by a plume near 800 hPa on April 10th 2011. Hotspot c is near Ny-Ålesund that is caused by a plume at around 700 hPa on May 5th 2011 . The underestimated magnitudes of these plumes, likely related to emissions or numerical diffusion, may contribute to the underestimation of BC concentrations between 500-700 hPa in Fig. 3-5. Fig. 3-6 (A3) shows mean simulated BC concentrations between 500-700 hPa in April. Concentrations are highest (~70 ng m^{-3}) in northeastern Russia and near Barrow, with a gradual decrease eastward to around 50 ng m^{-3} near Alert to reach the lowest concentrations of below 40 ng m^{-3} in the southern Arctic near Ny-Ålesund. This gradient illustrates the overall sources and transport pathways affecting BC in the Arctic middle troposphere in springtime. The next section will investigate the enhanced concentrations in northeastern Russia and their relation to sources in eastern and southern Asia.

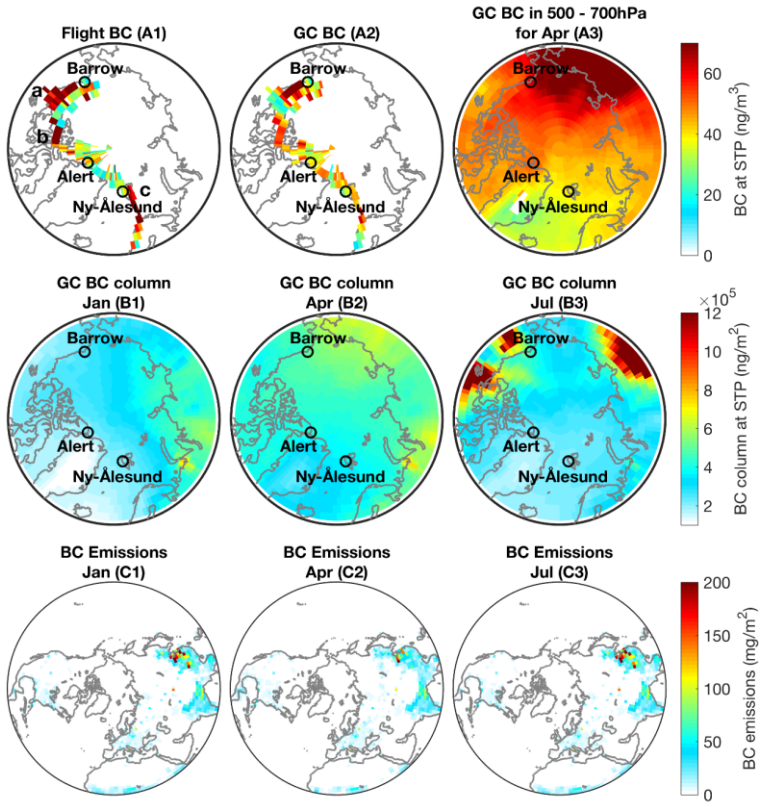

Figure 3-6: Top left: BC concentrations from the NETCARE 2015, PAMARCMiP 2009 and 2011 aircraft campaigns averaged on the GEOS-Chem grid, along with three hotspots labeled as a, b, c. Top middle: BC concentrations from GEOS-Chem simulations coincidently sampled with flight measurements. Top right: BC concentrations between 500-700 hPa simulated with the HTAP+flaring emissions in April averaged over 2009, 2011 and 2015. Circles are ground monitoring stations. Middle: pan-Arctic BC column concentrations simulated with the HTAP+flaring emissions for January (left), April (middle) and July (right) averaged over 2009, 2011 and 2015. All concentrations are at STP. Bottom: total BC emissions for January (left), April (middle) and July (right) averaged over 2009, 2011 and 2015. Letters and numbers in brackets refer to figure numbers.

Figure 3-6 (B1-B3) shows pan-Arctic spatial distributions of BC column (1000 hPa – 300 hPa) concentrations from the HTAP+flaring simulation for January, April and July. Strong spatial and seasonal variation is observed in BC columns with the highest overall concentrations in April and in the eastern Arctic. Emissions remain similar for the three months as shown in Fig. 3-6 C1-C3, indicating that the main reason for the seasonal variation of Arctic BC column is transport efficiency. In July, the enhanced concentrations in western Siberia due to flaring are less obvious, due to more effective wet scavenging in summer. North America exhibits remarkably high BC column in July (Fig. 3-6 B3) from biomass burning as will be discussed further in Sect. 3.2.

Since BC concentrations simulated with HTAP+flaring exhibit overall consistency with the measured seasonal variation, and the measured spatial distributions, we use this inventory in the following simulations for source attributions.

3.4.2 Source attribution of BC in the Arctic

Figure 3-7 (top left) shows the contribution of anthropogenic emissions from regions defined in Fig. 3-1, and of biomass burning from North America and the rest of the world, to springtime airborne BC along the flight tracks of the three aircraft campaigns in Fig. 3-1. Contributions are quantified by excluding regional emissions. At all levels, anthropogenic emissions explain more than 90 % of BC concentrations, of which 56 % is contributed by eastern and southern Asia, followed by Europe with a contribution of 19 %. Biomass burning is minor (~8 %) compared to anthropogenic emissions in the contribution to springtime Arctic BC loadings, and the biomass burning impact on the springtime Arctic almost exclusively originates from regions other than North America. The relative contribution of anthropogenic emissions from each source region varies with altitude, partly reflecting different transport pathways and scavenging efficiencies. The influence of eastern and southern Asia increases considerably with altitude, with a contribution of 66 % between 400 - 700 hPa and 46 % between 900 - 1000 hPa, because transport from mid-latitudes follows isentropic surfaces that slope upward toward the middle or upper troposphere in the Arctic (Klonecki et al., 2003). In contrast, the influence of northern Asia decreases rapidly with altitude by a factor of 10 from the surface to 400 -700 hPa, reflecting transport from sufficiently cold regions along the low-level isentropic surfaces into the Arctic and direct transport within the polar dome (Klonecki et al., 2003; Stohl, 2006). The impact of Europe is roughly uniform throughout the troposphere, suggesting both of the above pathways are possible.

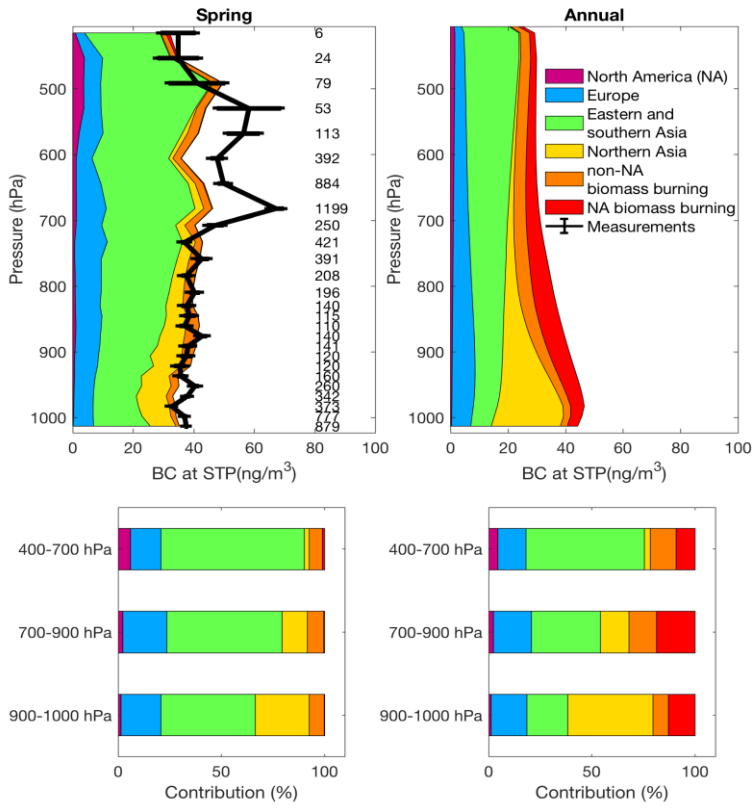

Figure 3-7: Top left: mean spring BC vertical profiles from flight measurements and simulations that are color-coded to anthropogenic sources from regions defined in Fig. 3-1. and biomass burning sources from North America and the rest of the world. Flight measurements and error bars are the same as in Fig. 3-5. Simulated vertical profiles of BC are taken coincidently with flight measurements. Numbers along the y-axis represent the number of measurements in each pressure bin. Top right: annual mean vertical profile of BC for the entire Arctic from simulations that are color-coded to source regions. Concentrations are all presented at STP. Bottom: regional contributions binned by pressure.

The gas flaring contribution to the springtime vertical BC concentration is shown as the red shading in Fig. 3-5. The contribution decreases with altitude from ~20 % near the surface to < 10 % above 800 hPa because flaring occurs almost exclusively below 2 km a.s.l (Stohl et al., 2013) and because the high-latitude sources of flaring limit isentropic lifting in the polar dome (Stohl, 2006).

Figure 3-7 (top right) shows the annual mean vertical contribution of anthropogenic emissions from each source region and of biomass burning to Arctic BC. Anthropogenic emissions from eastern and southern Asia (37 %) and biomass burning emissions (25 %) are major sources of Arctic tropospheric BC, along with a substantial contribution (43 %) from anthropogenic

emissions in northern Asia near the surface (900 -1000 hPa). Unlike in spring, roughly half of biomass burning BC originates from North America in the annual attribution. Compared to springtime, the annual anthropogenic contribution from eastern and southern Asia is smaller and that from northern Asia is substantially larger in the lower troposphere. This reflects that long-range transport from eastern and southern Asia is more favorable in spring due to warm conveyor belts (Liu et al., 2015), and that proximal transport from northern Asia is more efficient in winter owing to the extended Arctic front to the south of northern Asian sources (Stohl, 2006).

The dominant role of eastern and southern Asia in the middle troposphere is consistent with Ikeda et al. (2017) who studied the source attribution of Arctic BC using a tagged tracer method in GEOS-Chem with the HTAP v2.2 emission inventory. The largest contribution from eastern and southern Asia to Arctic BC burden in this study is also consistent with Ma et al. (2013) and Wang et al. (2014a). However, some prior studies suggested that Europe had the largest contribution to the Arctic BC burden (Stohl, 2006; Shindell et al., 2008; Huang et al., 2010b; Sharma et al., 2013). The difference likely arises from trends in anthropogenic emissions with reductions from Europe and increases in eastern and southern Asia as discussed further below.

Figure 3-8 shows the simulated source attribution of surface BC at Alert, Barrow and Ny-Ålesund. For all stations, anthropogenic emissions from northern Asia, eastern and southern Asia, and Europe are major contributors to high concentrations of BC in winter and early spring. In summer, anthropogenic contributions decline rapidly while biomass burning predominantly from North America becomes the primary source. At Alert and Barrow, the largest contributions are anthropogenic emissions from northern Asia in winter (~50 %), and from eastern and sourthern Asia in spring (~40 %). Barrow shows a pronounced peak in summer, more than 90 % of which is explained by biomass burning from North America. At Ny-Ålesund, anthropogenic emissions in Europe and northern Asia are significant sources of BC in winter and early spring with a contribution of ~30 % from each source.

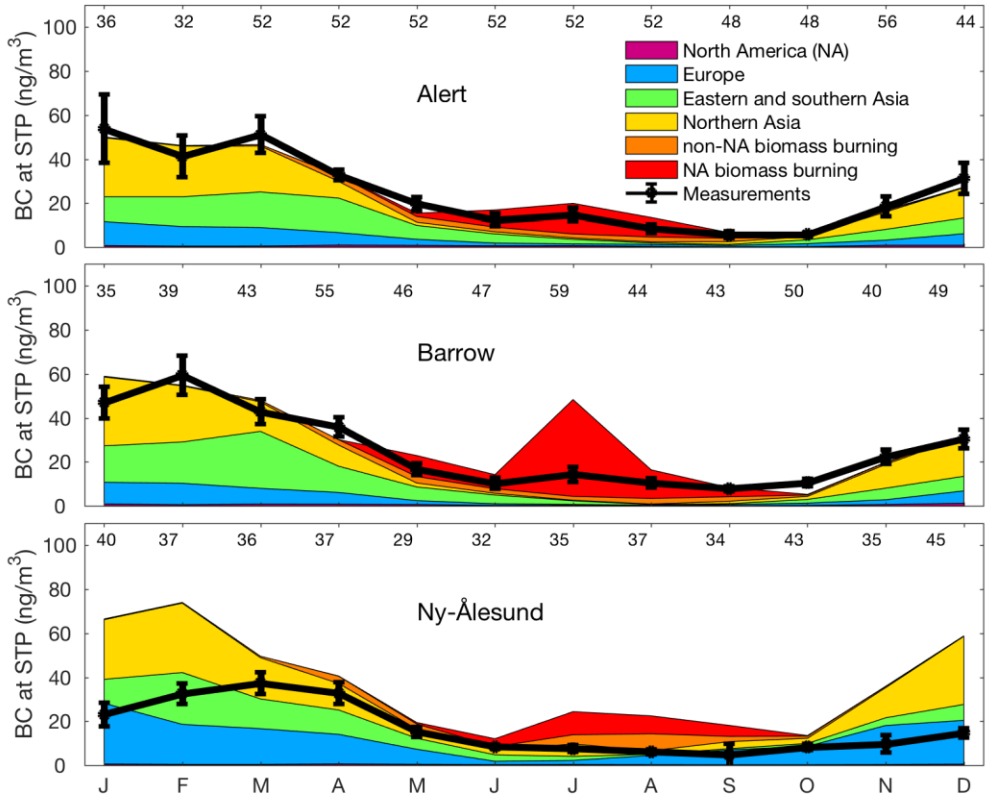

Figure 3-8: Monthly variation of BC surface concentrations at selected Arctic stations from measurements and simulations that are color-coded to anthropogenic sources from regions defined in Fig 3-1. and biomass burning sources from North America and the rest of the world. The measured monthly mean concentrations of BC and error bars are the same as the best estimate of surface BC concentrations in Fig. 3-3. Simulated monthly concentrations are monthly averages of 2009, 2011 and 2015. Numbers below the top x-axis denote the total number of weekly observations from all available instruments in each month. Concentrations are all presented at STP.

The contributions from gas flaring to surface BC concentrations are shown as the red shadings in Fig. 3-3. Flaring accounts for ~25 % of concentrations in winter and spring and less than 5 % in summer at all stations except Ny-Ålesund where flaring contributes 14 % of BC in summer. This result is consistent with Stohl et al. (2013) who studied the flaring contribution to surface BC concentrations at Arctic stations using the FLEXPART model.

We also investigate the influence of international shipping from the HTAP v2 inventory for 2010 on Arctic surface BC concentrations, and found the contribution is less than 1 % at all stations owing to the small magnitude of emissions (< 1 % of total anthropogenic BC emissions globally

and within the Arctic). This source is expected to increase by 16 % by 2050 (Winther et al., 2014).

Our source attribution of Arctic surface BC has consistencies with that of Koch and Hansen (2005) who investigated the origins of Arctic BC using a general circulation model and found that Russia, Europe and south Asia each accounted for 20 % - 30 % of springtime surface BC. However, some studies (e.g. Stohl, 2006; Shindell et al., 2008; Gong et al., 2010; Sharma et al., 2013) suggested lower contributions (< 10 %) from eastern and southern Asia and higher contributions (> 30 %) from Europe than our results. The main difference is due to emission trends such that our anthropogenic BC emissions from eastern and southern Asia are generally 30 % higher than those in earlier studies (e.g. Shindell et al., 2008; Sharma et al., 2013) due to rapid development since 2000 and that our anthropogenic BC emissions in Europe are half those in prior studies due to European emission controls.

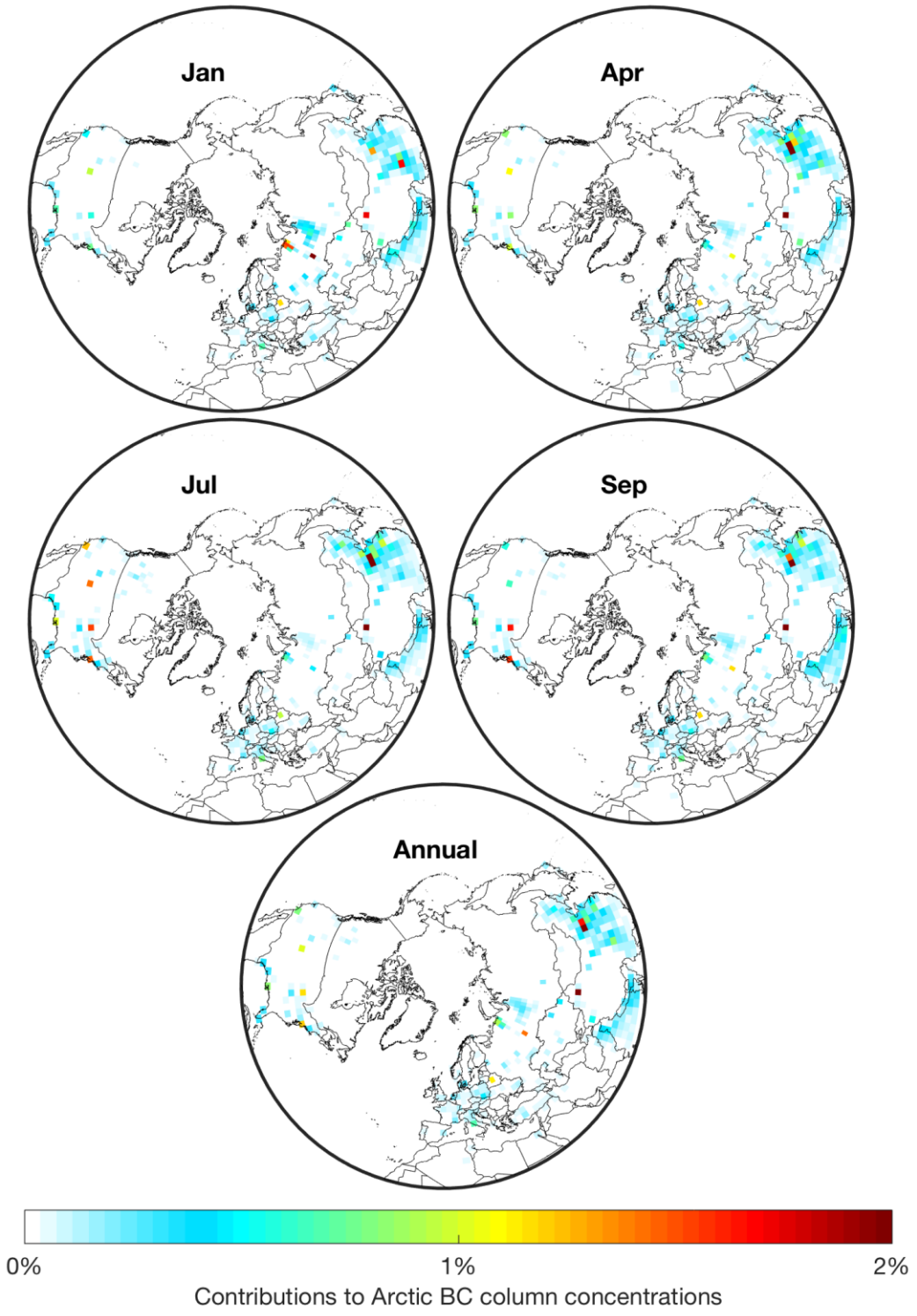

Figure 3-9: Contributions to Arctic BC column concentrations from changes in local emissions (as percent change in Arctic BC column concentration per fractional change in emissions) in 2011. Local emissions include anthropogenic and biomass burning emissions. The annual map is the average of contributions in January, April, July and September calculated with the adjoint model.

Figure 3-9 shows the contributions to Arctic BC column concentrations from changes in local emissions in 2011 as calculated with the GEOS-Chem adjoint. Pronounced seasonal variation and spatial heterogeneity are found. Sources in January are strongly influenced by specific Asian regions including western Siberia, eastern China and the Indo-Gangetic Plain, whereas sources in other seasons are more widespread across Europe and North America. Several hotspots are found in each season.

In January, oilfields in western Siberia have a total impact of 13 % on Arctic BC loadings, of which 4.4 % is from the Timan-Pechora basin oilfield and 6.4 % from the West Siberia oilfields, suggesting that the influence of western Siberia is comparable to the total influence of continental Europe and North America (~ 6.5 % each in January). Considerable flaring emissions (67 % of total flaring emissions north of 60° N in January) and close proximity to the Arctic contribute to the substantial influence of these oilfields in western Siberia. The Indo-Gangetic Plain also exhibits considerable impact (7.2 %) to the Arctic in January, reflecting the substantial emissions there as shown in Fig. 3-1. In April, the influence of western Siberia decreases to 4.4 % with the northward retreat of the Arctic front. In contrast, contributions from emissions in eastern China (25 %) and North America (8.2 %) are enhanced owing to the facilitated transport of air masses from warm regions (e.g. the US and Asia) in spring (Klonecki et al., 2003). Emission contributions to Arctic BC loadings are generally weak in July, but the Tarim oilfield in western China stands out as the second most influential (3.2 %) grid cell to the Arctic, which is comparable to the influence of half of continental Europe (6 %). The Tarim oilfield is located in a high altitude (~1000 m) arid region (Taklamakan Desert). Considerable flaring emissions, less efficient wet scavenging and elevation all facilitate its large contribution to the Arctic. The contribution from North America is the largest (13 %) in July, consistent with the remarkably high BC loadings over high-latitude North America as shown in Fig. 3-6 (B3).

Annually, eastern China (15 %), western Siberia (6.5 %) and the Indo-Gangetic Plain (6.3 %) have the largest impact on Arctic BC loadings, along with a noteworthy contribution from the Tarim oilfield (2.6 %). At continental scales, eastern and southern Asia contributes 40 % to the Arctic BC loadings. Northern Asia, North America and Europe each make a contribution of ~10 %, consistent with the vertical source attribution from sensitivity simulations in Fig. 3-7

(right). BC emissions within the Arctic generally contribute less than 3 % of Arctic BC loadings in all seasons except for January (5 %).

3.5 Conclusions

Airborne measurements of BC concentrations taken across the Arctic during the NETCARE 2015, the PAMARCMiP 2009 and the PAMARCMiP 2011 campaigns, along with long-term ground-based measurements of BC concentrations from three Arctic stations (Alert, Barrow and Ny-Ålesund) were interpreted with the GEOS-Chem chemical transport model and its adjoint to quantify the sources of Arctic BC. Measurements from multiple BC instruments (rBC, EC, EBC) were examined to quantify Arctic BC concentrations. We relied on rBC and EC measurements, and on EBC inferred from PSAP absorption measurements with a MAC calibrated to rBC and EC measurements. The new rBC measurements at Alert differed by up to a factor of 2 from commonly used measurements as discussed by Sharma et al. (2017) and played a major role in our ability to simulate observations at Alert. Our simulations with the addition of seasonally varying domestic heating and of gas flaring emissions were consistent with ground-based measurements of the BC concentrations at Alert and Barrow in winter and spring (rRMSE < 13 %), and represented airborne measurements of BC vertical profile across the Arctic (rRMSE = 17 %), yet underestimated an enhancement of BC concentrations between 500-700 hPa that was affected by several plumes near Alert, Barrow and Ny-Ålesund. The weaker biomass burning influences on the airborne measurements used here than in prior ARCTAS and ARCPAC campaigns facilitated our interpretation for anthropogenic source attribution.

Sensitivity simulations with the GEOS-Chem model were conducted to assess the contribution of geographic sources to Arctic BC. The Arctic tropospheric BC burden was predominantly affected by anthropogenic emissions from eastern and southern Asia (56 % in spring and 37 % annually from 1000 hPa to 400 hPa) with larger contributions aloft (66 % in spring and 57 % annually between 400-700 hPa) than near the surface (46% in spring and 20 % annually below 900 hPa), reflecting long-range transport in the middle troposphere. Anthropogenic emissions from northern Asia had considerable contributions in the lower troposphere (27 % in spring and

43 % annually below 900 hPa) due to low-level proximal transport. Biomass burning contributed 25 % to the annual BC burden.

Surface BC was largely influenced by anthropogenic emissions from northern Asia (> 50 %) in winter and eastern and southern Asia in spring (~ 40 %) at both Alert and Barrow, and from Europe (~ 30 %) and northern Asia (~ 30 %) at Ny-Ålesund in winter and early spring. Biomass burning, primarily from North America, was the most important contributor to surface BC at all stations in summer, especially at Barrow.

Our adjoint simulations indicated pronounced spatial and seasonal heterogeneity in the contribution of emissions to Arctic BC column concentrations. Eastern China (15 %) and western Siberia (6.5 %) had a noteworthy influence on Arctic BC loadings on an annual average. Emissions from as far south as the Indo-Gangetic Plain also had a considerable influence (6.3 %) on the Arctic annually. The Tarim oilfield stood out as the second most influential grid cell with an annual contribution of 2.6 %. Gas flaring emissions from oilfields in western Siberia had a striking impact (13 %) on the Arctic BC burden in January, which was comparable to the total impact of continental Europe and North America (6.5 % each in January).

The increasing BC fraction from eastern and southern Asia at higher altitudes could have significant implications for Arctic warming by extending the trend in increasing BC radiative forcing efficiency found by Breider et al. (2017) driven by strong increase with altitude of the direct radiative forcing of BC (Zarzycki and Bond, 2010; Samset and Myhre, 2015). Furthermore, anthropogenic emissions of BC in southern Asia are projected to increase under several IPCC scenarios (Streets et al., 2004; Bond et al., 2013). The climate implications of BC emissions within the Arctic are concerning given their disproportionate warming effects and the potential for increasing Arctic shipping activity as ice cover declines (Sand et al., 2013). The considerable impact of emissions from China and Indo-Gangetic Plain on the Arctic deserves further investigation. Additional work to reconcile the different BC mass concentrations measured by different instruments would be valuable to reduce uncertainties in BC studies not only in the Arctic but also globally.

3.6 Acknowledgement

The authors acknowledge the financial support provided for NETCARE through the Climate Change and Atmospheric Research Program at NSERC Canada. We also acknowledge the World Data Centre for Aerosol, in which BC measurements from Arctic stations are hosted (http://ebas.nilu.no). We thank all operators at Barrow and Ny-Ålesund stations for maintaining and providing ground-based BC measurements. We also thank the developers of the HTAP and ECLIPSE emission inventories.

Chapter 4: Simulation of airborne trace metals in fine particulate matter over North America

Jun-Wei Xu[1], Randall V. Martin[1,2], Barron H. Henderson[3], Melanie Hammer[1]

[1]Department of Physics and Atmospheric Science, Dalhousie University, Halifax, NS, Canada
[2]Harvard-Smithsonian Center for Astrophysics, Cambridge, MA, USA
[3]Environmental Protection Agency, Research Triangle Park, NC, USA

4.1 Abstract

A representation of trace metal distributions can inform sources of fine particulate matter ($PM_{2.5}$) and can facilitate assessments of $PM_{2.5}$-related health effects. We present a simulation of 12 trace metals: Si, Ca, Al, Fe, Ti, Mn, K, Mg, As, Cd, Ni and Pb over continental North America for 2013 using the GEOS-Chem chemical transport model. Evaluation of modeled trace metal concentrations with observations from more than 200 monitors across North America indicates a promising spatial consistency within a factor of 2. Elements with mostly crustal origins (Si, Ca, Al, Fe, Ti, Mn) show high concentrations over the central and southwestern US due to anthropogenic fugitive dust (AFD) and mineral dust, respectively. Heavy metals (As, Cd, Ni and Pb) are abundant over the eastern US where stack emissions from power plants are considerable. Enhanced concentrations of Mg are observed along the coastline as contributed by sea spray aerosol. K is high over the southeastern US due to biomass burning.

Biases remain in the modeled distributions of trace metals compared to observations. Mostly crustal elements are biased high over the central US due to an overestimation of AFD emissions. Decreasing AFD emissions by 50% reduces the error of modeled crustal element concentrations with observations, especially for Si, Al and Ti with a reduction in error by about 15%. However, reducing AFD emissions generally increases the bias of crustal elements between the simulation and observations, due to a pronounced underestimation over the southwestern US. Heavy metals are largely biased low (45% - 87%), possibly indicating an underestimated magnitude of stack emissions from power plants.

Based on our simulation over North America, K and Ni are significantly correlated with $PM_{2.5}$ ($r>0.7$) and black carbon (BC; $r= 0.8$ for both) annually. Pb is significantly correlated with $PM_{2.5}$ ($r= 0.7$) and BC ($r= 0.8$) in winter, but not in summer ($r<=0$), highlighting the importance of stack emissions to $PM_{2.5}$ in winter. K is significantly correlated with $PM_{2.5}$, organics and BC in summer ($r=0.9$ for all), driven by biomass burning sources of $PM_{2.5}$ in summer.

4.2 Introduction

Metals are important components of airborne fine particulate matter ($PM_{2.5}$) with concentrations ranging from about 20% of $PM_{2.5}$ mass for crustal metals (i.e., Si and Al) to less than 1% of $PM_{2.5}$ mass for heavy metals (i.e., As and Pb; Snider et al., 2016). Metals are toxic and carcinogenic to humans, making them significant contributors to adverse health effects associated with $PM_{2.5}$ (Burnett et al., 2000; Ostro et al., 2007; Bell et al., 2013; Lippmann, 2014; Krall et al., 2016). Through atmospheric deposition, airborne metals are transferred to the surface, posing a potential threat to soil and marine environments (Nagajyoti et al., 2010; Nriagu and Pacyna, 1988). Therefore, representation of trace metal surface concentrations and atmospheric deposition is needed to evaluate their impact on human health and the environment.

Trace metals have both natural and anthropogenic sources. Natural sources include wind-blown mineral dust (Prospero et al., 2002), biomass burning for potassium (K; Pachon et al., 2013) and sea spray aerosol primarily for magnesium (Mg), calcium (Ca), and K (Salter et al., 2016). Anthropogenic fugitive dust (AFD; Tegen et al., 1996) and industrial combustion (Pacyna and Pacyna, 2001) are primary anthropogenic sources. Other minor anthropogenic sources include vehicles (Khodeir et al., 2012) and agricultural fires (Li et al., 2017). Due to their signature sources, trace metals are useful for identifying $PM_{2.5}$ sources. For example, K is commonly used as a marker of wood burning (Tanner et al., 2001; Pachon et al., 2013). Elements with mostly crustal origins such as silicon (Si), Ca, aluminum (Al), iron (Fe), manganese (Mn) and titanium (Ti) can indicate mineral dust sources (Chang et al., 2017; Khodeir et al., 2012a). Heavy metals are associated with industrial combustion, such as nickel (Ni) from oil combustion (Okuda et al., 2007; Thomaidis et al., 2003), arsenic (As) and lead (Pb) from coal combustion (Brimblecombe,

1979; Chang et al., 2017). Thus a representation of trace metal distributions can provide valuable information about $PM_{2.5}$ sources.

Due to heterogeneous emission sources and short atmospheric lifetimes (days), airborne trace metals exhibit strong spatial heterogeneity. For example, surface concentrations for heavy metals can vary by several orders of magnitude from urban regions to rural areas (Khillare et al., 2004; Kim et al., 2002; Venter et al., 2017). Thus, a robust representation of trace metal spatial distributions remains challenging. Nonetheless, recent developments of chemical transport models are promising. Hutzell and Luecken (2008) developed the first simulation of five metals (Pb, Mn, Cd, Ni and Cr) over the United States by using the Community Multiscale Air Quality (CMAQ) model. Dore et al. (2014) developed a simulation of 9 heavy metals (As, Cd, Cr, Cu, Pb, Ni, Zn, Se, Hg) over the United Kingdom by using an atmospheric transport model (FRAME-HM). Both studies found a significant underestimation of modeled metal concentrations and attributed the bias primary to missing wind-blown dust sources and underestimated anthropogenic emissions. Appel et al. (2013) further developed the simulation by including anthropogenic fugitive dust (AFD) and naturally wind-blown dust sources and presented a simulation of 8 mostly crustal elements (Al, Ca, Fe, K, Mg, Mn, Si and Ti) over the United States by using the CMAQ model. They found a pronounced overestimation (40% - 190%) in the simulation. Wai et al. (2016) developed a global simulation of As with the GEOS-Chem model and found a general consistency with observations worldwide and a bias within a factor of 3 over the United States.

Building upon recent developments of the National Air Toxic Assessment (NATA) inventory over North America for 2011 (https://www.epa.gov/national-air-toxics-assessment/2011-nata-assessment-results), we present an initial simulation of 12 trace metals over continental North America at a fine resolution of 0.25 ° x 0.31 ° using the GEOS-Chem chemical transport model. The 12 trace metals include 6 mostly crustal elements: Si, Ca, Al, Fe, Mn and Ti; 4 heavy metals: As, Cd, Ni, and Pb; and 2 other metals: K and Mg. Section 2 describes model simulations developed in this study. Section 3 elaborates the observations of trace metals for model evaluation. Section 4 presents surface concentrations and wet deposition of trace metals, along

with correlations between trace metals and $PM_{2.5}$. Section 5 provides the implications of this study.

4.3 Simulation development

We use the nested GEOS-Chem global chemical transport model (version 11-01; www.geos-chem.org) to simulate trace metals, $PM_{2.5}$ and its major components over North America for 2013.

The simulation of trace metals from anthropogenic sources (Section 4.3.1) is based on a nested passive species simulation over North America (60°W–130°W, 9.75°N–60°N) at 0.25° x 0.3125° horizontal resolution with 47 vertical levels (1013.25 hPa – 0.01 hPa) driven by assimilated meteorological data from the Goddard Earth Observing System (GEOS-FP) of the NASA Modeling and Assimilation Office (GMAO). The model is initialized with an arbitrary small concentration for all elements. A simulation that is initialized with annual median concentrations by element from observations is in progress.

The simulation of trace metals from natural sources (Section 4.3.2) is based on the simulation of $PM_{2.5}$ and its chemical composition that is nested over the same domain in North America at 0.5° x 0.625° horizontal resolution with the same vertical levels driven by assimilated meteorological data from the Modern-Era Retrospective analysis for Research and Applications, Version 2 (MERRA-2). A simulation driven by the GEOS-FP meteorological data at 0.25° x 0.3125° resolution is under development to match the simulation from anthropogenic sources.

Boundary conditions for the nested domain is provided by a global simulation at 4° x 5° spatial resolution (Wang et al., 2004). We spin up the model for 1 month before any simulations to remove the effects of initial conditions on simulations.

4.3.1 The simulation of trace metals from anthropogenic sources

Trace metals from anthropogenic sources are simulated by building upon the passive species simulation of GEOS-Chem. We develop the passive species simulation here to include anthropogenic emissions of 12 trace metals based on the NATA2011 inventory, along with sectoral emission factors from the National Emission Inventory (NEI) for 2011, since NEI and NATA annual total emissions for each metal for 2011 are nearly identical (<1% difference). A simulation that includes anthropogenic metal emissions over Canada is under development.

Figure A4-1 shows anthropogenic metal emissions in the NATA2011 inventory. Anthropogenic metal emissions have 5 major sectors: AFD, power plants, anthropogenic fires, mobile sources and stack emissions. For mostly crustal elements, AFD contributes about 50% of their annual total anthropogenic emissions. For Mg, AFD accounts for 40% of its anthropogenic emissions, along with another 20% from mobile sources. Anthropogenic K has large contributions from AFD (40%) and non-point (30%) sources. Reff et al. (2009) found that aluminum processing, iron and steel production are major non-point sources of anthropogenic K, with contributions of 10% and 21%, respectively. In contrast to these metals, heavy metals primarily arise from stack emissions that account for more than 55% of their total anthropogenic emissions.

As will be discussed in Section 4.5, AFD emissions in NATA2011 have been largely overestimated. We thereby reduce AFD emissions by 50% in our simulations to better represent observations. Simulations without AFD reductions are shown in appendix.

We assume and parameterize all trace elements to undergo the same wet and dry deposition processes as they are for mineral dust. A detailed description of deposition schemes of mineral dust can be found in Bey et al. (2001) and Liu et al. (2001) with updates from Fisher et al. (2011), Wang et al. (2011) and Wang et al. (2014). The precise scavenging treatment remains uncertain due to considerable variations in metal fractional solubility (Schroth et al., 2009). However, our simulated metal surface concentrations and atmospheric deposition are nearly identical (R^2>0.96) if they are scavenged with high solubility as sulfate or with low solubility as mineral dust.

4.3.2 The simulation of trace metals from natural sources

The simulation of mineral dust follows the Dust Entrainment and Deposition (DEAD) mobilization scheme (Zender et al., 2003), combined with a topographic source function (Ginoux et al., 2001; Chin et al., 2002) as described in Fairlie et al. (2007), and an optimized dust particle size distribution as described in Zhang et al. (2013). Table 4-1 shows the mass fractions of trace metals in mineral dust based on measurements for 2005-2015 at Phoenix, Arizona by the Interagency Monitoring of Protected Visual Environments (IMPROVE; http://views.cira.colostate.edu/fed/) network. Cd measurements are not used here since more than half of Cd measurements are below the minimum detection limit (1 ng m^{-3}; Solomon et al., 2014). Instead, we assume the mass fraction of Cd in mineral dust is about 10% of that of As (Nriagu and Pacyna, 1988). The mass fractions are applied across the US to estimate trace metal concentrations contributed by mineral dust.

Table 4-1: Mass fractions of median trace metal concentrations in fine mineral dust based on measurements at Phoenix, AZ, USA by the IMPROVE network for 2005-2015.

Si	Fe	Al	Ca	K	Mg	Ti	Mn	Pb	Ni	As	Cd
15%	7.5%	5.4%	5.4%	4.1%	1.5%	0.52%	0.15%	0.07%	0.01%	0.007%	0.0007%

The simulation of sea spray aerosol follows Jaeglé et al. (2011). We assume that sea spray aerosol contains 4 % Mg, 1 % Ca, and 1 % K as used in Salter et al. (2016).

Biomass burning emissions for K are calculated from the Global Fire Emissions Database version 4 inventory (GFED4; Randerson et al., 2015). GFED4 combines satellite information on fire activity and vegetation productivity to estimate globally gridded monthly burned area (including small fires) and fire emissions, and then apply emission factors to calculate specific aerosol emissions. Table 4-2 shows the emission factors for K from various vegetation types as used in our simulation. These emission factors are based on Andreae and Merlet (2001) and Akagi et al. (2011) as used for GFED4. When emission factors are given as a range or multiple emission factors are found, we take the mean. Emission factors for K from peat and woodland were not available. We assume the emission factors for K from peat and woodland as half that of

BC used in GFED4, which is generally true for the other vegetation types.

Table 4-2: Emission factors for potassium (K) from various types of biomass burning.

	Emission factors (g/kg)	References
Agricultural waste	0.28	Andreae and Merlet (2001)
Deforestation	0.29	GFED4 (Akagi et al., 2011)
Extratropical forest	0.25	Andreae and Merlet (2001)
Peat	0.28	Half of BC emission factors in GFED4 (Akagi et al., 2011)
Savanna	0.23	GFED4 (Akagi et al., 2011)
Woodland	0.28	Half of BC emission factors in GFED4 (Akagi et al., 2011)

4.3.3 The simulation of $PM_{2.5}$ and its chemical composition

$PM_{2.5}$ is simulated with the standard GEOS-Chem that includes a fully coupled treatment of oxidant-aerosol chemistry (Bey et al., 2001; Park et al., 2004) with carbonaceous aerosol (Park et al., 2003), sea salt (Jaeglé et al., 2011), mineral dust (Fairlie et al., 2007), secondary inorganic aerosol (Park et al., 2004) and secondary organic aerosol (SOA; Pye et al., 2010). We implement the additional SOA formation from aqueous-phase isoprene uptake following Marais et al. (2016). Gas-aerosol phase partitioning is simulated using the ISORROPIA II thermodynamic scheme (Fountoukis and Nenes, 2007). Aerosol uptake of N_2O_5 is given by Evans and Jacob, (2005). HNO_3 concentrations are reduced following Heald et al. (2012). Aerosol optics affect photolysis rates as described by Martin et al. (2003) with updates on aerosol size distribution (Drury et al. 2010), dust optics (Ridley et al. 2012) and brown carbon (Hammer et al. 2016). Dry and wet deposition scheme is described in Bey et al. (2001) and Liu et al. (2001) with updates from Fisher et al. (2011), Wang et al. (2011) and Wang et al. (2014). Organic carbon (OC) is converted to particulate organic mass (OM) following Philip et al. (2014). We calculate ground-level $PM_{2.5}$ at 35% relative humidity to follow common measurement protocols.

Anthropogenic emissions are based on the NEI 2011 for the United States (Travis et al., 2016) and the Criteria Air Contaminants (CAC) inventory for Canada (Kuhns et al., 2005). Non-anthropogenic emissions include biomass burning emissions (GFED4; Randerson et al., 2015), biogenic emissions (MEGAN; Guenther et al., 2012), soil NOx (Wang et al., 1998; Yienger and Levy, 1995), lightning NOx (Murray et al., 2012), aircraft NOx (Stettler et al., 2011; Wang et al., 1998), ship SO_2 (Lee et al., 2011) and volcanic SO_2 emissions (Fisher et al., 2011).

4.4 Ground-based measurements of trace metals and $PM_{2.5}$ over North America

4.4.1 Ambient surface concentrations

We collect measurements of the twelve trace metals (Si, Ca, Al, Fe, Mn, Ti, K, Mg, As, Cd, Ni and Pb), dust and $PM_{2.5}$ from IMPROVE (Malm et al., 2011) and Chemical Speciation Network (CSN; http://www. epa.gov/ttnamti1/speciepg.html) over the United States for 2005-2015, and from National Air Pollution Surveillance (NAPS; http://www.ec.gc.ca/rnspa-naps/) program over Canada for 2005-2015. The IMPROVE network consisted of 167 sites primarily located in rural areas such as national parks in the western United States. The CSN network consisted of 182 sites primarily located in urban areas in the eastern United States. There are 14 sites available from NAPS.

IMPROVE and CSN measure $PM_{2.5}$ by federal reference method (FRM) sampler (Malm et al., 2011). NAPS measures $PM_{2.5}$ by dichotomous sampler and supplementary FRM samplers (Galarneau et al., 2016). All the three networks collect $PM_{2.5}$ samples for 24 hours every third day and analyze trace elements in $PM_{2.5}$ samples with x-ray fluorescence (XRF; Dabek-Zlotorzynska et al., 2011; RTI, 2009).

For CSN measurements, we remove all industrial sites to better represent ambient conditions. For both CSN and IMPROVE networks, only sites with at least 75% of the scheduled sample days per season containing valid records are retained for developing annual averages. These filters remove about 30% of measurements.

Dust in $PM_{2.5}$ including naturally windblown mineral dust and anthropogenic windblown dust is not directly measured by these networks. Following equation (1) developed by Malm et al. (1994), we calculate dust concentrations based on trace metal concentrations measured by IMPROVE, CSN and NAPS.

$$\text{Dust} = (2.20\times\text{Al}) + (2.49\times\text{Si}) + (1.63\times\text{Ca}) + (2.42\times\text{Fe}) + (1.94\times\text{Ti}) \quad (1)$$

Simulated anthropogenic dust concentrations are also calculated from simulated anthropogenic metal concentrations following equation (1).

4.4.2 Wet deposition fluxes

Measurements of Mg, K and Ca wet deposition fluxes are collected from the National Atmospheric Deposition Program (NADP; http://nadp.slh.wisc.edu/NTN/) over the United States for 2010-2016. A total of 266 sites from NADP are used in this study. NADP collects precipitation samples in a AerochemMetrics Wet-Dry Collector on a weekly basis. Precipitation depths are measured in a Belfort recording rain gauge. Mg^{2+}, K^{+} and Ca^{2+} ions in precipitation samples are analyzed by Inductively Coupled Plasma-Optical Emission Spectroscopy (ICP-OES; Vermette et al., 1995). Ion concentrations in precipitation are then converted to precipitation-weighted deposition fluxes.

4.5 Results and discussion

Figure 4-1 shows annual median trace metal concentrations over North America for 2013 with AFD emissions reduced by 50%. The observed spatial distribution of trace metals exhibits strong heterogeneity, reflecting various emission sources. Mostly crustal elements are abundant over the southwestern US, whereas heavy metals that primarily arise from industrial activities are abundant over the eastern US. Mg exhibits enhanced concentrations over the oceans and coast due to contributions from sea spray aerosol. Crustal elements have greater concentrations than heavy metals by about 3 orders of magnitude. Measurements across the US indicate that Si has the highest annual concentration of 86 ng m^{-3} among all the mostly crustal elements, followed by

Ca (35 ng m^{-3}) and Fe (35 ng m^{-3}). Heavy metals are typically below 1 ng m^{-3}. All these features are generally represented in the simulated distributions, yet model-measurement discrepancies are found. Compared to Fig. A4-2 that shows results without the reduction of AFD emissions, the overestimation of crustal elements over the central US are largely corrected and errors in modeled estimates are generally reduced in Fig. 4-1, especially for Si, Al and Ti (NME reduced by about 15%). However, the reduction of AFD emissions in Fig. 4-1 generally amplifies the negative biases of modeled crustal element concentrations compared to Fig. A4-2. This is due to an underestimation over the southwestern US. Since southwestern US is frequently affected by locally generated windblown dust (Kavouras et al., 2009), the underestimation possibly arises from a lack of sub-grid dust generation processes such as convective dust storms in the model (Foroutan et al., 2017). Heavy metal concentrations show large negative bias. As and Pb are biased low all over the US by about 80%, likely implying an underestimation of sources. Ni is overall underestimated by 45%, but interestingly exhibits a slight overestimation over the majority of the eastern US. K and Mg are well represented by the model with biases of 3% and 11%, respectively. $PM_{2.5}$ mass concentrations are well represented with the lowest NME.

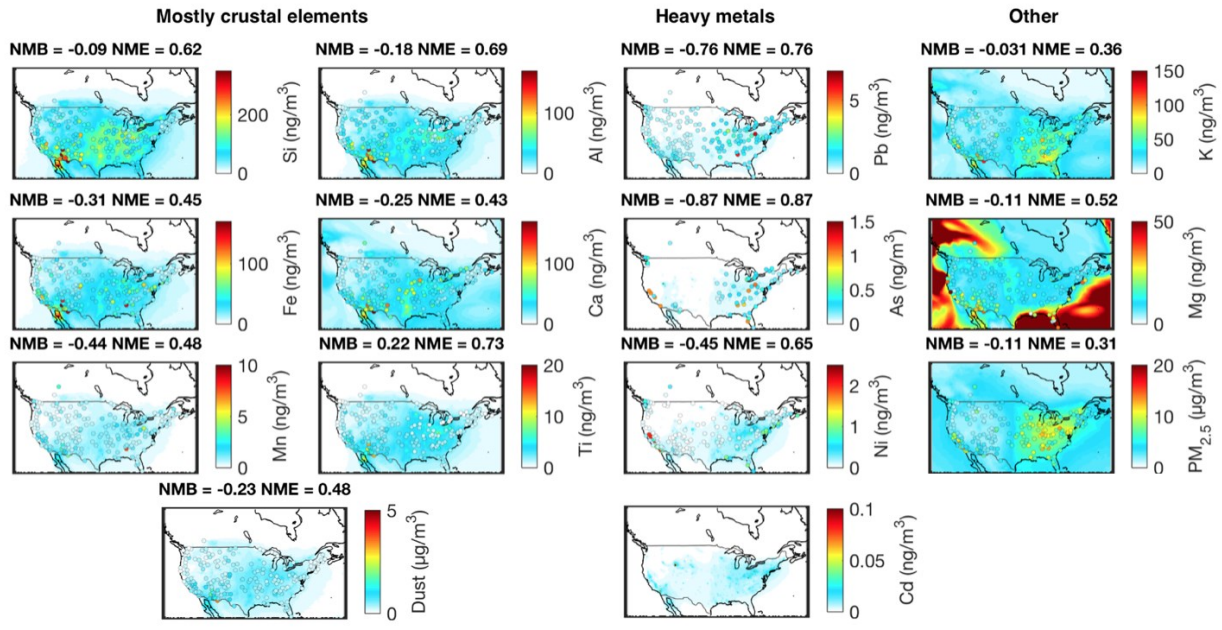

Figure 4-1: Annual median trace metal, dust and $PM_{2.5}$ concentrations over North America. Background colors are simulated concentrations for 2013 at 0.25° x 0.3125° resolution, with contributions from mineral dust, sea salt and biomass burning that are interpolated from a simulation at 0.5° x 0.625°

resolution. Anthropogenic fugitive dust (AFD) emissions are reduced by 50% in the simulation. Filled circles are median observations from the IMPROVE, the CSN and the NAPS networks for 2005-2015. Observations of Cd are excluded because more than half of its measurements are below the minimum detection limit (24 ng m^{-3}). Dust includes natural and anthropogenic windblown mineral dust. Statistics are normalized mean bias (NMB) and normalized mean error (NME).

Similar discrepancies between simulations and observations have also been found in other studies. Hutzell and Luecken (2008) simulated Pb, Mn, Cd, As and Cr over the United States by using the CMAQ model with the NEI 1999 emission inventory, and found an underestimation of about a factor of 2 in modeled metal concentrations. A large underestimation of heavy metals was also presented in Dore et al. (2014) in their simulation over the United Kingdom by an atmospheric transport model (FRAME-HM). Our As model-observation consistency (within a factor of 2) is slightly better than that in Wai et al. (2016) who found a factor of 3 difference in their simulation of As by using the GEOS-Chem model with NATA 1999 emissions over the United States. Appel et al. (2013) found an overall overestimation of K, Mg and crustal elements by 30% - 190% over the United States by using the CMAQ model with the NEI2005 emission inventory. Our simulation without reducing AFD by 50% also exhibits an overestimation (< 50%) of these elements, which is largely corrected with the reduction of AFD emissions.

Figure 4-2 shows annual mean precipitation-weighted wet deposition fluxes of Mg, K and Ca for 2013 with AFD emissions reduced by 50%. Observed fluxes exhibit different spatial distribution for Mg, K and Ca, reflecting their different emission sources. Mg and K fluxes are abundant along the east coast since sea spray aerosol is one of their major sources. Considerable wood combustion and agricultural burning over the eastern US also contribute to enhanced K in precipitation. Ca wet deposition is the largest over the central US. These spatial features in observations are generally represented in the simulation, yet the simulation largely underestimates the magnitude by more than 80%, larger than the model bias for ground-level concentrations (< 25%) for these metals as shown in Fig. 4-1. The underestimation is not associated with reduced AFD emissions since the larges bias remains in Fig. A4-3 in which AFD emissions are not reduced. The underestimation is not due to precipitation in the simulation and observations either as their difference is minor (NMB=6.7% for annual total precipitation). For K

and Mg, the bias is evident along the coastline. Restricting the model-observation comparison of K and Ca to about 25 km away from the coastline reduces the magnitude of NMB and NME by about 5%. Since mineral dust is an important source for all three elements (Table 4-1), the underestimation of dust aloft transported from Sahara (Ridley et al., 2012) may explain the pronounced negative bias over the central US for all three elements. Given the large discrepancy in wet deposition fluxes, we focus the remainder of our analysis on boundary layer concentrations that are better simulated.

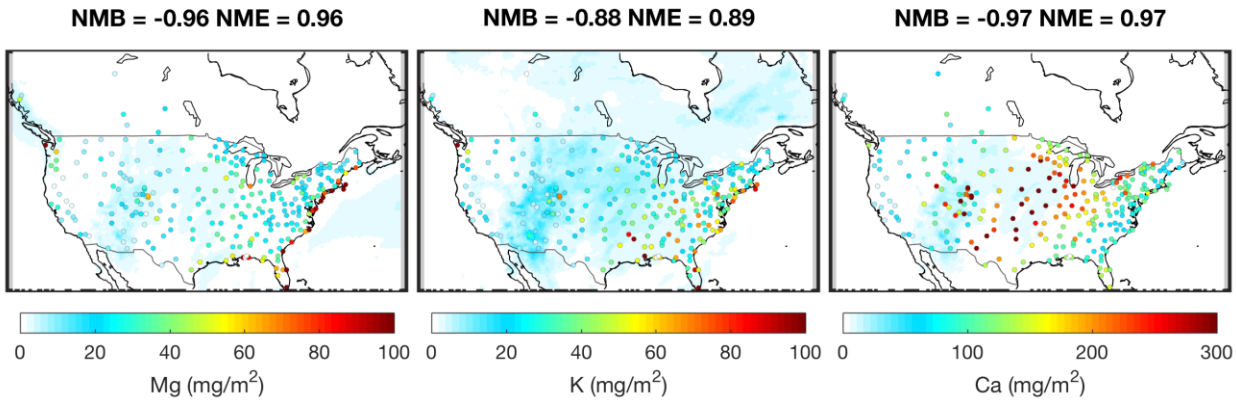

Figure 4-2: Annual mean precipitation-weighted wet deposition fluxes of trace metals. Background is the simulated fluxes for 2013 at 0.25° x 0.3125° resolution, with contributions from mineral dust from all size bins, sea salt and biomass burning that are interpolated from a simulation at 0.5° x 0.625° resolution. AFD emissions are reduced by 50% in the simulation. Filled circles are mean observations from the NADP network for 2010-2016.

Table 4-3 summarizes the boundary layer budget of trace metals as simulated in the GEOS-Chem model for 2013. Anthropogenic emissions are the primary source for most metals, except for K and Mg. K is primarily emitted from biomass burning that contributes to 98% of its emissions in North America. Mineral dust and sea spray are major sources of Mg, accounting for 44% and 30% of its emissions, respectively. Wet and dry deposition are weighted evenly in the removal of trace metals, except that Mg, K and Ca are mainly removed by wet deposition. Table 4-3 also shows that a considerable amount of trace metals is transported out of the continental North America, with implications for the marine environment (Mahowald et al., 2018).

Table 4-3: Boundary layer budget of trace metals over continental North America (NA) in the GEOS-Chem simulation for 2013.

	Emissions		Wet deposition	Dry deposition	Export from the boundary layer of
	Natural (Gg)	Anthropogenic (Gg)	(Gg)	(Gg)	continental NA (Gg)
Fe	32	35	6.4	7.2	54
Al	24	45	5.8	6.7	56
Ti	2.2	4.2	0.54	0.61	5.3
Mg	13	4.9	34	2.8	-19
K	9.3E+02	45	20	11	9.4E+02[a]
Si	65	1.3E+02	17	19	1.6E+02[a]
Ca	25	40	14	6.7	45
Mn	0.67	1.6	0.14	0.16	2.0
As	0.030	0.078	0.0077	0.0079	0.093
Cd	0.0030	0.02	0.0011	0.0011	0.021
Pb	0.30	0.53	0.06	0.061	0.71
Ni	0.059	0.34	0.028	0.024	0.35

[a]Number difference due to rounding

Figure 4-3 shows concentration spatial correlations of trace metals with $PM_{2.5}$ and its major components over North America. In the annual relationship, K is highly correlated with $PM_{2.5}$ (r=0.8), OM (r = 0.7) and BC (r=0.8), driven by biomass burning source of $PM_{2.5}$. The correlation of Ni with $PM_{2.5}$ (r=0.7) and BC (r=0.8) reflects the relationship of oil combustion with $PM_{2.5}$ concentrations. The correlations between trace metals and $PM_{2.5}$ in winter are similar to those annually, while their correlations with BC are more pronounced in winter. It is interesting that Pb is highly correlated with BC in winter (r=0.9), but not in other seasons, highlighting the associations of stack emission with $PM_{2.5}$ in winter. Summer exhibits a correlation near unity sof K with $PM_{2.5}$, BC and OM, reflecting pronounced biomass burning in summer. The correlation between trace metals and dust is also greater in summer, reflecting the contribution of dust sources to $PM_{2.5}$ in summer.

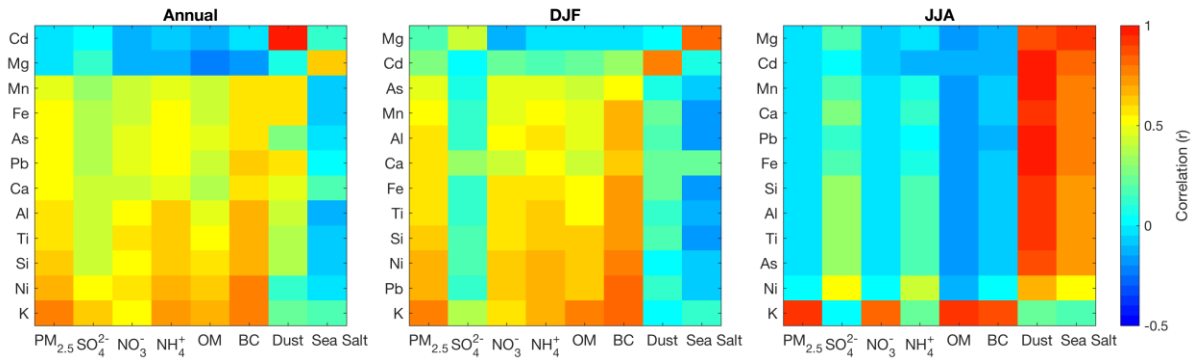

Figure 4-3: Annual and seasonal concentration spatial correlations of trace metals with $PM_{2.5}$ and its major components over continental North America as simulated by the GEOS-Chem model. Trace metals from bottom to top are in the order of their correlations with $PM_{2.5}$.

4.6 Implications

This work presents an initial simulation of 12 trace metals over the continental North America using the GEOS-Chem model. Our modeled trace metal concentrations and wet deposition exhibit promising spatial consistency with observations from more than 200 monitors across North America. These initial results illustrate the potential for further development of a more thorough and comprehensive trace metal simulation. Further improvement will benefit from a better understanding of the spatial distribution and the magnitude of emissions from AFD and power plants. Investigation into the influence of long-range transport of dust on crustal element deposition will help to understand the pronounced negative bias over the central US. Observations of wet deposition for more metals especially toxic metals will not only better constrain the simulation but will also be beneficial for studies on the impact of metal deposition on soil and marine environment. The development of emissions of more metals such as zinc (Zn) and vanadium (V) will be useful for source appointment of $PM_{2.5}$ and for health effect studies. Results from this work provide valuable basis for further investigations into the health effects of trace metals and $PM_{2.5}$, and the effects of airborne metal deposition on marine and soil environment.

4.7 Acknowledgements

This work is financially supported by Health Canada. We acknowledge the Federal Land Manager Environmental Database (http://views.cira.colostate.edu/fed/) and the Environment and Climate Change Canada (http://maps-cartes.ec.gc.ca/rnspa-naps/data.aspx) for hosting observation data. We thank the IMPROVE, CSN, NAPS, NADP and NATA teams for providing data used in this study.

4.8 Appendix

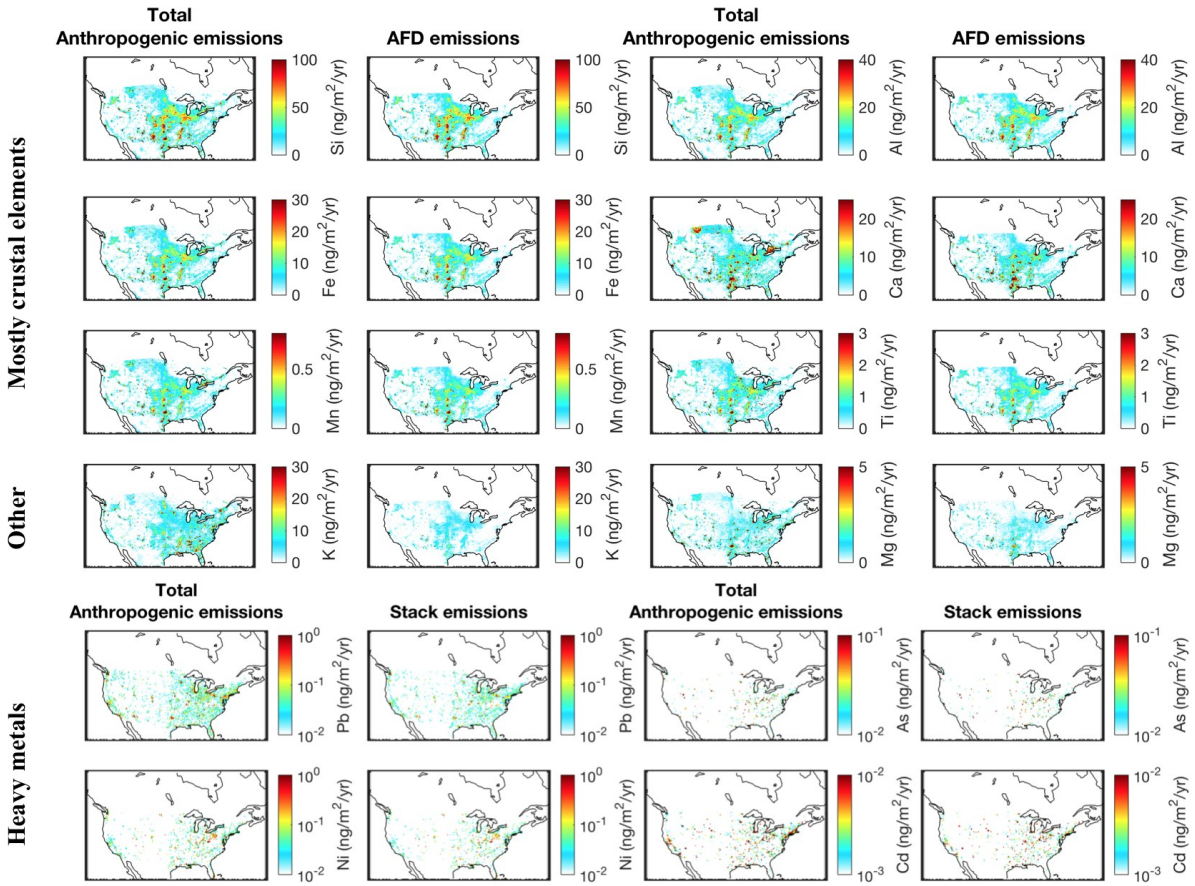

Figure A4-1: Anthropogenic emissions of trace metals. Total anthropogenic emissions are from the NATA emission inventory for 2011. Sectoral emissions are calculated by applying sectoral emission factors from the NEI2011 inventory to annual total emissions from NATA2011.

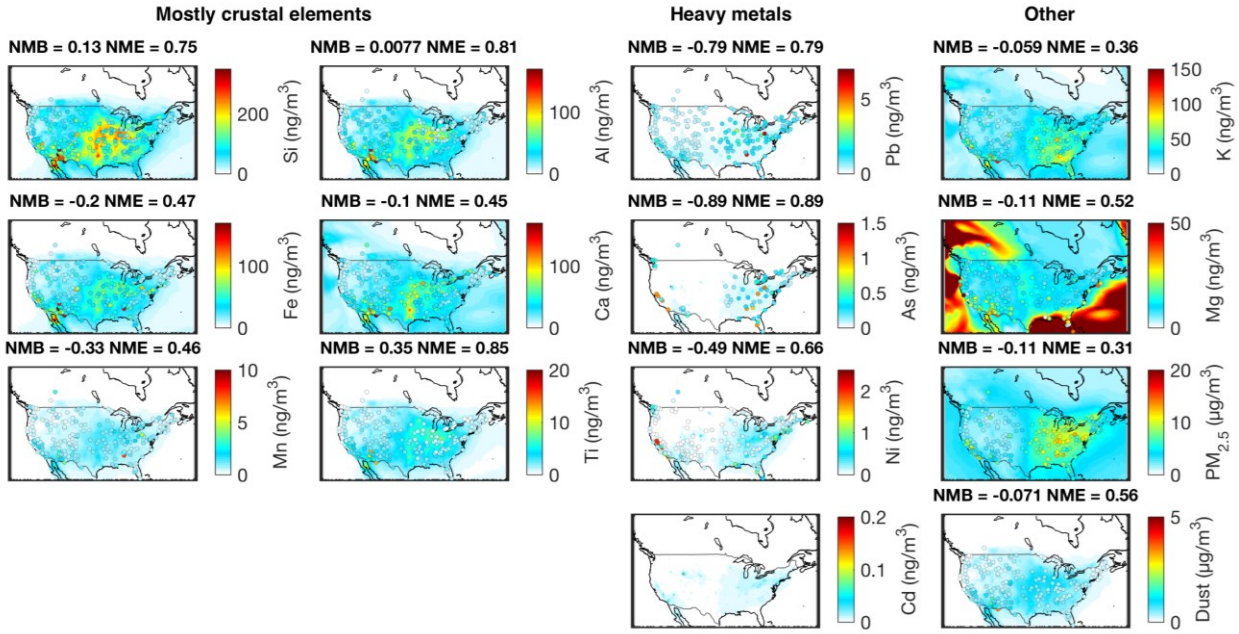

Figure A4-2: Similar to Fig. 4-1, but without reducing AFD emissions in the simulation.

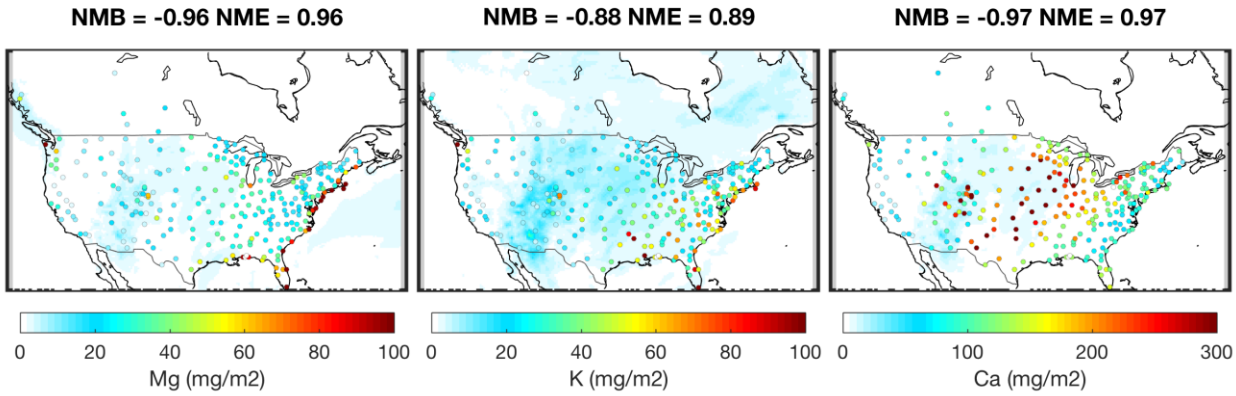

Figure A4-3: Similar to Fig. 4-2, but without reducing AFD emissions in the simulation.

Chapter 5: Conclusions

5.1 Summary

$PM_{2.5}$ is the leading environmental risk factor for the global burden of disease, with a number of adverse health effects associated with BC and metal components. BC also makes a considerable contribution to Arctic warming. Thus a strong understanding of atmospheric processes that impact $PM_{2.5}$ and its chemical components are essential for health and climate related research. This thesis presents results from three projects that show how satellite remote sensing, airborne and ground-based measurements can be used in combination with a chemical transport model to enhance our understanding of emissions, transport and deposition of $PM_{2.5}$ and its chemical components regionally and globally.

In Chapter 2, we estimated $PM_{2.5}$ and its chemical composition concentrations over eastern China by using the GOCI AOD combined with the GEOS-Chem model. We applied additional cloud filters to GOCI AOD, which improved its agreement with ground-based measurements (MFB from 6.7% to -1.2%). The annual averages of GOCI-derived and in situ measurements of $PM_{2.5}$ exhibit a significant correlation (r^2=0.66) with a slope close to unity (1.01). Monthly averages of GOCI-derived $PM_{2.5}$ are within an error of 20%. The GEOS-Chem simulation revealed that SIA (SO_4^{2-}, NO_3^-, NH_4^+) and OM were dominant components of GOCI-derived $PM_{2.5}$ throughout the year. NO_3^- had a winter maximum due to its favorable formation at low temperatures. OM increased by a factor of 2 in winter, primarily driven by biofuel emissions for heating in northern China. The population-weighted GOCI-derived $PM_{2.5}$ for eastern China was 53.8 μg m^{-3}, suggesting that ~400 million people in China live in regions with $PM_{2.5}$ concentrations exceeding the suggested 35 μg m^{-3} by the World Health Organization (WHO) Air Quality Interim Target-1. Further development on GOCI cloud masking, such as constraints from temporal smoothness as demonstrated in this work, would improve the accuracy aerosol retrievals (Choi et al., 2018). The pronounced increase of SIA and OM in $PM_{2.5}$ in winter warrants further studies on their sources and formation mechanisms (Yao et al., 2018).

In Chapter 3, we interpreted the recent airborne and ground-based measurements of Arctic BC with the GEOS-Chem model to understand geographical sources of Arctic BC. Our simulation with the HTAP+flaring emissions best represented airborne and surface measurements of BC concentrations in the Arctic (rRMSE < 20%), yet underestimated an enhanced BC concentration between 500-700 hPa that was affected by several plumes near Alert, Barrow and Ny-Ålesund. With these emissions, our simulation revealed that eastern and southern Asia were the primary sources of Arctic BC in the mid-troposphere, contributing to more than 50% of BC between 400-700 hPa. Northern Asia was the largest source of surface BC in the Arctic with a contribution of 47% below 900 hPa. Biomass burning, primarily from North America, contributed 25 % to the annual BC burden and was a major reason for a BC enhancement in summer at surface level. Our adjoint simulation showed that oilfields in western Siberia had a striking impact (13 %) on the Arctic BC burden in January, which was comparable to the total impact of continental Europe and North America (6.5 % each in January). Future work to reconcile the differences in BC measurements by different instruments would be valuable to reduce uncertainties in BC studies not only in the Arctic but also globally (Bond et al., 2013; Sharma et al., 2017). Further improvement on model simulation (i.e., wet scavenging) to better represent observations at Ny-Ålesund will help understand aerosol processes in the Arctic. The considerable influence of the Indo-Gangetic Plain on the Arctic deserves further investigation.

In Chapter 4, we presented an initial simulation of 12 trace metals in $PM_{2.5}$ over continental North America by using the GEOS-Chem model. Our simulated trace metal concentrations and wet deposition show promising spatial consistency with observations from more than 200 monitors across North America. Mostly crustal elements (Si, Ca, Al, Fe, Ti and Mn) exhibited high concentrations over the central and southwestern US due to anthropogenic fugitive dust and mineral dust, respectively. Heavy metals (As, Cd, Ni and Pb) were abundant over the eastern US. Mg concentrations were enhanced along the coastline due to contributions from sea salt aerosol. K was high over the southeastern US due to biomass burning. Further development on trace metal simulations would benefit from a better understanding of emissions from AFD and power plants (Appel et al., 2013; Dore et al., 2014). Investigation into the influence of long-range transport dust on crustal element deposition will help to understand the negative bias over the

central US. The development of emissions of more metals such as zinc (Zn) and vanadium (V) will be useful for identifying $PM_{2.5}$ sources.

5.2 Implications on Future Work

GOCI-derived $PM_{2.5}$ and its chemical composition over eastern China provides a basis for health effect studies of $PM_{2.5}$. Given extraordinary high concentrations of $PM_{2.5}$ in winter as found in our study, health risks associated with daily and short-term exposure to this level of pollution is needed. Several studies have suggested that carbonaceous aerosols might be more toxic than other major $PM_{2.5}$ components (i.e., nitrate, sulfate and dust particles; Tuomisto et al., 2008; Lelieveld et al., 2015). Given the considerable contribution of carbonaceous aerosols to $PM_{2.5}$ mass annually, a detailed evaluation of composition-specific health effects associated with $PM_{2.5}$ is necessary.

Sources of Arctic BC revealed in Chapter 3 offers a reference for the assessment on climate impact of BC and the development of mitigation strategies. Potential enhancement of positive radiative forcing due to large Arctic BC concentrations in the mid-troposphere needs to be assessed, since the direct radiative forcing of BC increases with altitude (Zarzycki and Bond, 2010; Samset and Myhre, 2015). The positive forcing due to Arctic BC in the mid-troposphere may be further enhanced with the projected increase of anthropogenic emissions from southern Asia (Streets et al., 2004; Bond et al., 2013), which warrants a detailed evaluation. Although shipping emissions within the Arctic are minor in our study, the projected increase of shipping activities within the Arctic (Sand et al., 2013) deserves more attention as within-Arctic emissions are likely to have a large radiative forcing per emission (Sand et al., 2013; Law et al., 2017).

The simulation of airborne trace metals developed in this thesis provides an exciting opportunity for studies on health and the environment impacts of particulate metals. Specific health effects of metals in $PM_{2.5}$ need to assessed as some metals (i.e., Pb, As and Cd) are carcinogenic. Using trace metals as indicators of $PM_{2.5}$ sources, the simulation of trace metals can also facilitate the source attribution of $PM_{2.5}$ and source-specific health effect studies of $PM_{2.5}$ (Huang et al.,

2018). The simulation of trace metal deposition to the oceans, soil and vegetation can be further developed to better understand its impact on the ecosystem over a large temporal and spatial scale and the impact of a wide range of metals including both nutrients (such as Fe) and toxic heavy metals (Mahowald et al., 2018).

Reference

Abel, S.J., Haywood, J.M., Highwood, E.J., Li, J., Buseck, P.R., 2003. Evolution of biomass burning aerosol properties from an agricultural fire in southern Africa. Geophys. Res. Lett. 30. doi:10.1029/2003GL017342

Akagi, S.K., Yokelson, R.J., Wiedinmyer, C., Alvarado, M.J., Reid, J.S., Karl, T., Crounse, J.D., Wennberg, P.O., 2011. Emission factors for open and domestic biomass burning for use in atmospheric models. Atmos. Chem. Phys. 11, 4039–4072. doi:10.5194/acp-11-4039-2011

Alexander, B., Park, R.J., Jacob, D.J., Li, Q.B., Yantosca, R.M., Savarino, J., Lee, C.C.W., Thiemens, M.H., 2005. Sulfate formation in sea-salt aerosols: Constraints from oxygen isotopes. J. Geophys. Res. D Atmos. 110, 1–12. doi:10.1029/2004JD005659

Andreae, M.O., Merlet, P., 2001. Emission of trace gases and aerosols from biomass burning. Global Biogeochem. Cycles 15, 955–966. doi:10.1029/2000GB001382

Appel, K.W., Pouliot, G.A., Simon, H., Sarwar, G., Pye, H.O.T., Napelenok, S.L., Akhtar, F., Roselle, S.J., 2013. Evaluation of dust and trace metal estimates from the Community Multiscale Air Quality (CMAQ) model version 5.0. Geosci. Model Dev. 6, 883–899. doi:10.5194/gmd-6-883-2013

Barrett, T.E., Robinson, E.M., Usenko, S., Sheesley, R.J., 2015. Source Contributions to Wintertime Elemental and Organic Carbon in the Western Arctic Based on Radiocarbon and Tracer Apportionment. Environ. Sci. Technol. 49, 11631–11639. doi:10.1021/acs.est.5b03081

Bell, M.L., Ebisu, K., Leaderer, B.P., Gent, J.F., Lee, H.J., Koutrakis, P., Wang, Y., Dominici, F., Peng, R.D., 2013. Associations of PM2.5 Constituents and Sources with Hospital Admissions: Analysis of Four Counties in Connecticut and Massachusetts (USA) for Persons $\geqslant$ 65 Years of Age. Environ. Health Perspect. doi:10.1289/ehp.1306656

Bell, M.L., Ebisu, K., Peng, R.D., Samet, J.M., Dominici, F., 2009. Hospital Admissions and Chemical Composition of Fine Particle Air Pollution. Am. J. Respir. Crit. Care Med. 179, 1115–1120. doi:10.1164/rccm.200808-1240OC

Bell, M.L., Son, J.-Y., Peng, R.D., Wang, Y., Dominici, F., 2015. Ambient PM(2.5) and risk of hospital admissions: Do risks differ for men and women? Epidemiology 26, 575–579. doi:10.1097/EDE.0000000000000310

Bey, I., Jacob, D. J., Yantosca, R. M., Logan, J. A., Field, B. D., Fiore, A. M., Li, Q. B., Liu, H .G. Y., Mickley, L. J., and Schultz, M. G., 2001. Global modeling of tropospheric chemistry with assimilated meteorology: Model description and evaluation, J. Geophys. Res., 106, 23073–23095,doi:10.1029/2001JD000807.

Bond, T. C., Streets, D. G., Yarber, K. F., Nelson, S. M., Woo, J.-H., and Klimont, Z., 2004. A technology-based global inventory of black and organic carbon emissions from combustion, J. Geophys. Res., 109, D14203, doi:10.1029/2003JD003697.

Bond, T.C., Anderson, T.L., Campbell, D., 1999. Calibration and Intercomparison of Filter-Based Measurements of Visible Light Absorption by Aerosols. Aerosol Sci. Technol. 30, 582–600. doi:10.1080/027868299304435

Bond, T.C., Bergstrom, R.W., 2006. Light Absorption by Carbonaceous Particles: An Investigative Review. Aerosol Sci. Technol. 40, 27–67. doi:10.1080/02786820500421521

Bond, T.C., Bhardwaj, E., Dong, R., Jogani, R., Jung, S., Roden, C., Streets, D.G., Trautmann, N.M., 2007. Historical emissions of black and organic carbon aerosol from energy-related combustion, 1850-2000. Global Biogeochem. Cycles 2, doi:10.1029/2006GB002840

Bond, T.C., Doherty, S.J., Fahey, D.W., Forster, P.M., Berntsen, T., DeAngelo, B.J., Flanner, M.G., Ghan, S., Kärcher, B., Koch, D., Kinne, S., Kondo, Y., Quinn, P.K., Sarofim, M.C., Schultz, M.G., Schulz, M., Venkataraman, C., Zhang, H., Zhang, S., Bellouin, N., Guttikunda, S.K., Hopke, P.K., Jacobson, M.Z., Kaiser, J.W., Klimont, Z., Lohmann, U., Schwarz, J.P., Shindell, D., Storelvmo, T., Warren, S.G., Zender, C.S., 2013. Bounding the role of black carbon in the climate system: A scientific assessment. J. Geophys. Res. Atmos. 118, 5380–5552. doi:10.1002/jgrd.50171

Boys, B. L., Martin, R. V., van Donkelaar, A., MacDonell, R. J., Hsu, N. C., Cooper, M. J., Yantosca, R. M., Lu, Z., Streets, D. G., Zhang, Q., and Wang, S. W., 2014. Fifteen-Year Global Time Series of Satellite-Derived Fine Particulate Matter, Environ. Sci. Technol., 48, 11109–11118.

Breider, T.J., Mickley, L.J., Jacob, D.J., Ge, C., Wang, J., Payer Sulprizio, M., Croft, B., Ridley, D.A., McConnell, J.R., Sharma, S., Husain, L., Dutkiewicz, V.A., Eleftheriadis, K., Skov, H., Hopke, P.K., 2017. Multidecadal trends in aerosol radiative forcing over the Arctic: Contribution of changes in anthropogenic aerosol to Arctic warming since 1980. J. Geophys. Res. Atmos. 122, 3573–3594. doi:10.1002/2016JD025321.

Brimblecombe, P., 1979. Atmospheric arsenic. Nature 280, 104.

Brock, C.A., Cozic, J., Bahreini, R., Froyd, K.D., Middlebrook, A.M., McComiskey, A., Brioude, J., Cooper, O.R., Stohl, A., Aikin, K.C., de Gouw, J.A., Fahey, D.W., Ferrare, R.A., Gao, R.-S., Gore, W., Holloway, J.S., Hübler, G., Jefferson, A., Lack, D.A., Lance, S., Moore, R.H., Murphy, D.M., Nenes, A., Novelli, P.C., Nowak, J.B., Ogren, J.A., Peischl, J., Pierce, R.B., Pilewskie, P., Quinn, P.K., Ryerson, T.B., Schmidt, K.S., Schwarz, J.P., Sodemann, H., Spackman, J.R., Stark, H., Thomson, D.S., Thornberry, T., Veres, P., Watts, L.A., Warneke, C., Wollny, A.G., 2011. Characteristics, sources, and transport of aerosols measured in spring 2008 during the aerosol, radiation, and cloud processes affecting Arctic Climate (ARCPAC) Project. Atmos. Chem. Phys. 11, 2423–2453. doi:10.5194/acp-11-2423-2011

Chang, Y., Huang, K., Deng, C., Zou, Z., Liu, S., Zhang, Y., 2017. First long-term and near real-time measurement of atmospheric trace elements in Shanghai, China. Atmos. Chem. Phys. Discuss. 1–49. doi:10.5194/acp-2017-613.

Cheng, S., Yang, L. X., Zhou, X., Wang, Z., Zhou, Y., Gao, X., Nie, W., Wang, X., Xu, P., and Wang, W., 2011 Evaluating PM2.5 ionic components and source apportionment in Jinan, China from 2004 to 2008 using trajectory statistical methods, J. Environ. Monit., 13, 1662, 1662-1671.

Chin, M., Ginoux, P., Kinne, S., Torres, O., Holben, B.N., Duncan, B.N., Martin, R. V., Logan, J.A., Higurashi, A., Nakajima, T., Chin, M., Ginoux, P., Kinne, S., Torres, O., Holben, B.N., Duncan, B.N., Martin, R. V., Logan, J.A., Higurashi, A., Nakajima, T., 2002. Tropospheric Aerosol Optical Thickness from the GOCART Model and Comparisons with Satellite and Sun Photometer Measurements. J. Atmos. Sci. 59, 461–483. doi:10.1175/1520-0469(2002)059<0461:TAOTFT>2.0.CO;2

Cho, Y., and Youn, H., 2006. Characteristics of COMS Meteorological Imager, in: Sensors, Systems, and Next-Generation Satellites X, Proc. SPIE, Stockholm, Sweden, doi: 10.1117/12.688393, October 03.

Choi, M., Kim, J., Lee, J., Kim, M., Park, Y.-J., Holben, B., Eck, T.F., Li, Z., Song, C.H., 2018. GOCI Yonsei aerosol retrieval version 2 products: an improved algorithm and error analysis with uncertainty estimation from 5-year validation over East Asia. Atmos. Meas. Tech. 11, 385–408. doi:10.5194/amt-11-385-2018

Chow, J.C., 2002. Introduction to the A&WMA 2002 Critical Review Visibility: Science and Regulation. J. Air Waste Manage. Assoc. 52, 626–627. doi:10.1080/10473289.2002.10470812

Chýlek, P., Ramaswamy, V., Srivastava, V., 1983. Albedo of soot-contaminated snow. J. Geophys. Res. 88, 10837. doi:10.1029/JC088iC15p10837

Clarke, A.D., Noone, K.J., 1985. Soot in the Arctic snowpack: a cause for perturbations in radiative transfer. Atmos. Environ. 19, 2045–2053. doi:10.1016/0004-6981(85)90113-1

Cohen, A.J., Brauer, M., Burnett, R., Anderson, H.R., Frostad, J., Estep, K., Balakrishnan, K., Brunekreef, B., Dandona, L., Dandona, R., Feigin, V., Freedman, G., Hubbell, B., Jobling, A., Kan, H., Knibbs, L., Liu, Y., Martin, R., Morawska, L., Pope, C.A., Shin, H., Straif, K., Shaddick, G., Thomas, M., van Dingenen, R., van Donkelaar, A., Vos, T., Murray, C.J.L., Forouzanfar, M.H., 2017. Estimates and 25-year trends of the global burden of disease attributable to ambient air pollution: an analysis of data from the Global Burden of Diseases Study 2015. Lancet (London, England) 389, 1907–1918. doi:10.1016/S0140-6736(17)30505-6

Crouse, D.L., Peters, P.A., van Donkelaar, A., Goldberg, M.S., Villeneuve, P.J., Brion, O., Khan, S., Atari, D.O., Jerrett, M., Pope III, C.A., Brauer, M., Brook, J.R., Martin, R. V., Stieb, D., Burnett, R.T., 2012. Risk of nonaccidental and cardiovascular mortality in relation to long-term exposure to low concentrations of fine particulate matter : a Canadian national-level cohort study. doi:10.14288/1.0074703

Dabek-Zlotorzynska, E., Dann, T.F., Kalyani Martinelango, P., Celo, V., Brook, J.R., Mathieu, D., Ding, L., Austin, C.C., 2011. Canadian National Air Pollution Surveillance (NAPS) PM2.5 speciation program: Methodology and PM2.5 chemical composition for the years 2003–2008. Atmos. Environ. 45, 673–686. doi:10.1016/J.ATMOSENV.2010.10.024

Delene, D.J., Ogren, J.A., 2002. Variability of Aerosol Optical Properties at Four North American Surface Monitoring Sites. J. Atmos. Sci. 59, 1135–1150. doi:10.1175/1520-0469(2002)059<1135:VOAOPA>2.0.CO;2

Di, Q., Wang, Y., Zanobetti, A., Wang, Y., Koutrakis, P., Choirat, C., Dominici, F., Schwartz, J.D., 2017. Air Pollution and Mortality in the Medicare Population. N. Engl. J. Med. 376, 2513–2522. doi:10.1056/NEJMoa1702747

Doherty, S.J., Warren, S.G., Grenfell, T.C., Clarke, A.D., Brandt, R.E., 2010. Light-absorbing impurities in Arctic snow. Atmos. Chem. Phys. 10, 11647–11680. doi:10.5194/acp-10-11647-2010

Dore, A.J., Hallsworth, S., McDonald, A.G., Werner, M., Kryza, M., Abbot, J., Nemitz, E., Dore, C.J., Malcolm, H., Vieno, M., Reis, S., Fowler, D., 2014. Quantifying missing annual emission sources of heavy metals in the United Kingdom with an atmospheric transport model. Sci. Total Environ. 479–480, 171–180. doi:10.1016/j.scitotenv.2014.02.001

Drury, E., Jacob, D.J., Spurr, R.J.D., Wang, J., Shinozuka, Y., Anderson, B.E., Clarke, A.D., Dibb, J., McNaughton, C., Weber, R., 2010. Synthesis of satellite (MODIS), aircraft (ICARTT), and surface (IMPROVE, EPA-AQS, AERONET) aerosol observations over eastern North America to improve MODIS aerosol retrievals and constrain surface aerosol concentrations and sources. J. Geophys. Res. Atmos. 115. doi:10.1029/2009JD012629

Duncan Fairlie, T., Jacob, D.J., Park, R.J., 2007. The impact of transpacific transport of mineral dust in the United States. Atmos. Environ. 41, 1251–1266. doi:10.1016/j.atmosenv.2006.09.048

Eckhardt, S., Quennehen, B., Olivié, D.J.L., Berntsen, T.K., Cherian, R., Christensen, J.H., Collins, W., Crepinsek, S., Daskalakis, N., Flanner, M., Herber, A., Heyes, C., Hodnebrog, Ø., Huang, L., Kanakidou, M., Klimont, Z., Langner, J., Law, K.S., Massling, A., Myriokefalitakis, S., Nielsen, I.E., Nøjgaard, J.K., Quaas, J., Quinn, P.K., Raut, J.-C., Rumbold, S.T., Schulz, M., Skeie, R.B., Skov, H., Lund, M.T., Uttal, T., von Salzen, K., Mahmood, R., Stohl, A., 2015. Current model capabilities for simulating black carbon and sulfate concentrations in the Arctic atmosphere: a multi-model evaluation using a comprehensive measurement data set. Atmos. Chem. Phys. Discuss. 15, 10425–10477. doi:10.5194/acpd-15-10425-2015

Eleftheriadis, K., Vratolis, S., Nyeki, S., 2009. Aerosol black carbon in the European Arctic: Measurements at Zeppelin station, Ny-Ålesund, Svalbard from 1998-2007. Geophys. Res. Lett. 36, n/a-n/a. doi:10.1029/2008GL035741

Evangeliou, N., Balkanski, Y., Hao, W.M., Petkov, A., Silverstein, R.P., Corley, R., Nordgren, B.L., Urbanski, S.P., Eckhardt, S., Stohl, A., Tunved, P., Crepinsek, S., Jefferson, A., Sharma, S., Nøjgaard, J.K., Skov, H., 2016. Wildfires in northern Eurasia affect the budget of black carbon in the Arctic – a 12-year retrospective synopsis (2002–2013). Atmos. Chem. Phys. 16, 7587–7604. doi:10.5194/acp-16-7587-2016

Evans, M.J., Jacob, D.J., 2005. Impact of new laboratory studies of N 2 O 5 hydrolysis on global model budgets of tropospheric nitrogen oxides, ozone, and OH. Geophys. Res. Lett. 32, L09813. doi:10.1029/2005GL022469

Fairlie, D., T., Jacob, D. J., and Park, R. J., 2007 The impact of transpacific transport of mineral dust in the United States, Atmos. Environ., 41, 1251-1266, doi:http://dx.doi.org/10.1016/j.atmosenv.2006.09.048.

Fang, G., Chang, C., Wu, Y., Fu, P. P., Yang, C., Chen, C., and Chang, S., 2002. Ambient suspended particulate matters and related chemical species study in central Taiwan, Taichung during 1998–2001, Atmos. Environ., 36, 1921–1928

Favez, O., Cachier, H., Sciare, J. and Le Moullec, Y., 2007. Characterization and contribution to PM2.5 of semi-volatile aerosols in Paris (France), Atmos. Environ., 41(36), 7969–7976, doi:10.1016/j.atmosenv.2007.09.031.

Fischer, J. A., Jacob, D. J., Wang, Q., Bahreini, R., Carouge, C. C., Cubison, M. J., Dibb, J. E., Diehl, T., Jimenez, J. L., and Leibensperger, E. M., 2011. Sources, distribution, and acidity of sulfate–ammonium aerosol in the Arctic in winter–spring, Atmos. Environ., 45, 7301–7318.

Fisher, J.A., Jacob, D.J., Purdy, M.T., Kopacz, M., Le Sager, P., Carouge, C., Holmes, C.D., Yantosca, R.M., Batchelor, R.L., Strong, K., Diskin, G.S., Fuelberg, H.E., Holloway, J.S., Hyer, E.J., McMillan, W.W., Warner, J., Streets, D.G., Zhang, Q., Wang, Y., Wu, S., 2010. Source attribution and interannual variability of Arctic pollution in spring constrained by aircraft (ARCTAS, ARCPAC) and satellite (AIRS) observations of carbon monoxide. Atmos. Chem. Phys. 10, 977–996. doi:10.5194/acp-10-977-2010

Fisher, J.A., Jacob, D.J., Wang, Q., Bahreini, R., Carouge, C.C., Cubison, M.J., Dibb, J.E., Diehl, T., Jimenez, J.L., Leibensperger, E.M., Lu, Z., Meinders, M.B.J., Pye, H.O.T., Quinn, P.K., Sharma, S., Streets, D.G., van Donkelaar, A., Yantosca, R.M., 2011. Sources, distribution, and acidity of sulfate-ammonium aerosol in the Arctic in winter-spring. Atmos. Environ. 45, 7301–7318. doi:10.1016/j.atmosenv.2011.08.030

Flanner, M.G., 2009. Integrating anthropogenic heat flux with global climate models. Geophys. Res. Lett. 36, n/a-n/a. doi:10.1029/2008GL036465

Flanner, M.G., Zender, C.S., Randerson, J.T., Rasch, P.J., 2007. Present-day climate forcing and response from black carbon in snow. J. Geophys. Res. 112, D11202. doi:10.1029/2006JD008003

Foroutan, H., Young, J., Napelenok, S., Ran, L., Appel, K.W., Gilliam, R.C., Pleim, J.E., 2017. Development and evaluation of a physics-based windblown dust emission scheme implemented in the CMAQ modeling system. J. Adv. Model. Earth Syst. 9, 585–608. doi:10.1002/2016MS000823

Fountoukis, C., Nenes, A., 2007. ISORROPIA II: a computationally efficient thermodynamic equilibrium model for K+–Ca2+–Mg2+–NH4+–Na+–SO42−–NO3−–Cl−–H2O aerosols. Atmos. Chem. Phys. 7, 4639–4659. doi:10.5194/acp-7-4639-2007

Fu, T., Jacob, D. J., Wittrock, F., Burrows, J. P., Vrekoussis, M., and Henze, D. K., 2008. Global budgets of atmospheric glyoxal and methylglyoxal, and implications for formation of secondary organic aerosols, J. Geophys. Res., 113, D15303, doi:10.1029/2007JD009505.

Galarneau, E., Wang, D., Dabek-Zlotorzynska, E., Siu, M., Celo, V., Tardif, M., Harnish, D., Jiang, Y., 2016. Air toxics in Canada measured by the National Air Pollution Surveillance (NAPS) program and their relation to ambient air quality guidelines. J. Air Waste Manage. Assoc. 66, 184–200. doi:10.1080/10962247.2015.1096863

Galloway, J.N., Dianwu, Z., Jiling, X., Likens, G.E., 1987. Acid Rain: China, United States, and a Remote Area. Science (80-.). 236, 1559–1562.

Geng, G., Zhang, Q., Martin, R. V., van Donkelaar, A., Huo, H., Che, H., Lin, J. and He, K., 2015. Estimating long-term PM2.5 concentrations in China using satellite-based aerosol optical depth and a chemical transport model, Remote Sens. Environ., 166, 262–270, doi:10.1016/j.rse.2015.05.016.

Gentry, J.., Brock, J.., 1968. A study of the lifetime of aerosol particles. J. Colloid Interface Sci. 27, 691–701. doi:10.1016/0021-9797(68)90103-3

Giglio, L., Randerson, J.T., van der Werf, G.R., 2013. Analysis of daily, monthly, and annual burned area using the fourth-generation global fire emissions database (GFED4). J. Geophys. Res. Biogeosciences 118, 317–328. doi:10.1002/jgrg.20042

Gilardoni, S., Vignati, E., Wilson, J., 2011. Using measurements for evaluation of black carbon modeling. Atmos. Chem. Phys. 11, 439–455. doi:10.5194/acp-11-439-2011

Ginoux, P., Chin, M., Tegen, I., Prospero, J.M., Holben, B., Dubovik, O., Lin, S.-J., 2001. Sources and distributions of dust aerosols simulated with the GOCART model. J. Geophys. Res. Atmos. 106, 20255–20273. doi:10.1029/2000JD000053

Goldberg, M., 2008. A systematic review of the relation between long-term exposure to ambient air pollution and chronic diseases, Rev. Environ. Health, 23, 243, DOI: 10.1515/REVEH.2008.23.4.243.

Gong, S.L., Zhao, T.L., Sharma, S., Toom-Sauntry, D., Lavoué, D., Zhang, X.B., Leaitch, W.R., Barrie, L.A., 2010. Identification of trends and interannual variability of sulfate and black carbon in the Canadian High Arctic: 1981–2007. J. Geophys. Res. 115, D07305. doi:10.1029/2009JD012943

Guenther, A., Karl, T., Harley, P., Wiedinmyer, C., Palmer, P., and Geron, C., 2006. Estimates of global terrestrial isoprene emissions using MEGAN (Model of Emissions of Gases and Aerosols from Nature), Atmos. Chem. Phys., 6, 3181

Guenther, A.B., Jiang, X., Heald, C.L., Sakulyanontvittaya, T., Duhl, T., Emmons, L.K., Wang, X., 2012. The Model of Emissions of Gases and Aerosols from Nature version 2.1 (MEGAN2.1): an extended and updated framework for modeling biogenic emissions. Geosci. Model Dev. 5, 1471–1492. doi:10.5194/gmd-5-1471-2012

Hammer, M.S., Martin, R. V., van Donkelaar, A., Buchard, V., Torres, O., Ridley, D.A., Spurr, R.J.D., 2016. Interpreting the ultraviolet aerosol index observed with the OMI satellite instrument to understand absorption by organic aerosols: implications for atmospheric oxidation and direct radiative effects. Atmos. Chem. Phys. 16, 2507–2523. doi:10.5194/acp-16-2507-2016

Hansen, J., Nazarenko, L., 2004. Soot climate forcing via snow and ice albedos. Proc. Natl. Acad. Sci. United States Am. 101, 423–428. doi:10.1073/pnas.2237157100

Harrigan, D.L., Fuelberg, H.E., Simpson, I.J., Blake, D.R., Carmichael, G.R., Diskin, G.S., 2011. Anthropogenic emissions during Arctas-A: mean transport characteristics and regional case studies. Atmos. Chem. Phys. 11, 8677–8701. doi:10.5194/acp-11-8677-2011

He, K., Yang, F., Ma, Y., Zhang, Q., Yao, X., Chan, C. K., Cadle, S., Chan, T., and Mulawa, P. 2001. The characteristics of PM2.5 in Beijing, China, Atmos. Environ., 35, 4959, doi:http://dx.doi.org/10.1016/S1352-2310(01)00301-6.

Heald, C. L., Collett, J. L., Lee, T., Benedict, K. B., Schwandner, F. M., Li, Y., Clarisse, L., Hurtmans, D. R., Van Damme, M., Clerbaux, C., Coheur, P., Philip, S., Martin, R.V., and Pye, H. O. T., 2012. Atmospheric ammonia and particulate inorganic nitrogen over the United States., Atmos. Chem. and Phys., 12, 10295, doi:10.5194/acp-12-10295-2012.

HEI, 2016. Burden of Disease Attributable to Coal-Burning and Other Air Pollution Sources in China.

Heidam, N.Z., Christensen, J., Wåhlin, P., Skov, H., 2004. Arctic atmospheric contaminants in NE Greenland: levels, variations, origins, transport, transformations and trends 1990–2001. Sci. Total Environ. 331, 5–28. doi:10.1016/J.SCITOTENV.2004.03.033

Henze, D. K., and Seinfeld, J. H., 2012. Global secondary organic aerosol from isoprene oxidation., Geophys. Res. Lett., 33, L09812, doi:10.1029/2006GL025976

Henze, D. K., Seinfeld, J. H., Ng, N. L., Kroll, J. H., Fu, T.-M., Jacob, D. J., and Heald, C. L., 2008. Global modeling of secondary organic aerosol formation from aromatic hydrocarbons: high- vs. low-yield pathways, Atmos. Chem. Phys., 8, 2405, doi:10.5194/acp-8-2405-2008

Henze, D.K., Hakami, A., Seinfeld, J.H., 2007. Development of the adjoint of GEOS-Chem. Atmos. Chem. Phys. 7, 2413–2433. doi:10.5194/acp-7-2413-2007

Herber, A.B., Haas, C., Stone, R.S., Bottenheim, J.W., Liu, P., Li, S.-M., Staebler, R.M., Strapp, J.W., Dethloff, K., 2012. Regular airborne surveys of Arctic sea ice and atmosphere. Eos, Trans. Am. Geophys. Union 93, 41–42. doi:10.1029/2012EO040001

Holben, B., Eck, T., Slutsker, I., Tanre, D., Buis, J., Setzer, A., Vermote, E., Reagan, J., Kaufman, Y., and Nakajima, T., 1998. AERONET—A federated instrument network and data archive for aerosol characterization, Remote Sens. Environ., 66, 1-16

Holben, B., Tanre, D., Smirnov, A., Eck, T., Slutsker, I., Abuhassan, N., Newcomb, W., Schafer, J., Chatenet, B., and Lavenu, F., 2001. An emerging ground-based aerosol climatology: Aerosol optical depth from AERONET, J. of Geophys. Res. (1984–2012), 106, 12067–12097

Holben, B.N., Eck, T.F., Slutsker, I., Tanré, D., Buis, J.P., Setzer, A., Vermote, E., Reagan, J.A., Kaufman, Y.J., Nakajima, T., Lavenu, F., Jankowiak, I., Smirnov, A., 1998. AERONET—A Federated Instrument Network and Data Archive for Aerosol Characterization. Remote Sens. Environ. 66, 1–16. doi:10.1016/S0034-4257(98)00031-5

Hu, X., Waller, L. A., Al-Hamdan, M. Z., Crosson, W. L., Jr Estes, M. G., Estes, S. M., Quattrochi, D. A., Sarnat, J. A. and Liu, Y., 2013. Estimating ground-level PM2.5 concentrations in the southeastern US using geographically weighted regression, Environ. Res., 121, 1-10

Huang, L., Brook, J.R., Zhang, W., Li, S.M., Graham, L., Ernst, D., Chivulescu, A., Lu, G., 2006. Stable isotope measurements of carbon fractions (OC/EC) in airborne particulate: A new dimension for source characterization and apportionment. Atmos. Environ. 40, 2690–2705. doi:10.1016/j.atmosenv.2005.11.062

Huang, L., Gong, S.L., Sharma, S., Lavoué, D., Jia, C.Q., 2010. A trajectory analysis of atmospheric transport of black carbon aerosols to Canadian high Arctic in winter and spring (1990–2005). Atmos. Chem. Phys. 10, 5065–5073. doi:10.5194/acp-10-5065-2010.

Huang, R.-J., Cheng, R., Jing, M., Yang, L., Li, Y., Chen, Q., Chen, Y., Yan, J., Lin, C., Wu, Y., Zhang, R., El Haddad, I., Prevot, A.S.H., O'Dowd, C.D., Cao, J., 2018. Source-Specific Health Risk Analysis on Particulate Trace Elements: Coal Combustion and Traffic Emission As Major Contributors in Wintertime Beijing. Environ. Sci. Technol. doi:10.1021/acs.est.8b02091.

Hyer, E., Reid, J., and Zhang, J., 2011. An over-land aerosol optical depth data set for data assimilation by filtering, correction, and aggregation of MODIS Collection 5 optical depth retrievals, Atmos. Meas. Tech., 4, 379

Ikeda, K., Tanimoto, H., Sugita, T., Akiyoshi, H., Kanaya, Y., Zhu, C., Taketani, F., 2017. Tagged tracer simulations of black carbon in the Arctic: Transport, source contributions, and budget. Atmos. Chem. Phys. Discuss. 1–31. doi:10.5194/acp-2017-237

Jacob, D.J., Crawford, J.H., Maring, H., Clarke, A.D., Dibb, J.E., Emmons, L.K., Ferrare, R.A., Hostetler, C.A., Russell, P.B., Singh, H.B., Thompson, A.M., Shaw, G.E., McCauley, E., Pederson, J.R., Fisher, J.A., 2010. The Arctic Research of the Composition of the Troposphere from Aircraft and Satellites (ARCTAS) mission: design, execution, and first results. Atmos. Chem. Phys. 10, 5191–5212. doi:10.5194/acp-10-5191-2010

Jaeglé, L., Quinn, P. K., Bates, T. S., Alexander, B., and Lin, J.-T.: Global distribution of sea salt aerosols: new constraints from in situ and remote sensing observations, Atmos. Chem. Phys., 11, 3137, doi:10.5194/acp-11-3137-2011, 2011.

Jang, M., Czoschke, N.M., Lee, S., Kamens, R.M., 2002. Heterogeneous Atmospheric Aerosol Production by Acid-Catalyzed Particle-Phase Reactions. Science (80-.). 298, 814 LP-817.

Janssens-Maenhout, G., Crippa, M., Guizzardi, D., Dentener, F., Muntean, M., Pouliot, G., Keating, T., Zhang, Q., Kurokawa, J., Wankmüller, R., Denier van der Gon, H., Kuenen, J.J.P., Klimont, Z., Frost, G., Darras, S., Koffi, B., Li, M., 2015. HTAP_v2.2: a mosaic of regional and global emission grid maps for 2008 and 2010 to study hemispheric transport of air pollution. Atmos. Chem. Phys. 15, 11411–11432. doi:10.5194/acp-15-11411-2015

Jiang, X., Zhang, Q., Zhao, H., Geng, G., Peng, L., Guan, D., Kan, H., Huo, H., Lin, J., Brauer, M., Martin, R. V. and He, K., 2015. Revealing the hidden health costs embodied in Chinese exports, Environ. Sci. Technol., 49, 4381-4388, 10.1021/es506121s

Jimenez, J.L., Canagaratna, M.R., Donahue, N.M., Prevot, A.S.H., Zhang, Q., Kroll, J.H., DeCarlo, P.F., Allan, J.D., Coe, H., Ng, N.L., Aiken, A.C., Docherty, K.S., Ulbrich, I.M., Grieshop, A.P., Robinson, A.L., Duplissy, J., Smith, J.D., Wilson, K.R., Lanz, V.A., Hueglin, C., Sun, Y.L., Tian, J., Laaksonen, A., Raatikainen, T., Rautiainen, J., Vaattovaara, P., Ehn, M., Kulmala, M., Tomlinson, J.M., Collins, D.R., Cubison, M.J., Dunlea, J., Huffman, J.A., Onasch, T.B., Alfarra, M.R., Williams, P.I., Bower, K., Kondo, Y., Schneider, J., Drewnick, F., Borrmann, S., Weimer, S., Demerjian, K., Salcedo, D., Cottrell, L., Griffin, R., Takami, A., Miyoshi, T., Hatakeyama, S., Shimono, A., Sun, J.Y., Zhang, Y.M., Dzepina, K., Kimmel, J.R., Sueper, D., Jayne, J.T., Herndon, S.C., Trimborn, A.M., Williams, L.R., Wood, E.C., Middlebrook, A.M., Kolb, C.E., Baltensperger, U., Worsnop, D.R., 2009. Evolution of Organic Aerosols in the Atmosphere. Science (80-.). 326, 1525 LP-1529.

Kalberer, M., Paulsen, D., Sax, M., Steinbacher, M., Dommen, J., Prevot, A.S.H., Fisseha, R., Weingartner, E., Frankevich, V., Zenobi, R., Baltensperger, U., 2004. Identification of Polymers as Major Components of Atmospheric Organic Aerosols. Science (80-.). 303, 1659 LP-1662.

Kang, G., Youn, H. S., Choi, S. B., and Coste P., Radiometric calibration of COMS geostationary ocean color imager, IEEE T Geosci Remote, 6361, 636112, doi:10.1117/12.689888, 2006.

Kavouras, I.G., Etyemezian, V., Dubois, D.W., Xu, J., Pitchford, M., 2009. Source reconciliation of atmospheric dust causing visibility impairment in Class I areas of the western United States reconciliation of atmospheric dust causing visibility impairment in Class I areas of the western United States. Source J. Geophys. Res 114. doi:10.1029/2008JD009923

Khillare, P.S., Balachandran, S., Meena, B.R., 2004. Spatial and Temporal Variation of Heavy Metals in Atmospheric Aerosol of Delhi. Environ. Monit. Assess. 90, 1–21. doi:10.1023/B:EMAS.0000003555.36394.17

Khodeir, M., Shamy, M., Alghamdi, M., Zhong, M., Sun, H., Costa, M., Chen, L.-C., Maciejczyk, P., 2012a. Source apportionment and elemental composition of PM2.5 and PM10 in Jeddah City, Saudi Arabia. Atmos. Pollut. Res. 3, 331–340. doi:10.5094/APR.2012.037

Khodeir, M., Shamy, M., Alghamdi, M., Zhong, M., Sun, H., Costa, M., Chen, L.-C., Maciejczyk, P., 2012b. Source Apportionment and Elemental Composition of PM2.5 and PM10 in Jeddah City, Saudi Arabia. Atmos. Pollut. Res. 3, 331–340.

Kim, K.-H., Lee, J.-H., Jang, M.-S., 2002. Metals in airborne particulate matter from the first and second industrial complex area of Taejon city, Korea. Environ. Pollut. 118, 41–51. doi:10.1016/S0269-7491(01)00279-2

Klonecki, A., 2003. Seasonal changes in the transport of pollutants into the Arctic troposphere-model study. J. Geophys. Res. 108, 8367. doi:10.1029/2002JD002199

Kloog, I., Nordio, F., Coull, B. A., and Schwartz, J.: Incorporating local land use regression and satellite aerosol optical depth in a hybrid model of spatiotemporal PM2.5 exposures in the Mid-Atlantic states, Environ. Sci. Tech., 46, 11913–11921, 2012.

Koch, D., 2005. Distant origins of Arctic black carbon: A Goddard Institute for Space Studies ModelE experiment. J. Geophys. Res. 110, D04204. doi:10.1029/2004JD005296

Krall, J.R., Mulholland, J.A., Russell, A.G., Balachandran, S., Winquist, A., Tolbert, P.E., Waller, L.A., Sarnat, S.E., 2016. Associations between Source-Specific Fine Particulate Matter and Emergency Department Visits for Respiratory Disease in Four U.S. Cities. Environ. Health Perspect. 125. doi:10.1289/EHP271

Kuhns, H., Knipping, E.M., Vukovich, J.M., 2005. Development of a United States–Mexico Emissions Inventory for the Big Bend Regional Aerosol and Visibility Observational (BRAVO) Study. J. Air Waste Manage. Assoc. 55, 677–692. doi:10.1080/10473289.2005.10464648

Laden, F., Schwartz, J., Speizer, F. E., and Dockery, D. W., 2006. Reduction in fine particulate air pollution and mortality: extended follow-up of the Harvard Six Cities study, Am. J. Respir. Crit. Care Med., 173(6), 667-672.

Law, K.S., Stohl, A., 2007. Arctic Air Pollution: Origins and Impacts. Science (80-.). 315, 1537 LP-1540.

Law, K.S., Roiger, A., Thomas, J.L., Marelle, L., Raut, J.-C., Dalsøren, S., Fuglestvedt, J., Tuccella, P., Weinzierl, B., Schlager, H., 2017. Local Arctic air pollution: Sources and impacts. Ambio 46, 453–463. doi:10.1007/s13280-017-0962-2.

Lee, C., Martin, R. V., van Donkelaar, A., Lee, H., Dickerson, R.R., Hains, J.C., Krotkov, N., Richter, A., Vinnikov, K., Schwab, J.J., 2011. SO 2 emissions and lifetimes: Estimates from inverse modeling using in situ and global, space-based (SCIAMACHY and OMI) observations. J. Geophys. Res. 116, D06304. doi:10.1029/2010JD014758

Lee, J., Kim, J., Song, C. H., Ryu, J., Ahn, Y., and Song, C. K., 2010. Algorithm for retrieval of aerosol optical properties over the ocean from the Geostationary Ocean Color Imager, Remote Sens. Environ., 114, 1077, doi:http://dx.doi.org/10.1016/j.rse.2009.12.021.

Lee, J., Kim, J., Yang, P., and Hsu, N. C., 2012. Improvement of aerosol optical depth retrieval from MODIS spectral reflectance over the global ocean using new aerosol models archived from AERONET inversion data and tri-axial ellipsoidal dust database, Atmos. Chem. Phys., 12, 7087–7102, doi:10.5194/acp-12-7087- 2012.

Lee, K.H., Li, Z., Kim, Y.J., Kokhanovsky, A., 2009. Atmospheric Aerosol Monitoring from Satellite Observations: A History of Three Decades BT - Atmospheric and Biological Environmental Monitoring, in: Kim, Y.J., Platt, U., Gu, M.B., Iwahashi, H. (Eds.), . Springer Netherlands, Dordrecht, pp. 13–38. doi:10.1007/978-1-4020-9674-7_2.

Lee, R.E., Von Lehmden, D.J., 1973. Trace Metal Pollution in the Environment. J. air Pollut. Control Assoc. 23, 853–837.

Lelieveld, J., Evans, J.S., Fnais, M., Giannadaki, D., Pozzer, A., 2015. The contribution of outdoor air pollution sources to premature mortality on a global scale. Nature 525, 367–371. doi:10.1038/nature15371

Li, C., Hu, Y., Zhang, F., Chen, J., Ma, Z., Ye, X., Yang, X., Wang, L., Tang, X., Zhang, R., Mu, M., Wang, G., Kan, H., Wang, X., Mellouki, A., 2017. Multi-pollutant emissions from the burning of major agricultural residues in China and the related health-economic effects. Atmos. Chem. Phys 17, 4957–4988. doi:10.5194/acp-17-4957-2017

Li, M., Zhang, Q., Kurokawa, J., Woo, J.-H., He, K.B., Lu, Z., Ohara, T., Song, Y., Streets, D.G., Carmichael, G.R., Cheng, Y.F., Hong, C.P., Huo, H., Jiang, X.J., Kang, S.C., Liu, F., Su, H., Zheng, B., 2015. MIX: a mosaic Asian anthropogenic emission inventory for the MICS-Asia and the HTAP projects. Atmos. Chem. Phys. Discuss. 15, 34813–34869. doi:10.5194/acpd-15-34813-2015.

Liao, H., Henze, D. K., Seinfeld, J. H., Wu, S., and Mickley, L. J., 2007. Biogenic secondary organic aerosol over the United States: Comparison of climatological simulations with observations, J. Geophys. Res., 112, D06201, doi:10.1029/2006JD007813.

Lim, S. S., Vos, T., Flaxman, A. D., Danaei, G., Shibuya, K., Adair-Rohani, H., AlMazroa, M. A., Amann, M., Anderson, H. R., Andrews, K. G., Aryee, M., Atkinson, C., Bacchus, L. J., Bahalim, A. N., Balakrishnan, K., Balmes, J., Barker-Collo, S., Baxter, A., Bell, M. L., Blore, J. D., Blyth, F., Bonner, C., Borges, G., Bourne, R., Boussinesq, M., Brauer, M., Brooks, P., Bruce, N. G., Brunekreef, B., Bryan-Hancock, C., Bucello, C., Buchbinder, R., Bull, F., Burnett, R. T., Byers, T. E., Calabria, B., Carapetis, J., Carnahan, E., Chafe, Z., Charlson, F., Chen, H., Chen, J. S., Cheng, A. T., Child, J. C., Cohen, A., Colson, K. E., Cowie, B. C., Darby, S., Darling, S., Davis, A., Degenhardt, L., Dentener, F., Des Jarlais, D. C., Devries, K., Dherani, M., Ding, E. L., Dorsey, E. R., Driscoll, T., Edmond, K., Ali, S. E., Engell, R. E., Erwin, P. J., Fahimi, S., Falder, G., Farzadfar, F., Ferrari, A., Finucane, M. M., Flaxman, S., Fowkes, F. G. R., Freedman, G., Freeman, M. K., Gakidou, E., Ghosh, S., Giovannucci, E., Gmel, G., Graham, K., Grainger, R., Grant, B., Gunnell, D., Gutierrez, H. R., Hall, W., Hoek, H. W., Hogan, A., Hosgood III, H. D., Hoy, D., Hu, H., Hubbell, B. J., Hutchings, S. J., Ibeanusi, S. E., Jacklyn, G. L., Jasrasaria, R., Jonas, J. B., Kan, H., Kanis, J. A., Kassebaum, N., Kawakami, N., Khang, Y., Khatibzadeh, S., Khoo, J., Kok, C., Laden, F., Lalloo, R., Lan, Q., Lathlean, T., Leasher, J. L., Leigh, J., Li, Y., Lin, J. K., Lipshultz, S. E.,

London, S., Lozano, R., Lu, Y., Mak, J., Malekzadeh, R., Mallinger, L., Marcenes, W., March, L., Marks, R., Martin, R., McGale, P., McGrath, J., Mehta, S., Memish, Z. A., Mensah, G. A., Merriman, T. R., Micha, R., Michaud, C., Mishra, V., Hanafiah, K. M., Mokdad, A. A., Morawska, L., Mozaffarian, D., Murphy, T., Naghavi, M., Neal, B., Nelson, P. K., Nolla, J. M., Norman, R., Olives, C., Omer, S. B., Orchard, J., Osborne, R., Ostro, B., Page, A., Pandey, K. D., Parry, C. D., Passmore, E., Patra, J., Pearce, N., Pelizzari, P. M., Petzold, M., Phillips, M. R., Pope, D., Pope III, C. A., Powles, J., Rao, M., Razavi, H., Rehfuess, E. A., Rehm, J. T., Ritz, B., Rivara, F. P., Roberts, T., Robinson, C., Rodriguez-Portales, J. A., Romieu, I., Room, R., Rosenfeld, L. C., Roy, A., Rushton, L., Salomon, J. A., Sampson, U., Sanchez-Riera, L., Sanman, E., Sapkota, A., Seedat, S., Shi, P., Shield, K., Shivakoti, R., Singh, G. M., Sleet, D. A., Smith, E., Smith, K. R., Stapelberg, N. J., Steenland, K., Stöckl, H., Stovner, L. J., Straif, K., Straney, L., Thurston, G. D., Tran, J. H., Van Dingenen, R., van Donkelaar, A., Veerman, J. L., Vijayakumar, L., Weintraub, R., Weissman, M. M., White, R. A., Whiteford, H., Wiersma, S. T., Wilkinson, J. D., Williams, H. C., Williams, W., Wilson, N., Woolf, A. D., Yip, P., Zielinski, J. M., Lopez, A. D., Murray, C. J. and Ezzati, M.: A comparative risk assessment of burden of disease and injury attributable to 67 risk factors and risk factor clusters in 21 regions, 1990–2010: a systematic analysis for the Global Burden of Disease Study 2010, The Lancet, 380, 2224-2260, http://dx.doi.org/10.1016/S0140-6736(12)61766-8.

Lippmann, M., 2014. Toxicological and epidemiological studies of cardiovascular effects of ambient air fine particulate matter (PM 2.5) and its chemical components: Coherence and public health implications. Crit. Rev. Toxicol. 44, 299–347. doi:10.3109/10408444.2013.861796

Liu, D., Quennehen, B., Darbyshire, E., Allan, J.D., Williams, P.I., Taylor, J.W., Bauguitte, S.J.-B., Flynn, M.J., Lowe, D., Gallagher, M.W., Bower, K.N., Choularton, T.W., Coe, H., 2015. The importance of Asia as a source of black carbon to the European Arctic during springtime 2013. Atmos. Chem. Phys. 15, 11537–11555. doi:10.5194/acp-15-11537-2015

Liu, H., Jacob, D.J., Bey, I., Yantosca, R.M., 2001. Constraints from 210 Pb and 7 Be on wet deposition and transport in a global three-dimensional chemical tracer model driven by assimilated meteorological fields. J. Geophys. Res. Atmos. 106, 12109–12128. doi:10.1029/2000JD900839

Liu, J., Fan, S., Horowitz, L.W., Levy, H., 2011. Evaluation of factors controlling long-range transport of black carbon to the Arctic. J. Geophys. Res. 116, D04307. doi:10.1029/2010JD015145

Liu, Y., Paciorek, C. J., and Koutrakis, P., 2009. Estimating regional spatial and temporal variability of PM2.5 concentrations using satellite data, meteorology, and land use information, Environ. Health Perspect., 117, 886–892.

Liu, Y., Park, R. J., Jacob, D. J., Li, Q., Kilaru, V., and Sarnat, J. A., 2004. Mapping annual mean ground‐level PM2.5 concentrations using Multiangle Imaging Spectroradiometer aerosol optical thickness over the contiguous United States, J. Geophys. Res. (1984–2012), 109, D22206, DOI: 10.1029/2004JD005025.

Lohmann, U., Feichter, J., 2005. Global indirect aerosol effects: a review. Atmos. Chem. Phys. 5, 715–737. doi:10.5194/acp-5-715-2005

M., P.J., Paul, G., Omar, T., E., N.S., E., G.T., 2002. ENVIRONMENTAL CHARACTERIZATION OF GLOBAL SOURCES OF ATMOSPHERIC SOIL DUST IDENTIFIED WITH THE NIMBUS 7 TOTAL OZONE MAPPING SPECTROMETER (TOMS) ABSORBING AEROSOL PRODUCT. Rev. Geophys. 40, 2–31. doi:10.1029/2000RG000095

Ma, P.-L., Rasch, P.J., Wang, H., Zhang, K., Easter, R.C., Tilmes, S., Fast, J.D., Liu, X., Yoon, J.-H., Lamarque, J.-F., 2013. The role of circulation features on black carbon transport into the Arctic in the Community Atmosphere Model version 5 (CAM5). J. Geophys. Res. Atmos. 118, 4657–4669. doi:10.1002/jgrd.50411

Ma, Z., Hu, X., Huang, L., Bi, J., and Liu, Y., 2014. Estimating ground-level PM2.5 in China using satellite remote sensing, Environ. Sci. Tech., 48, 7436–7444.

Malm, W.C., Schichtel, B.A., Pitchford, M.L., 2011. Uncertainties in PM2.5 gravimetric and speciation measurements and what we can learn from them. J. Air Waste Manag. Assoc. 61, 1131–49.

Malm, W.C., Sisler, J.F., Huffman, D., Eldred, R.A., Cahill, T.A., 1994. Spatial and seasonal trends in particle concentration and optical extinction in the United States. J. Geophys. Res. 99, 1347. doi:10.1029/93JD02916

Marais, E.A., Jacob, D.J., Jimenez, J.L., Campuzano-Jost, P., Day, D.A., Hu, W., Krechmer, J., Zhu, L., Kim, P.S., Miller, C.C., Fisher, J.A., Travis, K., Yu, K., Hanisco, T.F., Wolfe, G.M., Arkinson, H.L., Pye, H.O.T., Froyd, K.D., Liao, J., McNeill, V.F., 2016. Aqueous-phase mechanism for secondary organic aerosol formation from isoprene: Application to the southeast United States and co-benefit of SO2 emission controls. Atmos. Chem. Phys. 16, 1603–1618. doi:10.5194/acp-16-1603-2016

Martin, R. V., Jacob, D. J., Yantosca, R. M., Chin, M., and Ginoux, P., 2003. Global and regional decreases in tropospheric oxidants from photochemical effects of aerosols, J. Geophys. Res., 108(D3), 4097, doi:10.1029/2002JD002622.

Ministry of Environmental Protection of the People's Republic of China: Chinese National Ambient Air Quality Standard, CNAAQS, GB3095-2012, Beijing, 2012.

Mu, M., Randerson, J., Van der Werf, G., Giglio, L., Kasibhatla, P., Morton, D., Collatz, G., DeFries, R., Hyer, E., and Prins, E., 2011. Daily and 3-hourly variability in global fire emissions and consequences for atmospheric model predictions of carbon monoxide, J. Geophys. Res. (1984–2012), 116, D24303, 1-19.

Mungall, E.L., Croft, B., Lizotte, M., Thomas, J.L., Murphy, J.G., Levasseur, M., Martin, R. V., Wentzell, J.J.B., Liggio, J., Abbatt, J.P.D., 2015. Summertime sources of dimethyl sulfide in the Canadian Arctic Archipelago and Baffin Bay. Atmos. Chem. Phys. Discuss. 15, 35547–35589. doi:10.5194/acpd-15-35547-2015

Murray, L. T., Jacob, D. J., Logan, J. A., Hudman, R. C., and Koshak, W. J., 2012. Optimized regional and interannual variability of lightning in a global chemical transport model constrained by LIS/OTD satellite data, J. Geophys. Res. (1984–2012), 117, D20307, DOI: 10.1029/2012JD017934.

Nagajyoti, P.C., Lee, K.D., Sreekanth, T.V.M., 2010. Heavy metals, occurrence and toxicity for plants: a review. Environ. Chem. Lett. 8, 199–216. doi:10.1007/s10311-010-0297-8

Namazi, M., von Salzen, K., Cole, J.N.S., 2015. Simulation of black carbon in snow and its climate impact in the Canadian Global Climate Model. Atmos. Chem. Phys. 15, 10887–10904. doi:10.5194/acp-15-10887-2015

NOAA, 2017. Arctic Report Card: Update for 2017.

Nriagu, J.O., Pacyna, J.M., 1988. Quantitative assessment of worldwide contamination of air, water and soils by trace metals. Nature 333, 134.

Ohara, T., Akimoto, H., Kurokawa, J., Horii, N., Yamaji, K., Yan, X. and Hayasaka, T.: An Asian emission inventory of anthropogenic emission sources for the period 1980–2020, Atmos. Chem. Phys., 7, 4419, 2007.

Okuda, T., Nakao, S., Katsuno, M., Tanaka, S., 2007. Source identification of nickel in TSP and PM2.5 in Tokyo, Japan. Atmos. Environ. 41, 7642–7648. doi:10.1016/J.ATMOSENV.2007.08.050

Olivier, J. G. J., and Berdowski, J. J. M., 2001. Global emissions sources and sinks, in: The Climate System, Berdowski, J., Guicherit, R., and Heij, B.J. (Ed.), A.A. Balkema Publishers/Swets & Zeitlinger Publishers, Lisse, The Netherlands, 33-78.

Ostro, B., Feng, W.-Y., Broadwin, R., Green, S., Lipsett, M., 2007. The effects of components of fine particulate air pollution on mortality in california: results from CALFINE. Environ. Health Perspect. 115, 13–9. doi:10.1289/ehp.9281

Pachon, J.E., Weber, R.J., Zhang, X., Mulholland, J.A., Russell, A.G., 2013. Revising the use of potassium (K) in the source apportionment of PM2.5. Atmos. Pollut. Res. 4, 14–21. doi:10.5094/APR.2013.002

Pacyna, J.M., Pacyna, E.G., 2001. An assessment of global and regional emissions of trace metals to the atmosphere from anthropogenic sources worldwide. Environ. Rev. 9, 269–298. doi:10.1139/a01-012

Pakkanen, T.A., Loukkola, K., Korhonen, C.H., Aurela, M., Mäkelä, T., Hillamo, R.E., Aarnio, P., Koskentalo, T., Kousa, A., Maenhaut, W., 2001. Sources and chemical composition of atmospheric fine and coarse particles in the Helsinki area. Atmos. Environ. 35, 5381–5391. doi:10.1016/S1352-2310(01)00307-7

Park, M., Song, C., Park, R., Lee, J., Kim, J., Lee, S., Woo, J., Carmichael, G., Eck, T. F., and Holben, B. N., 2014. New approach to monitor transboundary particulate pollution over Northeast Asia, Atmos. Chem. Phys., 14, 659.

Park, R. J., Jacob, D. J., Chin M., and Martin, R. V., 2003. Sources of carbonaceous aerosols over the United States and implications for natural visibility, J. Geophys. Res, 108, 4355, doi:10.1029/2002JD003190.

Park, R. J., Jacob, D. J., Field, B. D., Yantosca, R. M., and Chin, M., 2004. Natural and transboundary pollution influences on sulfate-nitrate-ammonium aerosols in the United States: implications for policy, J. Geophys. Res., 109, D15204, doi:10.1029/2003JD004473.

Park, R.J., 2005. Export efficiency of black carbon aerosol in continental outflow: Global implications. J. Geophys. Res. 110, D11205. doi:10.1029/2004JD005432

Park, R.J., Jacob, D.J., Chin, M., Martin, R. V, 2003. Sources of carbonaceous aerosols over the United States and implications for natural visibility. J. Geophys. Res. Atmos. 108, 4355. doi:10.1029/2002JD003190

Park, R.J., Jacob, D.J., Field, B.D., Yantosca, R.M., Chin, M., 2004. Natural and transboundary pollution influences on sulfate-nitrate-ammonium aerosols in the United States: Implications for policy. J. Geophys. Res. 109, D15204. doi:10.1029/2003JD004473

Pasceri, R.E., Friedlander, S.K., 1965. Measurements of the Particle Size Distribution of the Atmospheric Aerosol: II. Experimental Results and Discussion. J. Atmos. Sci. 22, 577–584. doi:10.1175/1520-0469(1965)022<0577:MOTPSD>2.0.CO;2

Petzold, A., Ogren, J.A., Fiebig, M., Laj, P., Li, S.-M., Baltensperger, U., Holzer-Popp, T., Kinne, S., Pappalardo, G., Sugimoto, N., Wehrli, C., Wiedensohler, A., Zhang, X.-Y., 2013. Recommendations for reporting “black carbon” measurements. Atmos. Chem. Phys. 13, 8365–8379. doi:10.5194/acp-13-8365-2013

Philip, S., Martin, R. V., Keller, C.A., 2016. Sensitivity of chemistry-transport model simulations to the duration of chemical and transport operators: a case study with GEOS-Chem v10-01. Geosci. Model Dev. 9, 1683–1695. doi:10.5194/gmd-9-1683-2016

Philip, S., Martin, R. V., Pierce, J. R., Jimenez, J. L., Zhang, Q., Canagaratna, M. R., Spracklen, D. V., Nowlan, C. R., Lamsal, L. N., Cooper, M. J., and Krotkov, N. A., 2014. Spatially and seasonally resolved estimate of the ratio of global organic matter to organic carbon, Atmos. Environ., 87, 34, DOI: 10.1016/j.atmosenv.2013.11.065.

Pye, H. O. T., Liao, H., Wu, S., Mickley, L. J., Jacob, D. J., Henze, D. K., and Seinfeld, J. H., 2009. Effect of changes in climate and emissions on future sulfate-nitrate-ammonium aerosol levels in the United States, J. Geophys. Res., 114, D01205, doi:10.1029/2008JD010701.

Pye, H.O.T., Chan, A.W.H., Barkley, M.P., Seinfeld, J.H., 2010. Global modeling of organic aerosol: the importance of reactive nitrogen (NO_x and NO₃). Atmos. Chem. Phys. 10, 11261–11276. doi:10.5194/acp-10-11261-2010

Qi, L., Li, Q., Li, Y., He, C., 2016. Factors Controlling Black Carbon Distribution in the Arctic. Atmos. Chem. Phys. Discuss. 1–39. doi:10.5194/acp-2016-707

Qi, L., Li, Q., Henze, D.K., Tseng, H.-L., He, C., 2017. Sources of Springtime Surface Black Carbon in the Arctic: An Adjoint Analysis. Atmos. Chem. Phys. Discuss. 1–32. doi:10.5194/acp-2016-1112

Quinn, P.K., Bates, T.S., Baum, E., Doubleday, N., Fiore, A.M., Flanner, M., Fridlind, A., Garrett, T.J., Koch, D., Menon, S., Shindell, D., Stohl, A., Warren, S.G., 2008. Short-lived pollutants in the Arctic: their climate impact and possible mitigation strategies. Atmos. Chem. Phys. 8, 1723–1735. doi:10.5194/acp-8-1723-2008

Ramabhadran, T.E., Peterson, T.W., Seinfeld, J.H., 1976. Dynamics of aerosol coagulation and condensation. AIChE J. 22, 840–851. doi:10.1002/aic.690220505

Ramanathan, V., Carmichael, G., 2008. Global and regional climate changes due to black carbon. Nat. Geosci 1, 221–227.

RANDERSON, J.T., VAN DER WERF, G.R., GIGLIO, L., COLLATZ, G.J., KASIBHATLA, P.S., 2015. Global Fire Emissions Database, Version 4, (GFEDv4). doi:10.3334/ornldaac/1293

Reff, A., Bhave, P. V, Simon, H., Pace, T.G., Pouliot, G.A., Mobley, J.D., Houyoux, M., 2009. Emissions Inventory of PM2.5 Trace Elements across the United States. Environ. Sci. Technol. 43, 5790–5796. doi:10.1021/es802930x

Ridley, D. A., Heald, C. L., and Ford, B., 2012. North African dust export and deposition: A satellite and model perspective., J. Geophys. Res., 117, D02202, doi:10.1029/2011JD016794.

RTI, 2009. Standard Operating Procedure for the X-Ray Fluorescence Analysis of Particulate Matter Deposits on Teflon Filters.

Salter, M.E., Hamacher-Barth, E., Leck, C., Werner, J., Johnson, C.M., Riipinen, I., Nilsson, E.D., Zieger, P., n.d. Geophysical Research Letters Calcium enrichment in sea spray aerosol particles. doi:10.1002/2016GL070275

Samset, B.H., Myhre, G., 2015. Climate response to externally mixed black carbon as a function of altitude. J. Geophys. Res. Atmos. 120, 2913–2927. doi:10.1002/2014JD022849

Sand, M., Berntsen, T.K., Seland, Ø., Kristjánsson, J.E., 2013. Arctic surface temperature change to emissions of black carbon within Arctic or midlatitudes. J. Geophys. Res. Atmos. 118, 7788–7798. doi:10.1002/jgrd.50613

Sand, M., Berntsen, T.K., von Salzen, K., Flanner, M.G., Langner, J., Victor, D.G., 2016. Response of Arctic temperature to changes in emissions of short-lived climate forcers. Nat. Clim. Chang. 6, 286–289.

Schroth, A.W., Crusius, J., Sholkovitz, E.R., Bostick, B.C., 2009. Iron solubility driven by speciation in dust sources to the ocean. Nat. Geosci. 2, 337–340. doi:10.1038/ngeo501

Seinfeld, J.H., Ramabhadran, T.E., 1975. Atmospheric aerosol growth by heterogeneous condensation. Atmos. Environ. 9, 1091–1097. doi:10.1016/0004-6981(75)90184-5

Sharma, S., Andrews, E., Barrie, L.A., Ogren, J.A., Lavoué, D., 2006. Variations and sources of the equivalent black carbon in the high Arctic revealed by long-term observations at Alert and Barrow: 1989–2003. J. Geophys. Res. 111, D14208. doi:10.1029/2005JD006581

Sharma, S., Ishizawa, M., Chan, D., Lavoué, D., Andrews, E., Eleftheriadis, K., Maksyutov, S., 2013. 16-year simulation of Arctic black carbon: Transport, source contribution, and sensitivity analysis on deposition. J. Geophys. Res. Atmos. 118, 943–964. doi:10.1029/2012JD017774

Sharma, S., Leaitch, W.R., Huang, L., Veber, D., Kolonjari, F., Zhang, W., Hanna, S.J., Bertram, A.K., Ogren, J.A., 2017. An Evaluation of three methods for measuring black carbon at Alert, Canada. Atmos. Chem. Phys. Discuss. 1–42. doi:10.5194/acp-2017-339

Shaw, G.E., Stamnes, K., 1980. ARCTIC HAZE: PERTURBATION OF THE POLAR RADIATION BUDGET*. Ann. N. Y. Acad. Sci. 338, 533–539. doi:10.1111/j.1749-6632.1980.tb17145.x

Shindell, D., Faluvegi, G., 2009. Climate response to regional radiative forcing during the twentieth century. Nat. Geosci 2, 294–300.

Shindell, D.T., Chin, M., Dentener, F., Doherty, R.M., Faluvegi, G., Fiore, a M., Hess, P., Koch, D.M., MacKenzie, I. a., Sanderson, M.G., Schultz, M.G., Schulz, M., Stevenson, D.S., Teich, H., Textor, C., O.Wild, Bergmann, D.J., Bey, I., Bian, H., Cuvelier, C., Duncan, B.N., Folberth, G., Horowitz, L.W., Jonson, J., Kaminski, J.W., Marmer, E., Park, R., Pringle, K.J., Schroeder, S., Szopa, S., Takemura, T., Zeng, G., Keating, T.J., Zuber, a., 2008. A multi-model assessment of pollution transport to the Arctic. Atmopsheric Chem. Phys. 8, 5353–5372. doi:10.5194/acp-8-5353-2008

Silva, R. A., West, J. J., Zhang, Y., Anenberg, S. C., Lamarque, J., Shindell, D. T., Collins, W. J., Dalsoren, S., Faluvegi, G., and Folberth, G., 2013. Global premature mortality due to

anthropogenic outdoor air pollution and the contribution of past climate change, Environ. Res. Lett., 8, 034005, doi:10.1088/1748-9326/8/3/034005.

Smirnov, A., Holben, B., Eck, T., Dubovik, O., and Slutsker, I., 2000. Cloud-screening and quality control algorithms for the AERONET database, Remote Sens. Environ., 73, 337–349.

Snider, G., Weagle, C. L., Martin, R. V., van Donkelaar, A., Conrad, K., Cunningham, D., Gordon, C., Zwicker, M., Akoshile, C., Artaxo, P., Anh, N. X., Brook, J., Dong, J., Garland, R. M., Greenwald, R., Griffith, D., He, K., Holben, B. N., Kahn, R., Koren, I., Lagrosas, N., Lestari, P., Ma, Z., Vanderlei Martins, J., Quel, E. J., Rudich, Y., Salam, A., Tripathi, S. N., Yu, C., Zhang, Q., Zhang, Y., Brauer, M., Cohen, A., Gibson, M. D., and Liu, Y., 2015. SPARTAN: A Global Network to Evaluate and Enhance Satellite-Based Estimates of Ground-level Particulate Matter for Global Health Applications, Atmos. Meas. Tech., 8, 505.

Snider, G., Weagle, C.L., Murdymootoo, K.K., Ring, A., Ritchie, Y., Stone, E., Walsh, A., Akoshile, C., Anh, N.X., Balasubramanian, R., Brook, J., Qonitan, F.D., Dong, J., Griffith, D., He, K., Holben, B.N., Kahn, R., Lagrosas, N., Lestari, P., Ma, Z., Misra, A., Norford, L.K., Quel, E.J., Salam, A., Schichtel, B., Segev, L., Tripathi, S., Wang, C., Yu, C., Zhang, Q., Zhang, Y., Brauer, M., Cohen, A., Gibson, M.D., Liu, Y., Martins, J.V., Rudich, Y., Martin, R. V., 2016. Variation in global chemical composition of PM_{2.5}: emerging results from SPARTAN. Atmos. Chem. Phys. 16, 9629–9653. doi:10.5194/acp-16-9629-2016

Solomon, P.A., Crumpler, D., Flanagan, J.B., Jayanty, R.K.M., Rickman, E.E., McDade, C.E., 2014. U.S. National PM 2.5 Chemical Speciation Monitoring Networks—CSN and IMPROVE: Description of networks. J. Air Waste Manage. Assoc. 64, 1410–1438. doi:10.1080/10962247.2014.956904

Stettler, M. E. J., Eastham, S., and Barrett, S. R. H., 2011. Air quality and public health impacts of UK airports. Part I: Emissions, Atmos. Environ., 45, 5415–5424.

Stohl, A., 2006. Characteristics of atmospheric transport into the Arctic troposphere. J. Geophys. Res. 111, D11306. doi:10.1029/2005JD006888

Stohl, A., Andrews, E., Burkhart, J.F., Forster, C., Herber, A., Hoch, S.W., Kowal, D., Lunder, C., Mefford, T., Ogren, J.A., Sharma, S., Spichtinger, N., Stebel, K., Stone, R., Ström, J., Tørseth, K., Wehrli, C., Yttri, K.E., 2006. Pan-Arctic enhancements of light absorbing

aerosol concentrations due to North American boreal forest fires during summer 2004. J. Geophys. Res. 111, D22214. doi:10.1029/2006JD007216

Stohl, A., Berg, T., Burkhart, J.F., Fjæraa, A.M., Forster, C., Herber, A., Hov, Ø., Lunder, C., McMillan, W.W., Oltmans, S., Shiobara, M., Simpson, D., Solberg, S., Stebel, K., Ström, J., Tørseth, K., Treffeisen, R., Virkkunen, K., Yttri, K.E., 2007. Arctic smoke – record high air pollution levels in the European Arctic due to agricultural fires in Eastern Europe in spring 2006. Atmos. Chem. Phys. 7, 511–534. doi:10.5194/acp-7-511-2007

Stohl, A., Klimont, Z., Eckhardt, S., Kupiainen, K., Shevchenko, V.P., Kopeikin, V.M., Novigatsky, A.N., 2013. Black carbon in the Arctic: the underestimated role of gas flaring and residential combustion emissions. Atmos. Chem. Phys. 13, 8833–8855. doi:10.5194/acp-13-8833-2013

Stone, R.S., Herber, A., Vitale, V., Mazzola, M., Lupi, A., Schnell, R.C., Dutton, E.G., Liu, P.S.K., Li, S.-M., Dethloff, K., Lampert, A., Ritter, C., Stock, M., Neuber, R., Maturilli, M., 2010. A three-dimensional characterization of Arctic aerosols from airborne Sun photometer observations: PAM-ARCMIP, April 2009. J. Geophys. Res. 115, D13203. doi:10.1029/2009JD013605

Streets, D.G., Bond, T.C., Lee, T., Jang, C., 2004. On the future of carbonaceous aerosol emissions. J. Geophys. Res. 109, D24212. doi:10.1029/2004JD004902

T. Burnett, R., Brook, J., Dann, T., Delocla, C., Philips, O., Cakmak, S., Vincent, R., S. Goldberg, M., Krewski, D., 2000. ASSOCIATION BETWEEN PARTICULATE- AND GAS-PHASE COMPONENTS OF URBAN AIR POLLUTION AND DAILY MORTALITY IN EIGHT CANADIAN CITIES. Inhal. Toxicol. 12, 15–39. doi:10.1080/08958370050164851

Tanner, R.L., Parkhurst, W.J., Valente, M.L., Lynn Humes, K., Jones, K., Gilbert, J., 2001. Impact of the 1998 Central American fires on PM2.5 mass and composition in the southeastern United States. Atmos. Environ. 35, 6539–6547. doi:10.1016/S1352-2310(01)00275-8

Tao, J., Shen, Z., Zhu, C., Yue, J., Cao, J., Liu, S., Zhu, L., and Zhang, R., 2012. Seasonal variations and chemical characteristics of sub-micrometer particles (PM1) in Guangzhou, China, Atmos. Res., 115, 222–231, doi:10.1016/j.atmosres.2012.06.025.

Thomaidis, N.S., Bakeas, E.B., Siskos, P.A., 2003. Characterization of lead, cadmium, arsenic and nickel in PM2.5 particles in the Athens atmosphere, Greece. Chemosphere 52, 959–966. doi:10.1016/S0045-6535(03)00295-9

Tobler, W, Deichmann, U., Gottsegen, J., and Maloy, K., 1997. World population in a grid of spherical quadrilaterals, Int. J. Popul. Geogr., 3, 203–225.

Toossi, R., Novakov, T., 1985. The lifetime of aerosols in ambient air: Consideration of the effects of surfactants and chemical reactions. Atmos. Environ. 19, 127–133. doi:10.1016/0004-6981(85)90143-X

Tørseth, K., Aas, W., Breivik, K., Fjæraa, A.M., Fiebig, M., Hjellbrekke, A.G., Lund Myhre, C., Solberg, S., Yttri, K.E., 2012. Introduction to the European Monitoring and Evaluation Programme (EMEP) and observed atmospheric composition change during 1972–2009. Atmos. Chem. Phys. 12, 5447–5481. doi:10.5194/acp-12-5447-2012

Travis, K.R., Jacob, D.J., Fisher, J.A., Kim, P.S., Marais, E.A., Zhu, L., Yu, K., Miller, C.C., Yantosca, R.M., Sulprizio, M.P., Thompson, A.M., Wennberg, P.O., Crounse, J.D., St. Clair, J.M., Cohen, R.C., Laughner, J.L., Dibb, J.E., Hall, S.R., Ullmann, K., Wolfe, G.M., Pollack, I.B., Peischl, J., Neuman, J.A., Zhou, X., 2016. Why do models overestimate surface ozone in the Southeast United States? Atmos. Chem. Phys. 16, 13561–13577. doi:10.5194/acp-16-13561-2016

Tuomisto, J.T., Wilson, A., Evans, J.S., Tainio, M., 2008. Uncertainty in mortality response to airborne fine particulate matter: Combining European air pollution experts. Reliab. Eng. Syst. Saf. 93, 732–744. doi:10.1016/J.RESS.2007.03.002

van Donkelaar, A., Martin, R. V., and Park, R. J., 2006. Estimating ground‐level PM2. 5 using aerosol optical depth determined from satellite remote sensing, J. Geophys. Res (1984‐2012), 111, D21201, DOI: 10.1029/2005JD006996.

van Donkelaar, A., Martin, R. V., Brauer, M., and Boys, B. L., 2015. Use of Satellite Observations for Long-Term Exposure Assessment of Global Concentrations of Fine Particulate Matter, Environ. Health Perspect., 123, DOI:10.1289/ehp.1408646.

van Donkelaar, A., Martin, R. V., Brauer, M., Hsu, N.C., Kahn, R.A., Levy, R.C., Lyapustin, A., Sayer, A.M., Winker, D.M., 2016. Global Estimates of Fine Particulate Matter using a Combined Geophysical-Statistical Method with Information from Satellites, Models, and Monitors. Environ. Sci. Technol. 50, 3762–3772. doi:10.1021/acs.est.5b05833

van Donkelaar, A., Martin, R. V., Brauer, M., Kahn, R., Levy, R., Verduzco, C., and Villeneuve, P. J., 2010. Global estimates of ambient fine particulate matter concentrations from satellite-based aerosol optical depth: development and application, Environ. Health Perspect., 118, 847, doi:10.1289/ehp.0901623.

Venter, A.D., Van Zyl, P.G., Beukes, J.P., Josipovic, M., Hendriks, J., Vakkari, V., Laakso, L., 2017. Atmospheric trace metals measured at a regional background site (Welgegund) in South Africa. Atmos. Chem. Phys 17, 4251–4263. doi:10.5194/acp-17-4251-2017

Vermette, S.J., Peden, M.E., Willoughby, T.C., Lindberg, S.E., Weiss, A.D., 1995. Methodology for the sampling of metals in precipitation: Results of the national atmospheric deposition program (NADP) pilot network. Atmos. Environ. 29, 1221–1229. doi:10.1016/1352-2310(94)00207-2

Wai, K.-M., Wu, S., Li, X., Jaffe, D.A., Perry, K.D., 2016. Global Atmospheric Transport and Source-Receptor Relationships for Arsenic. Environ. Sci. Technol. 50, 3714–3720. doi:10.1021/acs.est.5b05549

Walker, J. M., Philip, S., Martin, R. V., and Seinfeld, J. H., 2012. Simulation of nitrate, sulfate, and ammonium aerosols over the United States., Atmos. Chem. and Phys., 12, 11213, doi:10.5194/acp-12-11213-2012.

Wang, H., Rasch, P.J., Easter, R.C., Singh, B., Zhang, R., Ma, P.-L., Qian, Y., Ghan, S.J., Beagley, N., 2014. Using an explicit emission tagging method in global modeling of source-receptor relationships for black carbon in the Arctic: Variations, sources, and transport pathways. J. Geophys. Res. Atmos. 119, 12,888-12,909. doi:10.1002/2014JD022297

Wang, J. and Christopher, S. A., 2003. Intercomparison between satellite-derived aerosol optical thickness and PM2.5 mass: Implications for air quality studies, Geophys. Res. Lett., 30, doi:10.1029/2003GL018174.

Wang, Q., Jacob, D.J., Fisher, J.A., Mao, J., Leibensperger, E.M., Carouge, C.C., Le Sager, P., Kondo, Y., Jimenez, J.L., Cubison, M.J., Doherty, S.J., 2011. Sources of carbonaceous aerosols and deposited black carbon in the Arctic in winter-spring: implications for radiative forcing. Atmos. Chem. Phys. 11, 12453–12473. doi:10.5194/acp-11-12453-2011

Wang, Q., Jacob, D.J., Spackman, J.R., Perring, A.E., Schwarz, J.P., Moteki, N., Marais, E.A., Ge, C., Wang, J., Barrett, S.R.H., 2014. Global budget and radiative forcing of black carbon aerosol: Constraints from pole-to-pole (HIPPO) observations across the Pacific. J. Geophys. Res. Atmos. 119, 195–206. doi:10.1002/2013JD020824

Wang, Y., Jacob, D.J., Logan, J.A., 1998. Global simulation of tropospheric O 3 -NO x - hydrocarbon chemistry: 1. Model formulation. J. Geophys. Res. Atmos. 103, 10713–10725. doi:10.1029/98JD00158

Wang, Y., Logan, J. A., and Jacob D. J., 1998. Global simulation of tropospheric O3‐NO x‐hydrocarbon chemistry: 2. Model evaluation and global ozone budget, J. Geophys. Res. (1984‐2012), 103, 10757-10767.

Wang, Y., McElroy, M. B., Jacob, D. J., and Yantosca, R. M., 2004. A nested grid formulation for chemical transport over Asia: Applications to CO, J. Geophys. Res., 109, 27, DOI: 10.1029/2004JD005237.

Wang, Y., Zhang, Q. Q., He, K., Zhang, Q. and Chai, L., 2013. Sulfate-nitrate-ammonium aerosols over China: response to 2000–2015 emission changes of sulfur dioxide, nitrogen oxides, and ammonia, Atmos. Chem. Phys., 13, 2635.

Wang, Y.X., McElroy, M.B., Jacob, D.J., Yantosca, R.M., 2004. A nested grid formulation for chemical transport over Asia: Applications to CO. J. Geophys. Res. Atmos. 109, n/a-n/a. doi:10.1029/2004JD005237

Warneke, C., Bahreini, R., Brioude, J., Brock, C.A., de Gouw, J.A., Fahey, D.W., Froyd, K.D., Holloway, J.S., Middlebrook, A., Miller, L., Montzka, S., Murphy, D.M., Peischl, J., Ryerson, T.B., Schwarz, J.P., Spackman, J.R., Veres, P., 2009. Biomass burning in Siberia and Kazakhstan as an important source for haze over the Alaskan Arctic in April 2008. Geophys. Res. Lett. 36, n/a-n/a. doi:10.1029/2008GL036194

WHO (World Health Organization, 2005), 2006. Air Quality Guidelines Global Update 2005, WHO/Europe, Copenhagen, Denmark.

William T. Hutzell, D.J.L., 2008. Fate and transport of emissions for several trace metals over the United States. Sci. Total Environ. 396, 164–179. doi:10.1016/J.SCITOTENV.2008.02.020

Williams, J., De Reus, M., Krejci, R., Fischer, H., Ström, J., 2002. Atmospheric Chemistry and Physics Application of the variability-size relationship to atmospheric aerosol studies: estimating aerosol lifetimes and ages, Atmos. Chem. Phys., 2, 133-145. https://doi.org/10.5194/acp-2-133-2002.

Winther, M., Christensen, J.H., Plejdrup, M.S., Ravn, E.S., Eriksson, Ó.F., Kristensen, H.O., 2014. Emission inventories for ships in the arctic based on satellite sampled AIS data. Atmos. Environ. 91, 1–14. doi:10.1016/j.atmosenv.2014.03.006

Wiscombe, W.J., Warren, S.G., 1980. A Model for the Spectral Albedo of Snow. I: Pure Snow. J. Atmos. Sci. 37, 2712–2733. doi:10.1175/1520-0469(1980)037<2712:AMFTSA>2.0.CO;2

Wolf, M.E., Hidy, G.M., 1997. Aerosols and climate: Anthropogenic emissions and trends for 50 years, JOURNAL OF GEOPHYSICAL RESEARCH. doi:10.1029/97JD00199

Yang, F., Tan, J., Zhao, Q., Du, Z., He, K., Ma, Y., Duan, F., Chen, G., and Zhao, Q., 2011. Characteristics of PM2.5 speciation in representative megacities and across China, Atmos. Chem. Phys., 11, 5207.

Yao, L., Garmash, O., Bianchi, F., Zheng, J., Yan, C., Kontkanen, J., Junninen, H., Mazon, S.B., Ehn, M., Paasonen, P., Sipilä, M., Wang, M., Wang, X., Xiao, S., Chen, H., Lu, Y., Zhang, B., Wang, D., Fu, Q., Geng, F., Li, L., Wang, H., Qiao, L., Yang, X., Chen, J., Kerminen, V.-M., Petäjä, T., Worsnop, D.R., Kulmala, M., Wang, L., 2018. Atmospheric new particle formation from sulfuric acid and amines in a Chinese megacity. Science 361, 278–281. doi:10.1126/science.aao4839

Ye, B., Ji, X., Yang, H., Yao, X., Chan, C. K., Cadle, S. H., Chan, T., and Mulawa, P. A. Concentration and chemical composition of PM2.5 in Shanghai for a 1-year period, Atmos. Environ., 37, 499, doi:10.1016/S1352-2310(02)00918-4, 2003.

Yienger, J.J., Levy, H., 1995. Empirical model of global soil-biogenic NO χ emissions. J. Geophys. Res. 100, 11447. doi:10.1029/95JD00370

Yttri, K.E., Lund Myhre, C., Eckhardt, S., Fiebig, M., Dye, C., Hirdman, D., Ström, J., Klimont, Z., Stohl, A., 2014. Quantifying black carbon from biomass burning by means of levoglucosan – a one-year time series at the Arctic observatory Zeppelin. Atmos. Chem. Phys. 14, 6427–6442. doi:10.5194/acp-14-6427-2014

Zarzycki, C.M., Bond, T.C., 2010. How much can the vertical distribution of black carbon affect its global direct radiative forcing? Geophys. Res. Lett. 37, n/a-n/a. doi:10.1029/2010GL044555

Zender, C.S., Bian, H., Newman, D., 2003. Mineral Dust Entrainment and Deposition (DEAD) model: Description and 1990s dust climatology. J. Geophys. Res. 108, 4416. doi:10.1029/2002JD002775

Zhang, L., 2001. A size-segregated particle dry deposition scheme for an atmospheric aerosol module. Atmos. Environ. 35, 549–560. doi:10.1016/S1352-2310(00)00326-5

Zhang, L., Kok, J.F., Henze, D.K., Li, Q., Zhao, C., 2013. Improving simulations of fine dust surface concentrations over the western United States by optimizing the particle size distribution. Geophys. Res. Lett. 40, 3270–3275. doi:10.1002/grl.50591

Zhang, Q., Streets, D. G., Carmichael, G. R., He, K. B., Huo, H., Kannari, A, Klimont, Z., Park, I. S., Reddy, S., Fu, J. S., Chen, D., Duan, L., Lei, Y., Wang, L. T., and Yao, Z. L., 2009. Asian emissions in 2006 for the NASA INTEX-B mission, Atmos. Chem. Phys., 9, 5131.

Zhang, R., Jing, J., Tao, J., Hsu, S.-C., Wang, G., Cao, J, Lee, C. S. L,. Zhu, L., Chen, Z., Zhao, Y., and Shen, Z., 2013. Chemical characterization and source apportionment of PM2.5 in Beijing: seasonal perspective, Atmos. Chem. Phys., 13, 7053, doi:10.5194/acp-13-7053-2013.

Zhang, X. Y., Wang, Y. Q., Zhang, X. C., Guo, W., and Gong, S. L., 2008. Carbonaceous aerosol composition over various regions of China during 2006, J. Geophys. Res., 113, D14111, doi:10.1029/2007JD009525.

Zhao P. S., Dong, F., He, D., Zhao, X. J., Zhang, X. L., Zhang, W. Z., Yao, Q., and Liu, H. Y., 2013. Characteristics of concentrations and chemical compositions for PM2.5 in the region of Beijing, Tianjin, and Hebei, China, Atmos. Chem. Phys., 13, 4631.